

THESIS

LIGHTNING CHANNEL LOCATIONS, LNO<sub>x</sub> PRODUCTION, AND ADVECTION IN  
ANOMALOUS AND NORMAL POLARITY THUNDERSTORMS

Submitted by

Trenton Davis

Department of Atmospheric Science

In partial fulfillment of the requirements

For the Degree of Master of Science

Colorado State University

Fort Collins, Colorado

Spring 2018

Masters Committee:

Advisor: Steven A. Rutledge

Mary Barth (Brock)

Emily Fischer

Steven Reising

Copyright by Trenton Davis 2018

All Rights Reserved

## ABSTRACT

### LIGHTNING CHANNEL LOCATIONS, LNO<sub>x</sub> PRODUCTION, AND ADVECTION IN ANOMALOUS AND NORMAL POLARITY THUNDERSTORMS

Tropospheric ozone is a powerful greenhouse gas and OH precursor, thus understanding its sources is important. Its production is also widely studied in atmospheric science today as global climate modelers attempt to estimate future warming within the troposphere. Nitrogen oxides ( $\text{NO} + \text{NO}_2 = \text{NO}_x$ ), serve as a precursor to ozone production. In areas where higher concentrations of OH are present,  $\text{NO}_x$  will undergo reactions to produce nitric acid, thereby shortening its lifetime and limiting the production of ozone. Due to lower concentrations of OH in the upper troposphere,  $\text{NO}_x$  tends to experience a longer lifetime (on the order of days) and greater ozone production at these heights. Lightning produces an appreciable amount of  $\text{NO}_x$  (a.k.a. LNO<sub>x</sub>) but the final distribution of resulting LNO<sub>x</sub>, and thus its ozone production, remains poorly understood. Therefore, it is important that this source of  $\text{NO}_x$  be further investigated to improve current LNO<sub>x</sub> parameterizations.

Numerical modeling methods attempt to study this issue by parameterizing the nature of lightning within thunderstorms. Often, the vertical distribution of flash channels (and LNO<sub>x</sub>) is produced according to a parameterized flash rate within a defined vertical profile and reflectivity volume threshold. The structure and intensity of thunderstorms are highly variable though, causing the location of lightning within a thunderstorm to differ from one thunderstorm to the next. Furthermore, one remaining goal of the Deep Convective Clouds and Chemistry (DC3)

field campaign (May – June 2012) was to compare the lightning flash locations and contributions to upper tropospheric LNO<sub>x</sub> between storms of normal and anomalous charge polarity.

To address this remaining goal, five cases with over 5600 total flashes are analyzed in detail using data from DC3, three in northern Colorado and two in northern Alabama. Lightning sources are combined into 3-dimensional (3-D) flash channels and flash channel parcels, with each parcel containing the LNO<sub>x</sub> produced by its parent flash channel. Parcels are then advected forward in time during the lifetime of each storm using 3-D wind fields produced from dual-Doppler analyses. Results reveal a greater number of flashes and flash channels within anomalous polarity thunderstorms compared to normal polarity thunderstorms at a mean initiation height around 5 km. Flashes in these storms also appear to transect areas of higher vertical velocities resulting in roughly half of flash channel parcels being advected to the upper troposphere ( $z > 8$  km). Contrary to some assumptions, an appreciable fraction of these parcels and NO<sub>x</sub> contributions remain in the boundary layer of these storms. In the two normal polarity thunderstorm cases, flash channels tend to initiate around 8 km with roughly half of the flash channel parcels remaining near or above 8 km. While both storm types appear to transport roughly 50% of their flash channel parcels to the upper troposphere, significantly larger flash counts and total flash length in the anomalous polarity storms lead to much higher mixing ratios of LNO<sub>x</sub> in the upper troposphere. These results may help chemistry modelers in parameterizing LNO<sub>x</sub> formation in both normal and anomalous thunderstorm polarity structures, which will also improve global climate model parameterizations of tropospheric ozone production.

## ACKNOWLEDGMENTS

The author would like to thank his advisor Dr. Steven Rutledge for his extensive help in both advising, teaching, and mentoring. He would also like to thank to Brett Basarab for providing data for the Colorado cases used from previous work and Dr. Brody Fuchs for data from the Alabama cases. He would also like to specifically thank officemate Dr. Brody Fuchs for extensive consultation of lightning, Python programming, and general graduate school questions. He would like to thank Dr. Brenda Dolan for consultation in radar data processing and graduate school questions. For consultation regarding chemistry-related questions, he thanks Dr. Ilana Pollack and Dr. Emily Fischer. For general programming aid, he thanks Paul Hein. The LMA networks, data, and processing are managed through Paul Krehbiel, William Rison, and Ronald Thomas at New Mexico Tech. Readers are encouraged to visit <https://github.com/deeplycloudy/lmatools> for more information regarding the flash clustering algorithm used to derive flashes for this study. He specifically thanks NSF for providing the funds for this study via the DC3 project (NSF PDM grant number AGS-1429925).

Directly, the author would like to thank his friends, family, Master's graduate committee members, and research group for their continual support that went into his first scientific publication. He would like to thank Zach Finch and Becca Mazur, for directing him to CSU while a NOAA Hollings Scholar at the National Weather Service Cheyenne. He would like to especially thank his parents for pushing him to continue his education in the darkest moments; your support really paid off.

## TABLE OF CONTENTS

ABSTRACT.....	ii
ACKNOWLEDGMENTS .....	iv
TABLE OF CONTENTS.....	v
LIST OF TABLES.....	vii
LIST OF FIGURES .....	viii
CHAPTER 1 INTRODUCTION.....	1
1.1. Study motivation.....	1
1.2. Background.....	4
CHAPTER 2 DATA AND METHODOLOGY .....	9
2.1. Selection of cases.....	9
2.2. Radar attributions.....	10
2.3. Flash clustering algorithm.....	12
2.4. Flash channel parcels .....	14
2.5. Lightning NO <sub>x</sub> calculation .....	16
CHAPTER 3 RESULTS.....	23
3.1. The five cases.....	23
3.2. Storm lifetimes.....	25
3.3. Anomalous polarity cases .....	26
3.4. Normal polarity cases .....	28
3.5. Comparison between all storm cases .....	30

3.6. LNO <sub>x</sub> concentrations.....	35
CHAPTER 4 DISCUSSION.....	71
4.1. DC3 aircraft measurements.....	71
4.2. LNO <sub>x</sub> within the boundary layer.....	72
4.3 Justification discussion .....	74
CHAPTER 5 CONCLUSIONS .....	76
5.1. Summary .....	76
5.2. Normal versus anomalous polarity .....	77
5.3 Flash channel parcel originations.....	79
5.4. Closing statements .....	80
REFERENCES .....	82
APPENDIX A.....	87

## LIST OF TABLES

Table 3.1 .....	69
Table 3.2 .....	70

## LIST OF FIGURES

Figure 1.1 .....	8
Figure 2.1 .....	20
Figure 2.2 .....	21
Figure 2.3 .....	22
Figure 3.1 .....	41
Figure 3.2 .....	42
Figure 3.5 .....	45
Figure 3.6 .....	46
Figure 3.7 .....	47
Figure 3.8 .....	48
Figure 3.9 .....	49
Figure 3.10 .....	50
Figure 3.11 .....	51
Figure 3.13 .....	53
Figure 3.14 .....	54
Figure 3.15 .....	55
Figure 3.16 .....	56
Figure 3.17 .....	57
Figure 3.18 .....	58
Figure 3.19 .....	59
Figure 3.20 .....	60

Figure 3.21 .....	61
Figure 3.22 .....	62
Figure 3.23 .....	63
Figure 3.24 .....	64
Figure 3.25 .....	65
Figure 3.26 .....	66
Figure 3.27 .....	67
Figure 3.28 .....	68
Figure A.1 .....	87
Figure A.2 .....	88
Figure A.3 .....	89
Figure A.4 .....	90
Figure A.5 .....	91

## CHAPTER 1 INTRODUCTION

### 1.1. Study motivation

Resulting from dielectric breakdown of air in the presence of strong electric fields, lightning has been at the center of growing research over the past several decades (Maggio et al. 2005). Due to advances in technology, it is now possible to examine this phenomenon on a flash-scale basis. One such advance, the lightning mapping array (LMA) networks, allows for the detection of the radiative components of all lightning flashes. These components termed sources, can be combined into flashes using a flash clustering algorithm based upon initiation time and location (Fuchs et al. 2016). New developments have enabled lightning flash channels to be mapped from source locations, which can then be analyzed with respect to various radar-derived storm parameters such as reflectivity, wind speed, and hydrometeor species (Fuchs 2017).

Lightning is considered to be the largest natural source of nitrogen oxides ( $\text{NO}_x \equiv \text{NO} + \text{NO}_2$ ) in the upper troposphere, yet the amount of  $\text{NO}_x$  produced by an individual lightning flash is far from certain (Lawrence et al. 1995; Price et al. 1997; Schumann and Huntrieser 2007). Fundamentally, lightning produced  $\text{NO}_x$  ( $\text{LNO}_x$ ) is created as diatomic nitrogen and oxygen dissociate within super-heated air surrounding flash channels, making production proportional to flash channel length (hereafter FCL; Wang et al. 1998). These products then undergo reactions to form NO. After undergoing photolysis, NO is converted to  $\text{NO}_2$ . These two species rapidly interconnect during the daytime, and thus are considered a chemical family ( $\text{NO}_x$ ). The importance of  $\text{NO}_x$  lies in its production of ozone, which in the middle and upper troposphere acts as a greenhouse gas and source of OH. Understanding the vertical transport of  $\text{LNO}_x$  by storm scale updrafts and downdrafts is critical because this transport determines the ozone

production potential of LNO<sub>x</sub>. For example, when NO<sub>x</sub> is transported to the upper troposphere by storm updrafts, its lifetime is on the order of days, allowing for increased production of tropospheric ozone (Ridley et al. 1996). Moreover, Wu et al. (2007) shows that LNO<sub>x</sub> is roughly six times more efficient than anthropogenic NO<sub>x</sub> emissions in producing upper tropospheric ozone due to the extended lifetime at these altitudes. Conversely, NO<sub>x</sub> can be transported to the surface by storm downdrafts, where it can be depleted through the reaction with OH to produce nitric acid, thereby shortening its lifetime to the order of a day or less and preventing substantial net ozone production (DeCaria et al. 2000; Schumann and Huntrieser 2007). Recent research estimates the lifetime of LNO<sub>x</sub> to only be ~3 hours within storm outflow regions (Nault et al. 2017). Until this point, little research has been carried out to quantify the amount of LNO<sub>x</sub> removed to the boundary layer by convective downdrafts as the shortened lifetime at these levels makes in situ measurements by aircraft quite difficult in addition to the difficulty in isolating NO<sub>x</sub> sources from lightning to background NO<sub>x</sub> concentrations (Schumann and Huntrieser 2007). In short, knowing precisely just how much LNO<sub>x</sub> is being input to the upper troposphere by individual thunderstorms is critical to fully closing the global atmospheric NO<sub>x</sub> and ozone budget (Wu et al. 2007).

One aspect in this lack of understanding is knowing where flash channels originate and where LNO<sub>x</sub> generated by those channels is transported, which remain as major gaps in current atmospheric chemistry models. This lack of understanding exists for thunderstorms throughout various atmospheric regions, thereby preventing accurate modeling of ozone in global climate models (Wu et al. 2007). Many studies have investigated this problem using satellite detection of lightning by the Tropical Rainfall Measuring Mission (TRMM) Lightning Imaging Sensor (LIS) and the Optical Transient Detector (OTD), concluding that lightning produces anywhere from 2-

8 Tg of  $\text{NO}_x$  per year, yet still far from the goal of refining this estimate to  $\pm 1 \text{ Tg yr}^{-1}$  (Schumann and Huntrieser 2007). In fact, they note that this estimate has only been improved from 1-8 to 2-8  $\text{Tg yr}^{-1}$  as found by Lawrence et al. (1995).

One method of improving this estimate is to compare  $\text{NO}_x$  production to the number of flashes that occur within individual thunderstorms (e.g. Pollack et al. 2016). Following this, it has since been suggested that both intra-cloud (IC) and cloud-to-ground (CG) flashes produce similar amounts of  $\text{LNO}_x$  (DeCaria et al. 2000, 2005; Schumann and Huntrieser 2007; Ott et al. 2010). While this is an advance in knowledge, not enough improvement appears to have taken place to refine the global  $\text{LNO}_x$  estimate due to the continued lack of understanding in the transport of  $\text{LNO}_x$  to the upper troposphere. Quantifying the impact of storms of various regions on the production of  $\text{NO}_x$  capable of tropospheric ozone production will help to fill gaps in the understanding of global lightning contributions to tropospheric ozone production.

Examining where flash channels originate in individual thunderstorms and where the  $\text{LNO}_x$ -rich air parcels produced from those channels end up is a first step in this process. For example, Pickering et al. (1998) note the critical dependence in upper tropospheric  $\text{NO}_x$  and ozone to the vertical distribution of  $\text{LNO}_x$  in the form of prescribed vertical profiles and the importance of examining  $\text{LNO}_x$  convective redistribution by actual thunderstorms. Barthe and Barth (2008) supports this, noting that the placement of  $\text{NO}$  ( $\text{LNO}_x$ ) within a model domain is of critical importance when calculating the resulting  $\text{NO}$  transport and chemistry. Most research has examined this problem only from a modeling perspective, with little consideration of observational flash channel distribution data. Many current model simulations parameterize  $\text{LNO}_x$  production based on flash rate and distribute the resulting  $\text{NO}_x$  into the troposphere based on methods using vertical profiles from previous studies.

## 1.2. Background

### 1.2.1. Modeling

One such method is that developed by DeCaria et al. (2000, 2005). Initially, flash rates are parameterized as functions of various storm parameters such as reflectivity volume, storm cloud top height and storm ice mass flux (e.g. Basarab et al. 2015). Here IC and CG flashes are modelled by assigning a fixed IC to CG ratio to this flash rate, while confining these flashes to fixed vertical profiles. Regardless of flash type, each flash is set to 18.0 km in total length and distributed according to its prescribed vertical profile. DeCaria et al. (2005) notes that MacGorman and Rust (1998) found most that flash channels occur within reflectivity echoes  $> 20$  dBZ, which they then use to limit the distribution of flash channels uniformly in the horizontal in accordance with the fixed vertical profile.  $LNO_x$  is then parameterized according to the channel length, altitude (pressure), and temperature, while assuming a fixed flash current within these distributions (generally 19 kA; Wang et al. 1998; DeCaria et al. 2000; Barthe and Barth 2008). DeCaria et al. (2000) notes that the vertical distribution of FCL is highly variable, according to MacGorman and Rust (1998), varying from one storm to another and even within a single storm's lifetime. This is troubling because most global atmospheric models use effective vertical emission profiles that could be incorrectly parameterizing the placement of  $LNO_x$  for certain storms at various heights and regions around the globe. Research is needed to investigate the variability in  $LNO_x$  emissions among regions to correctly determine the contribution of lightning to  $NO_x$  and tropospheric ozone production globally. This motivates the examination of the distribution of FCL among storms of different charge structure and how this affects the convective transport efficiency of  $LNO_x$ .

### 1.2.2. Normal and anomalous thunderstorms

While it is unrealistic to study the vertical distribution of lightning channels globally in a single study, this motivates the examination of this distribution between storms of different charge structure in the U.S. where observational analysis is more readily available. As discussed above, the final altitude LNO<sub>x</sub> reaches is critical to determining whether or not it will impact upper tropospheric ozone production efficiency. Fuchs et al. (2015, 2016) and many previous authors describe how thunderstorm charge structures can be reversed from the normal dipole or tripole structure into an anomalous dipole or tripole. Most thunderstorms with this charge structure (hereafter anomalous storms) often exhibit higher reflectivity values, more intense vertical motions, and, sometimes, more intense rainfall and hail all in conjunction with supposedly higher super-cooled liquid water contents (SLWC) in the mixed-phase region. These storms are often associated with environments characterized by high convective available potential energy (CAPE) and shallow warm cloud depths (Williams et al. 2005; Fuchs et al. 2015). The quantitative differences in flash channels and their LNO<sub>x</sub> production between these thunderstorms and those of normal charge polarity both initially and after advection during the storm lifetime have yet to be studied (Barth et al. 2015).

While there are typically two or three charge layers in both thunderstorm types, the difference in the sign of each charge layer ultimately is important in flash channel distribution and LNO<sub>x</sub> production. In normal polarity thunderstorms, flashes tend to initiate between two charge layers, an upper-level region of positive charge and a mid-level region of negative charge. This charge structure is thought to develop when graupel particles collide with smaller ice crystals in the presence of super-cooled liquid water droplets (Takahashi 1978; Saunders et al. 1991; Takahashi 2017). As the graupel descends, it carries this charge, producing a mid-level

negative charge layer while the ascending ice crystals carry a net positive charge to the upper levels of the storm. Most storms possess this charge structure, leading to this “normal” label (Williams 1989). It is important to note here that a greater number of sources of IC flashes is detected within the positive charge region. This will be described in more detail in Section 2.3. On the other hand, enhanced vertical motions within anomalous thunderstorms often lead to higher SLWC. Saunders and Peck (1998) found that the sign of the charge on graupel is correlated to both temperature and SLWC. Hence, in these types of storms opposite charge transfer between graupel and ice crystals can take place (Williams et al. 2005; Bruning et al. 2014). This is thought to cause negative charge to accumulate in the upper levels of these thunderstorms, while positive charge tends to build in the mid-levels (Williams et al. 2005; Fuchs 2017). Flashes still initiate between the charge zones, but greater channel length tends to occur at lower levels in the storm, with breakdown of negative charge occurring in the mid-level positive charge regions. Flash rates also tend to be higher in such cases, which would inherently lead to more initial LNO<sub>x</sub> production, but the impact of these channel lengths at a lower altitude mode to upper tropospheric NO<sub>x</sub> has not been studied. Figure 1.1 provides a simplified depiction of the charge structure of a normal and anomalous polarity thunderstorm for comparison.

Examining the vertical profile of FCL (from observations) and associated LNO<sub>x</sub> production across a variety of storm modes, such as air mass to supercell storms, and storms in moist to dry environments, remains largely unstudied. This study attempts to bridge this gap through examining the organization of flash channels in storms of both normal and anomalous polarity in the U.S. To do this, flash channels are specifically investigated with regard to hydrometeor types, vertical winds (i.e. updrafts and downdrafts), reflectivity, and height to determine initial distributions and associated LNO<sub>x</sub> production. To investigate the LNO<sub>x</sub> transport efficiency of

these different types of storms, a parcel trajectory analysis is also used with the dual-Doppler derived three-dimensional (3-D) winds to advect the produced LNO<sub>x</sub> during the lifetime of each storm. Studying LNO<sub>x</sub> production in this manner separates this study from previous modeling studies such as DeCaria et al. (2000, 2005) who parameterize flash channel and LNO<sub>x</sub> production rather than examining it from LMA observations. This study also differs from observational studies that do not consider actual flash channel variation but instead average in situ NO<sub>x</sub> measurements among all flashes (either IC, CG, or both), inherently assuming production is the same for all flashes.

Collectively, the goal of this study is to investigate the production and transport of LNO<sub>x</sub> in normal and anomalous thunderstorms using observational radar and LMA data to recreate lightning flash channels. This will improve our understanding of how LNO<sub>x</sub> production changes as a result of the dynamics and charge structure differences for storms of each polarity structure. These results provide chemical transport modelers with possible avenues to improve LNO<sub>x</sub> parameterizations (at least for storms of similar charge structure in these two regions). This collective goal can be refined into three questions that this study will attempt to address:

1. Where do flash channels occur and where is LNO<sub>x</sub> specifically created in storms of normal and anomalous polarity?
2. To where is the LNO<sub>x</sub> being advected in storms of each polarity structure?
3. What is the mean LNO<sub>x</sub> production per flash for each polarity structure?

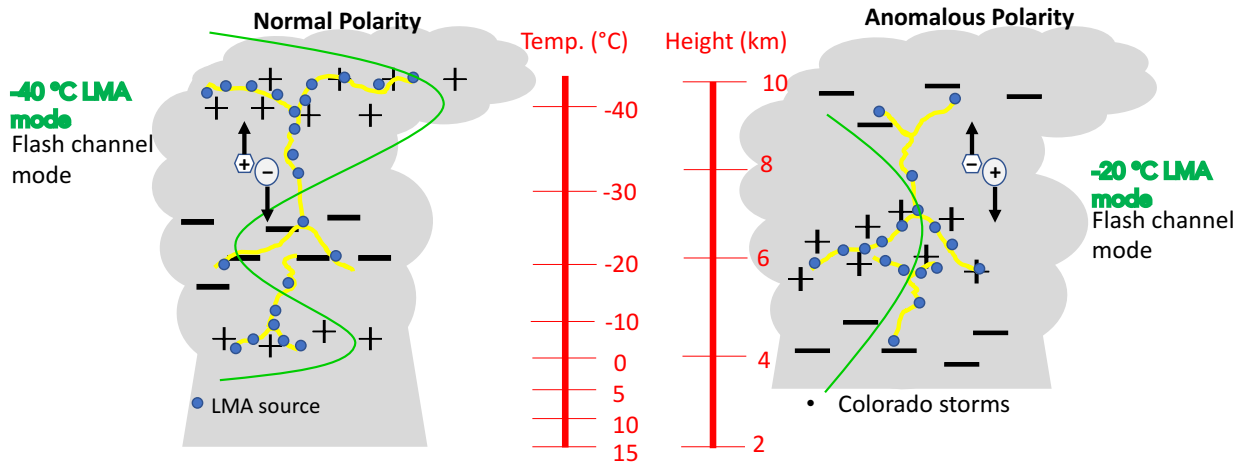


Figure 1.1: Cartoon depiction of the charge structure of a normal (left) versus anomalous polarity (right) thunderstorm tripole adapted from Fuchs (2017). Representative flashes (yellow) with associated sources (blue dots) show flash channel tendency with a flash channel mode near 9 km in normal polarity storms and near 6 km in anomalous polarity storms. Representative positive (+) and negative (-) charge layers also shown. Vertical profile of summed sources characteristic of each polarity type shown in green. Charge transfer tendency between graupel (light blue circle) and ice crystal (light blue hexagon) theorized to lead to these charge structure shown with hydrometeor direction of motion depicted by arrow attached arrows.

## CHAPTER 2 DATA AND METHODOLOGY

### 2.1. Selection of cases

To accomplish these goals, five case-study storms are selected from the data-rich observations of the Deep Convective Clouds and Chemistry (DC3) field campaign conducted in May - June 2012 (Barth et al. 2015). Isolated storms are selected for this study so that lightning flash channels and their LNO<sub>x</sub> production can be properly attributed to each storm with no overlap between separate convective cells. Furthermore, isolated storms tend to have better distinguished updrafts and downdrafts compared to linear storm complexes. The latter can be hard to define in multi-cell thunderstorms that are usually composed of developing and decaying cells. Flashes are attributed to storms using very high frequency (VHF) Lightning Mapping Arrays (LMAs) in northeast Colorado (COLMA) and Northern Alabama (NALMA). Radar observations were measured by the Colorado State University (CSU) (S-band) and CSU Pawnee (S-band) radars in the northern Colorado region and the National Weather Service (NWS) WSR-88D KHTX (S-band) and University of Alabama in Huntsville (UAH) ARMOR (C-band) radars in the northern Alabama region. Due to the intricate nature and randomness of storm path trajectories, only selected storms fit the criteria for this study. To be selected, storms needed to (1) remain isolated in nature, (2) move nearly perpendicular to the baseline between radars used for dual-Doppler analysis so that 3-D winds could be properly estimated, (3) occur within the detection range of the LMA networks and radars throughout the entire lifetime of the storm, and (4) produce enough flashes to analyze ( $n_{fl} \geq 100$ ). Based on these criteria, 5645 lightning flashes from five thunderstorm cases are gridded, totaling 206,565 km of FCL segments. The three selected anomalous polarity storms occurred on 6 June, 27 June, and 28 June 2012 in Colorado

while the two normal polarity storms occurred on May 18 and June 11, 2012 in Alabama. Further descriptions of each storm are provided in Section 3.1. The total channel length of each flash is then divided into 1 km flash channel parcels and advected forward throughout each respective storm lifetime. This is described further in Section 2.4.

## 2.2. Radar attributions

Dominant hydrometeor fields are created for each 3-D radar domain using a combination of dual-polarization variables. A fuzzy logic framework is used with CSU RadarTools for this calculation (Dolan et al. 2013). This method uses radar variables such as reflectivity, differential reflectivity, correlation coefficient, and specific differential phase along with the temperature (interpolated from corresponding soundings in shown in Appendix A) to determine a hydrometeor identification (HID) that best matches the corresponding variables attributed to each grid cell. Once HID has been estimated, vertical fall speeds can be calculated for the hydrometeors, and the 3-D wind fields can be created. Fall speeds are estimated for the identified hydrometeors in each grid cell based on observed fall speeds for similar hydrometeor species. Temperature soundings are also used to determine whether hydrometeors in grid cells are frozen or melted.

Dual-Doppler syntheses were performed using consecutive scans of the two radars in each region (CSU CHILL and CSU Pawnee, KHTX and UAH ARMOR; see Fig. 2.1). First, the radar fields are gridded to 1 km in resolution for the UAH radars and 0.5 km for the CSU radars. Radial winds are also converted to the U and V wind components using Radx2Grid. Note that the U-wind component corresponds to the north-south direction, and the V-wind component corresponds to the east-west direction. NCAR Custom Editing and Display of Reduced

Information in Cartesian space (CEDRIC) software is then used to retrieve the vertical wind component throughout the storm volumes. This is done by using the known horizontal wind components for each grid cell in conjunction with the mass continuity equation to solve for the vertical wind component. Dominant hydrometeor fall speed is then subtracted from each grid cell to consider the contribution from hydrometeors. This calculation is repeated and vertically integrated for all grid cells until the vertical wind profile is left with no motion immediately at the surface and the tropopause, as would theoretically occur (only convergence and divergence can exist at these levels as air is not allowed to penetrate the ground or stratosphere). While not a perfect retrieval, this method typically resolves vertical winds inside convection to within  $\pm 1 \text{ ms}^{-1}$  (Nelson and Brown 1987). One inherent shortfall of using multi-Doppler syntheses to calculate 3-D wind fields is that radial winds cannot be computed in areas without precipitation-sized hydrometeors to backscatter emitted radiation to the radar, and therefore vertical wind speeds also cannot be computed for these regions. This usually is true only for volumes outside the identified storm cells, but it is still important that winds exist in these regions so that flash channel parcels that may advect outside the main storm cells can continue to freely travel. To overcome this, storm soundings are interpolated to the vertical grid, and horizontal wind components are set for each level. The storm motion is subtracted from these winds so that only storm-relative winds are being used for parcels along their entire trajectories. Horizontal winds are then set for each vertical grid level for areas outside the storm cell. The vertical wind component was set to  $0 \text{ ms}^{-1}$  for grid cells at all levels where winds could not be determined. This likely introduces some error, but little vertical motion should occur outside thunderstorms, otherwise hydrometeor scatterers would more than likely be present with air parcels reaching their lifting condensation levels. Gravity waves likely exist near the tropopause within the storm

anvils but are likely to not exceed the error bounds of  $1 \text{ ms}^{-1}$  and are therefore ignored.

Soundings used for interpolating these winds are listed in Appendix A.

Each of the storm cells is identified and tracked using an automated case study framework so that characteristics of the radar and lightning data for each storm can be properly studied. The CSU Lightning, Environmental, Aerosol and Radar (CLEAR) framework contours the 35 dBZ composite reflectivity areas over consecutive radar scans (Lang and Rutledge 2011). New areas are identified as new cells and tracked until they merge with a larger cell or dissipate. A benefit to this method is that reflectivity echo and other radar variables for each scan time are calculated and stored for each cell. Once cells are tracked, sources and flashes can be attributed to each cell over their respective lifetimes.

### 2.3. Flash clustering algorithm

After the cells have been tracked, flash processing using data measured by LMAs can take place. LMA networks are constructed as a set of about ten stations designed to detect very high frequency (VHF  $\approx 60\text{-}66 \text{ MHz}$ ) radiation emissions produced from the discontinuous breakdown of lightning channel leader propagation (Rison et al. 1999). This is seen in the form of a series of numerous emission sources for each flash. The number of sources per flash can vary from tens to thousands depending on the spatial extent and detection efficiency of the flash, which depends upon the efficiency of the network and distance of the flash from the LMA center (Fuchs et al. 2016; Fuchs 2017).

Processing starts with combining sources into flashes based on a flash clustering algorithm described by Bruning (2013) and Fuchs et al. (2015, 2016). For this study, flashes require ten or more sources in Colorado and two or more in Alabama to prevent spurious flashes from being

created. Also, flashes are attributed to cells if they occur within or up to 10 km outside of a cell contour; all other flashes that occurred outside this range for each case are considered to be associated with other cells and ignored. Flashes that occur within 10 km of multiple cell contours are attributed to the nearest cell. One natural artifact of LMA detection is that more sources often appear within the positive charge region since the breakdown of negative charge within positive charge is a physically more noisy process, and more radiation is produced (Rison et al. 1999; Williams 2006). For an LMA network, this is reflected in the form of a greater number of sources appearing in sections of flashes transferring negative charge into regions of positive charge. This measurement characteristic allows for the polarity charge structure to be determined. The process of constructing flashes from sources is by no means perfect, but it has been refined overtime and is considered accurate. In fact, Krehbiel et al. (2000) showed that LMAs can detect the in-cloud portion of flash channels quite well.

FCL segments are created in a 3-D field at 1 km resolution to match the radar and 3-D wind fields. Fuchs (2017) shows through sensitivity tests that lightning channel vertical distribution best matches the vertical distribution of sources most often at 1 km resolution, so this resolution was chosen for this study. Since the radar data was previously gridded at 0.5 km resolution for initial analysis in the Colorado cases, a nearest-neighbor method is used to produce a 1 km resolution parameter field for all dual-Doppler radar variables. In a sense, only data at integral Cartesian grid locations in each dimension is used, yielding radar parameter fields at 1 km resolution for the Colorado storms to match that of the Alabama storms. Since flash channels produce the radiation detected as sources through their discontinuous breakdown of air, flash channels are essentially created for each flash using grid cells containing at least one source. The final distribution of these tallied grid cells makes up a gridded representation of each flash. FCL

fields can be created at various resolutions, but it has been determined that at 1 km, the vertical profile of FCL best matches the vertical profile of sources (Fuchs 2017). Cases were selected well within optimal detection range (~100 km) of each LMA center, so source detection should be quite efficient for all five storm cases.

As previously discussed, the additional concentration of sources within areas of positive charge would appear to bias flash channel construction in these areas. On the other hand, fewer sources in areas of negative charge representing the breakdown of positive charge would appear to lead to suboptimal flash channel construction in these charge regions. Sensitivity tests show that accurate flash channel representation can still be constructed for flashes even when the weak power sources are removed (Fuchs 2017). Therefore, we determine that the bias of flash channels to positive charge regions is of minimal impact.

#### 2.4. Flash channel parcels

Storm wind fields produced from the dual-Doppler analyses provide a convenient framework for investigating the LNO<sub>x</sub> convective transport efficiency. To do this, theoretical flash channel parcels are created at all grid cells transected by lightning flash channels for each storm as a function of time. The parcels are then advected forward in a Lagrangian framework according to the 3-D wind fields in a pseudo-model method. To start each case, parcels are created when and where LMA observed sources occur within grid cells (see Fig. 2.2). Time steps between the advection of each parcel are set to 50 seconds, less if the wind component speeds are updated with a following radar scan within 50 consecutive seconds of the parcel's current time step. For example, assuming radar scan intervals are 5 minutes each (as is the case for CSU CHILL) and a flash occurs 20 seconds after the start of a radar scan, all flash channel parcels making up that

flash would advect five times, at 50 seconds in duration each for a total change in time of 250 seconds, and then 30 seconds for the sixth time step to allow the parcel to begin advection for the seventh time step with a fresh radar scan. After that, each wind component would be updated and the process would continue with six time step advections at 50 seconds each. 50 second time step intervals are chosen so that space-time congruency can be maintained. In the case that flash channel parcels ran out of the pseudo model domain, they were kept at the boundary edge.

Many benefits result from analyzing flash channel parcel trajectories in a Lagrangian framework. One being that all storm parameters such as reflectivity, wind speeds, dominant hydrometeor identification (HID), Cartesian coordinate locations, and distance traveled can be recorded after each time step creating a spatial location history for each parcel and flash parcel group. With this, flash channel parcels can be analyzed individually or as a sum at any point during each storm's lifetime. Parcels can be analyzed for each flash to record where they travel throughout the storm's lifetime without worrying about their influences upon one another. Figure 2.3 provides an example of a single flash comprised of 33 flash channel parcels and their trajectories throughout the lifetime of the June 6, 2012 Colorado storm. The flash-produced parcels were then analyzed according to various storm parameters from their initial to final locations to determine when and where flash channels were originating and where the produced  $\text{LNO}_x$  within each parcel advects. Note that parcels are advected independently of one another, so the  $\text{LNO}_x$  contained within each parcel is retained and final profile analysis is done at the end of each storm's lifetime. Initial and final profiles of FCL are formed by summing the parcels along the z-axis. This analysis method will be discussed in more detail in Section 3.6.

## 2.5. Lightning NO<sub>x</sub> calculation

Since flash channel parcels are created for each flash as a construct from the grid resolution, assumptions regarding the channel length within each grid needs to be made. It is assumed that a flash travels perpendicular to the edges of each cell, whether horizontal or vertical, traveling the exact length of the average of each of the three dimensions. Since each grid cell is one cubic kilometer, we assume the FCL of each parcel is the average of each dimension, i.e. 1 km. This likely introduces some error as the tortuosity of each channel is ignored but it is assumed that this averages among all parcels to minimal impact.

With FCL being attributed to each parcel, LNO<sub>x</sub> can be parameterized based upon the initial environmental conditions of each parcel. DeCaria et al. (2000) describes one such method based upon the lab findings of Wang et al. (1998) who found NO<sub>x</sub> production to be nearly linearly proportional to channel length ( $r^2 = 0.67$ ) at a given flash current. The resulting equation of best fit for the study giving the NO production (in molecules m<sup>-1</sup>) as a function of pressure  $p$  (in Pa) is

$$n_{no}(p) = a + bp,$$

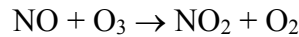
where  $a$  and  $b$  are constants (described below). DeCaria et al. (2000) note the mean flash channel current based on data from the National Lightning Detection Network (NLDN) for the simulated storm in their study was 15 kA, whereas the U.S. mean current estimate from NLDN is ~30 kA (Wacker and Orville 1999). Channel current can vary widely, and it is usually highest for large positive CG flashes common to the stratiform regions of mesoscale convective systems (MCSs), which were not considered in this study. We assume all flashes occur within this range and define a set value of 19 kA for each channel based upon the original NO<sub>x</sub> equation from Wang et al. (1998). Changes in the current would affect the linear fit of NO<sub>x</sub> production versus pressure and thus constant  $a$  and coefficient  $b$  would change. Future work could test LNO<sub>x</sub>

production and redistribution for varying current estimates, but this is outside the scope of this study.

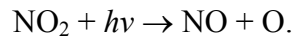
DeCaria et al. (2000) start their derivation of NO production per cloud to ground (CG) flash using this equation, which can be applied to each flash channel parcel in our analysis. Since the focus of this study is on flashes in terms of channel length, this equation is utilized to produce NO per meter of FCL and can be multiplied by the average length for each grid cell to get an equation for the total NO production per grid cell based on the cell's initial pressure. The resulting equation gives the total number of molecules of NO produced for each grid cell of FCL

$$n_{NO}(p) = (a + bp)\bar{l},$$

where  $a = 0.34 \times 10^{21}$  molecules  $m^{-1}$ ,  $b = 1.30 \times 10^{16}$  molecules  $m^{-1} Pa^{-1}$ , and  $\bar{l}$  is the average length of each grid cell traversed by each FCL (i.e. 1000 m). The photostationary state assumption assumes that the production of  $NO_2$  from NO,



is nearly instantaneously balanced with its destruction through photolysis,



In other words, the sum of NO and  $NO_2$  remains approximately unchanged as  $NO_x$  molecules transition from one form to another (Leighton 1961; DeCaria et al. 2005; Schumann and Huntrieser 2007). This is a reasonable assumption for areas away from large sources of organic radicals in the boundary layer, as are most of the flash channel parcels in this study (DeCaria et al. 2005). As photolysis ceases during the night, more  $NO_x$  is stored as  $NO_2$ , but can photolyze back to NO after sunrise. With this, we can treat NO as being the primary component in the contribution of  $LNO_x$  to total  $NO_x$  (DeCaria et al. 2000). Therefore, each parcel carries the  $LNO_x$  produced from a 1 km, 19 kA flash channel at an initial pressure. This concentration can be

tracked anywhere during its parent storm's lifetime after the initial flash has occurred. The  $\text{LNO}_x$  production within the parcel is also converted from molecules to moles by simply dividing by Avogadro's number. To get the mixing ratio of  $\text{LNO}_x$  at each level, the moles of  $\text{LNO}_x$  in all parcels are summed up for each vertical 1 km level in the identified cell and then divided by the total number of moles of air that the flash channel parcels reside within at that specific level (see Section 3.6.1).

Note that vertical mixing within and above the boundary layer can often be higher over the High Plains causing an increase in boundary layer depth than in the U.S. Southeast. The deepest boundary layers among these cases occurred on June 27 and 28, 2012 in the Colorado anomalous thunderstorm cases ( $\sim 4.8$  km above MSL), calculated as height of lowest inversion level in soundings (see Appendix A for soundings). Deep boundary layers are not uncommon for the High Plains, as previous field projects such as the DISCOVER-AQ/FRAPPÉ (Deriving Information on Surface conditions from Column and Vertically Resolved Observations Relevant to Air Quality/Front Range Air Pollution and Photochemistry Experiment) (July - August 2014) field campaign found. In this study, a maximum boundary layer height of 4.2 km above MSL (2.5 km above ground level at  $\sim 1.7$  km for the Denver Metro area) along with some mixing of free tropospheric air into and out of the boundary layer was found to occur over the two-month study (Kaser et al. 2017).

To ensure  $\text{LNO}_x$  is well removed from the boundary layer of our storms and to heights where the lifetime of  $\text{NO}_x$  is sufficient to produce ozone a boundary we define a boundary separating the upper and lower troposphere. Various studies have defined a boundary between the upper and lower troposphere as being roughly 8 km above mean sea level (MSL) (e.g. Ridley et al. 1996). Therefore, this study uses 8 km as an arbitrary boundary between the upper-lower

troposphere to consistently compare transport between the various cases for this study. This is simply a boundary to compare flash channel parcels in terms of whether they reach the upper troposphere or not. With this boundary, LNO<sub>x</sub> concentrations can be equally compared between all five cases. We can have higher confidence that parcels above 8 km will remain there after their parent storm dissipates and that clear sky conditions will allow for photolysis and ozone production in the following days.

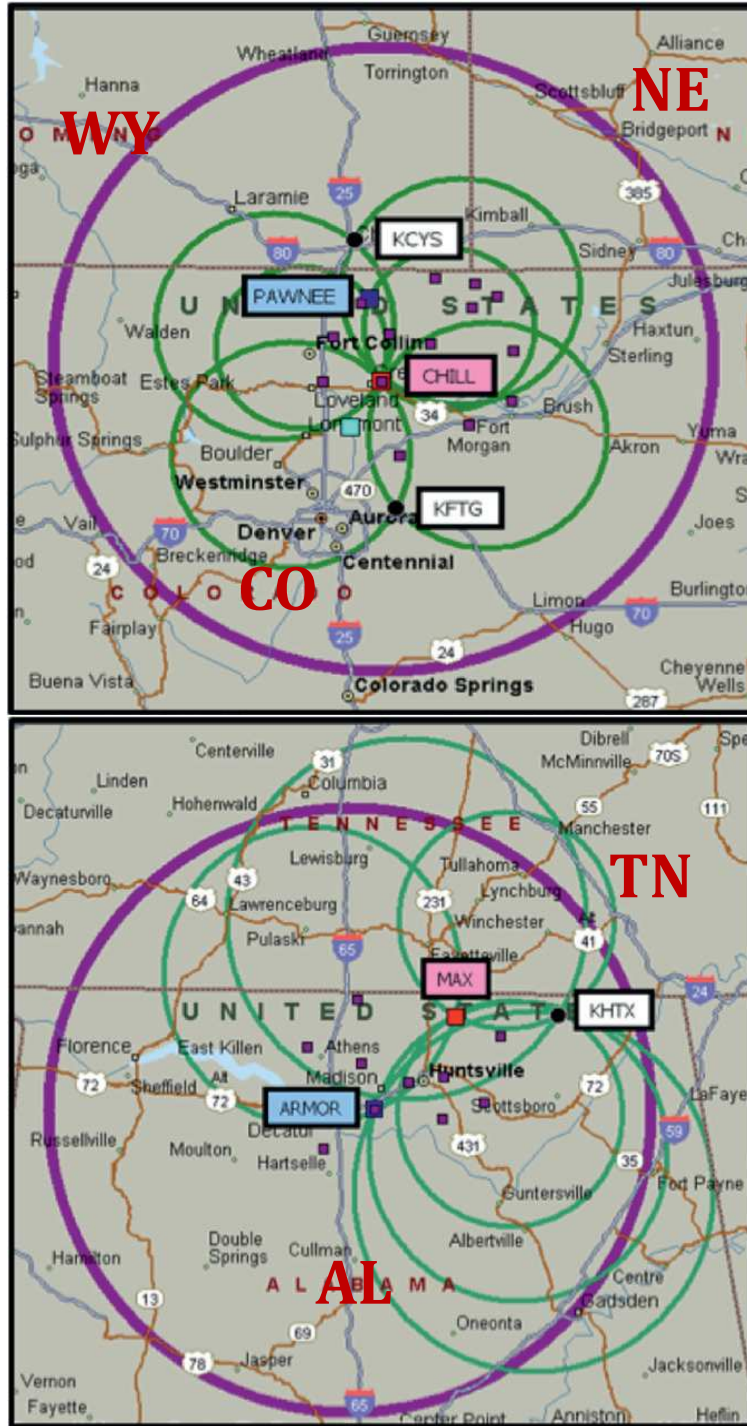


Figure 2.1: Doppler radar and LMA station set-up for both Colorado (top) and Alabama (bottom) DC3 regions from Barth et al. (2015). Radars used in this study are top: CSU CHILL (red square) and Pawnee (dark blue square) and bottom: KHTX (white square) and ARMOR (dark blue square). Dual-Doppler and polarimetric radar coverage depicted by green circles. LMA stations depicted by purple squares with 300 m detection range depicted by purple circle.

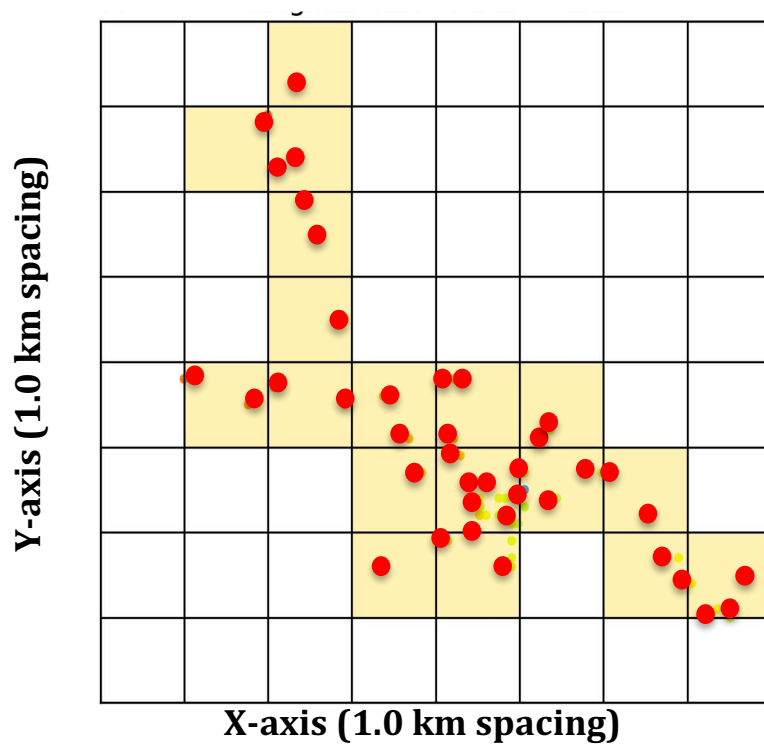


Figure 2.2: Example of a gridded lightning flash in X-Y dimensions at 1.0 km resolution. Individual sources within flash depicted by red circles. Sources are laid upon grid. Grid cells containing at least one source are highlighted in yellow, signifying the flash transected the cell. Highlighted grid cells each represent 1 km of flash channel length and become flash channel parcels to be advected forward in storm winds throughout the lifetime of parent storm.

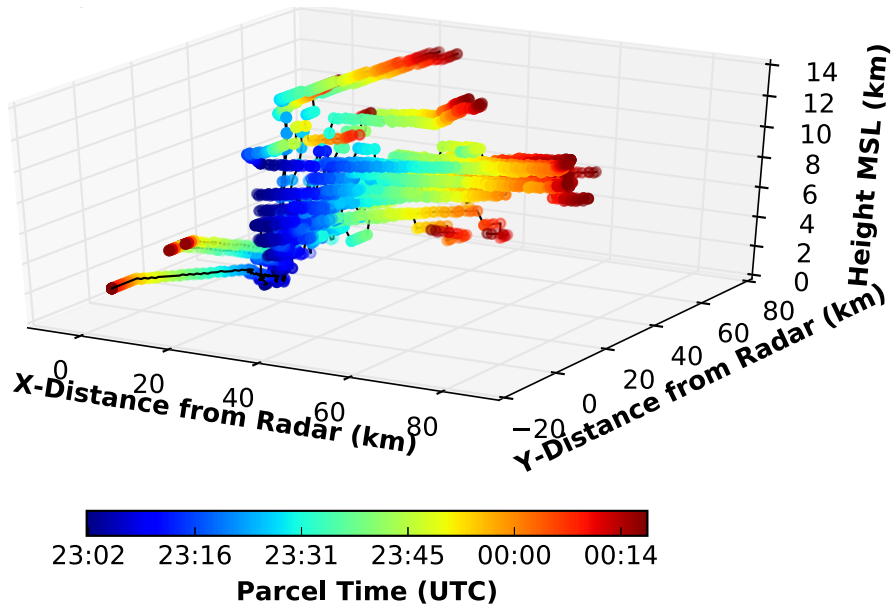


Figure 2.3: Example trajectories of individual flash parcels initialized for a single flash in the June 6, 2012 Colorado storm. Parcels are colored by time from the initial flash time (blue) to the end of the storm lifetime (red). Note the flash displayed is comprised of 33 flash parcels with 101 time steps. Notice the varying directions in which parcels advect due to changes in wind with height.

## CHAPTER 3 RESULTS

### 3.1. The five cases

The strongest of the five storm cases occurred in Weld County, Colorado from 2259-0017 UTC June 6-7, 2012. This storm was super-cellular in nature, prompting a severe thunderstorm warning from 2334-0015 UTC as it moved north-northeast from just north of the Denver metro area to the Wyoming border. This storm was one of several super-cellular storms that later converged into a larger complex after this individual storm dissipated. Significant hail and rainfall accompanied this storm, which is consistent with maximum updraft speeds nearing  $40 \text{ ms}^{-1}$  at times. The polarity of this storm was anomalous with a larger number of sources in the mid-levels of the storm centered around 6.0 km, indicative of predominant midlevel positive charge. Sources created a bimodal vertical distribution with a primary mode at 6 km and a secondary peak at 10 km. Lightning activity was quite intense in this case, with flash rates peaking at  $111 \text{ fl. min}^{-1}$  and a total of 3737 flashes occurring during its lifetime. This storm has been studied extensively due to its near ideal motion and lifetime all within the dual-Doppler network of the CSU CHILL and Pawnee radars and well within a 100 km radius of COLMA (e.g. Basarab et al. 2015; Fuchs et al. 2016).

The second case occurred along the Front Range in Colorado from 2154-2254 UTC on June 27, 2012. This storm was weaker than the previously described storm but also remained anomalous in polarity with a peak in sources centered around a single mode at 6 km. Flash rates were also lower, peaking at  $65 \text{ fl. min}^{-1}$  and producing 723 total flashes. The motion of the storm was also different as it moved eastward from the foothills of the Rocky Mountains onto the plains from Larimer to Weld County, Colorado. Storm structure was more elongated with a

much larger region of reflectivity echo values below 40 dBZ. The storm was also not as super-cellular in nature with larger areas of weaker reflectivity surrounding the main cell downwind of the main updraft. Updraft speeds were also lower with a maximum reaching  $\sim 17 \text{ ms}^{-1}$ .

The third and final case in Colorado occurred from 2039-2159 UTC June 28, 2012. Storm motion and structure closely resembled the previous case with polarity also remaining anomalous. On the other hand, the vertical distribution of sources more resembled the June 6 Colorado storm with main peak at 6 km and a slight secondary maximum near 9 km. Vertical motions were slightly weaker in this storm with maximum updraft speeds reaching  $\sim 15 \text{ ms}^{-1}$ , though downdrafts surpassed  $11 \text{ ms}^{-1}$  at times. Flash rates only peaked at  $28 \text{ fl. min}^{-1}$  in this storm, with a total of 687 flashes.

In northern Alabama, the fourth and fifth storm cases occurred from 2223-2256 UTC May 18, 2012 and 2018-2122 UTC June 11, 2012. Both cases were more discrete cells, common to the U.S. Southeast in summer. Steering flow (e.g. 500 mb winds) and 0-6 km effective bulk shear were weak, especially for the May 18 case, causing both storms to remain nearly stationary with a slight drift towards the southeast. Both storms were of normal polarity with a source mode height of 7 km (May 18 storm) and 9 km (June 11 storm). The overall depth of sources was deeper than that in the Colorado cases though. Both storms were similar in overall strength with a reduced reflectivity echo volume exceeding 20 dBZ (hereafter 20 dBZ volume). Maximum updraft speeds approached  $10 \text{ ms}^{-1}$  in each case with 238 total flashes for the May 18 storm and 267 flashes for the June 11 storm. For a list of storm intensity parameters along with flash information for each storm event, refer to Table 3.1.

### 3.2. Storm lifetimes

Lightning activity is well correlated with many intensity indices for these five storm cases. For example, Fig. 3.1 shows that various storm volumes (20 dBZ reflectivity echo, updraft volume  $\geq 5 \text{ ms}^{-1}$ ) along with the total FCL and flash rate for each storm over its respective lifetime follow similar trends of increase and decrease in accordance to flash rate and total FCL. It appears that the 20 dBZ volume, updraft volume, flash rate, and total FCL all increase and decrease in unison to a large extent, and the total FCL and flash rate appear to correlate between all cases (mean  $r^2 \cong 0.7$  for all cases). The downdraft volume does not appear to change as often as the updraft volume for each case, indicating the overwhelming strength and expanse of updrafts compared to downdrafts. This makes sense as maximum downdraft velocities did not peak nearly as high as updraft velocities. Though the total FCL and flash are somewhat correlated, total FCL does not appear to linearly correlate with flash rate most often during peaks in the flash rates.

Previous studies have suggested that stronger electric fields build during peaks in storm intensity, causing stronger reservoirs of charge to build and therefore shorter flashes are needed to equilibrate these charge differences (e.g. Carey et al. 2005; Kuhlman et al. 2009; Weiss et al. 2012; Bruning and MacGorman 2013). Accordingly, such shorter flashes also tend to occur near deep convective updrafts. Figure 3.2 shows a scatterplot of flash rate versus FCL for all flashes in all five storm cases in this study. A clear decrease in FCL for flashes that occur during higher flash rate periods appears, though there are a few outlier flashes in the June 28 case. This suggests that smaller flashes, likely surrounding the updraft cores, likely occur during peak storm intensity. With these shorter flashes, less  $\text{LNO}_x$  is produced per flash during this time – this topic

will be discussed further in Section 4.3. Also note that significantly higher flash rate peaks occur in the anomalous storms in Colorado compared to the normal polarity storms in Alabama.

### 3.3. Anomalous polarity cases

As previously discussed, the three anomalous thunderstorm cases in Colorado were more intense compared to the normal polarity cases in Alabama. The flash rates were also much higher throughout the lifetimes of these storms, along with significantly higher total flash counts. In addition to the lower mode in source initiation, another key distinction in these storms is the lower mode in flash channel initiation. In fact, mean flash channel initiation heights were around 5 km for these three cases versus 8 km for the normal polarity cases. Figures 3.3 and 3.4 show cross sections taken through the three anomalous storms with FCL contours overlaid. Flash channels clearly appear to congregate around 5-6 km for these storms. This artifact resembles findings by Fuchs (2017) who found the mode in flash channel height to be  $\sim 7$  km for Colorado and  $\sim 9$  km for Alabama. This tendency is also seen in the vertical distribution of flash sources initiating around 6 km. Most flash channels appear to occur during the peak in the flash rate from 23:16-23:32 UTC for the June 6 case (Fig. 3.5), from 21:57-22:06 UTC for the June 27 case (Fig. 3.6), and from 20:47-21:07 for the June 28 case (Fig. 3.7).

Few flash channel parcels appear to remain within mid-level regions of these storms. For example, Fig. 3.5 (a, b, c) shows that flash channels initiating from 8-12 km appear to advect upward while those below this (mainly  $< 6$  km) seem to advect downward or remain near their level of initiation, especially during peaks in flash rates. To little surprise, spikes in maximum updraft and downdraft speeds also occur during these periods. This appears to allow for the transport of flash channel parcels, leading to the distinctive gap of flash channel parcel fractions

in the mid-levels (6-12 km) throughout the storm lifetime as seen for the June 6 storm. Similar results occur for the June 27 and 28 cases with almost identical plots occurring (Figs. 3.6 and 3.7). Most flash channel parcels near the bottom and tops of each storm case seem to have initiated within 2 km of these heights, though this is likely due to the fewer parcels that occur at these extremes too. Towards the end of the lifetime of these storms, a greater fraction of parcels appears to remain within 2 km in the mid-levels as vertical motions begin to subside however.

Examining the advection of flash channel parcels at each of the various levels throughout these storms and over their respective lifetimes reveals deep upward advection. Figure 3.8 shows the number of flash channel parcels, each representing 1 km of FCL, initiating at all 1 km height intervals for the three anomalous Colorado storm cases. Parcels at each level are divided into their final vertical levels and further broken up into the number of parcels that advect upward more than 2 km (hatched areas) or downward more than 2 km (dotted areas). Figure 3.9 shows the same plots but for the two normal polarity Alabama cases. Notice the larger number of parcels that advect upward by 2 or more kilometers in the Colorado versus Alabama cases. Strong downward advection of parcels does not seem to occur in any of the five cases, which agrees with findings for a Colorado storm during the Stratospheric-Tropospheric Experiment: Radiation, Aerosols, and Ozone (STERA0)-Deep Convection field campaign (Dye et al. 2000). Figure 3.10 shows a similar view of the first plot in Fig. 3.8 for the June 6 storm but with each vertical bar normalized by the number of parcels initiating at that level. Upward advection is strongest in this case, with more than 78% of all parcels advecting upward more than 2 km for all initial levels between 4 and 9 km as shown by the hatched bar sectors. This suggests that though flash channels tend to originate at lower levels in anomalous thunderstorms, the enhanced vertical motions transport a significant portion, even a majority at some levels, of the induced

parcels higher into the thunderstorms. Figure 3.11 also shows a similar representation of the upward advection of parcels for the June 6 storm. Here, a two-dimensional histogram of parcels categorized by initial vertical wind speed and initial height (left) is compared to the initial vertical wind speed and final height (right). It is clear that a large fraction of the parcels is advected upward to heights above 8 km with most parcels at these heights initiating in positive vertical winds. Parcels ending at the greatest heights also appear to have initiated in the strongest vertical winds. As will be discussed in Section 3.6, this has substantial impacts on LNO<sub>x</sub> transport with larger amounts making it into the upper troposphere in these thunderstorms. At these levels, LNO<sub>x</sub> is well removed from the boundary layer and is likely to survive longer with ample time to produce ozone. Even though flashes (and channels) occur lower in these thunderstorms, they have a larger impact on the tropospheric NO<sub>x</sub> and ozone budget in the upper troposphere.

### 3.4. Normal polarity cases

The two normal polarity thunderstorm cases that occurred on May 18 and June 11, 2012 in northern Alabama were significantly less intense, and this is observed in both flash rates and vertical motions for each storm. For both cases, flash rates never exceeded 10 fl. min<sup>-1</sup> (computed at 1 minute time increments) and total flash counts were only 238 (May 18) and 267 (June 11) as identified through LMA data. These are only nearly one third of the totals for each of the two weaker anomalous cases in Colorado. Figure 3.12 provides an example cross sectional view with total FCL contoured in black for channels lying within 1 km on either side of the cross section for both storms at times near their peak intensities. Therefore, it is no surprise that parcel

counts were less than half that of the 2 weaker anomalous cases, totaling only 8881 (May 18) and 6737 (June 11).

As previously discussed, flashes tended to initiate at higher altitudes in these cases, with a flash channel mode lying at 8 km (see Fig. 3.9) Also note that the x-axes for these cases extends to only 2500 parcels in the plots of this figure, one tenth that of the June 6 Colorado case and one fourth of the other two Colorado cases. These results fall in line with those of Fuchs et al. (2016) and Fuchs (2017) who found a flash channel mode  $\sim 7$  km for Colorado storms and  $\sim 8$  km for Alabama storms through an analysis of flashes in nearly 4000 thunderstorms. Therefore, these cases likely represent common storm structure in each region.

Vertical wind speeds were less intense for these normal polarity storms, as Fig. 3.13d,e and Fig. 3.14d,e show in the vertical profile time series of maximum updraft and downdraft speeds for these storms. Updraft volumes tended to stay below  $100 \text{ km}^3$  throughout most of the lifetimes of these storms too, indicating less volume of the storm was available for deep vertical transport of flash channel parcels after initiation. A smaller number of parcels appear to initiate in updrafts over  $5 \text{ ms}^{-1}$  in these cases, even though the fraction of parcels in the May 18 case is more comparable to the June 27 and 28 Colorado cases. Figure 3.9 shows that relatively few parcels initiating below 12 km could make it above this level, unlike what is seen for the anomalous Colorado cases.

A key difference in advection between the normal polarity and anomalous polarity cases is that the flash channel parcels initiate at greater heights in the normal polarity cases, but they tend to remain closer to their initiation heights. Figures 3.13b and 3.14b show the vertical distribution time series of the fraction of flash channel parcels remaining within 2 km of initiation height for these storms. Notice the deeper concentration of flash channel parcels in purple within the mid-

levels of these two cases compared to the three Colorado cases (see Figs. 3.5, 3.6, and 3.7). These figures show that over half of the parcels originating in the mid-levels (6-12 km) of these storms remain within 2 km of their initial heights. Figure 3.15 also quantifies this for each vertical level of the May 18 Alabama case where more than 50% of the parcels in each normalized bar remain unhatched. This is vastly different than that for the anomalous polarity cases where vertical wind speeds are considerably stronger and small fractions of flash channel parcels remain within 2 km of their initiation heights throughout the mid-levels, especially for the June 6 storm (see Figs. 3.8 and 3.10). Moreover, Fig. 3.16 shows little change in the distribution of parcels by height and vertical wind speed both at parcel initiation (left) and after advection (right) compared to Fig. 3.11 for the June 6 storm. Figure 3.17a summarizes these claims for these two normal polarity storms, showing that more than 25% of all flash channel parcels initiate and remain above 8 km (red bars), more than the three Colorado anomalous storms (especially the less intense June 27 and 28 storms).

### 3.5. Comparison between all storm cases

#### 3.5.1 Differences in advection

The height where flash channel parcels initiate appears to vary significantly between each storm type, therefore influencing their advection. In the normal polarity cases, the average mode height is  $\sim 8$  km, versus  $\sim 5$  km in the anomalous polarity cases. Since updraft and downdraft maxima appear to be relatively weak (staying within  $\pm 10 \text{ ms}^{-1}$ ) at these heights in the normal polarity cases, the abundance of parcels that initiate at this height do not undergo strong advection and move much more than 2 km in height. Figure 3.17 summarizes the vertical advection of flash channel parcels, quantifying the transport for each of the cases around 8 km

altitude – a height marking the bottom of the upper troposphere for this study as previously discussed. Though variable from case to case, several observations in trend are common for each storm. First, about half of all flash channel parcels initiate and remain below 8 km (blue bars) for each of the five cases. This signifies that less advection occurs for the lowest initiating parcels. Second, the fraction of parcels that initiate above and advect to below 8 km (green bars) remains small for each case, showing that strong downward transport of LNO<sub>x</sub> from upper levels is minimal for each polarity structure. This is not surprising as it is difficult for downdrafts to fully penetrate the boundary layer, especially starting from at and above 6 km where most parcels originate amongst the cases.

Two distinct differences appear between the Colorado anomalous and Alabama normal polarity storms from this figure. In the normal polarity storms, a greater fraction of flash channel parcels initiate and remain above 8 km. The maxima in updrafts also appear to occur near this level so it makes sense that a higher fraction of flash channel parcels initiate and remain above 8 km. Weak downdrafts would also be capable of transporting parcels downward, helping account for the large fraction of parcels that initiate and remain below 8 km (blue bars). On the other hand, a larger fraction of parcels initiate below 8 km and advect to a final height above 8 km (purple bars) in the anomalous polarity Colorado cases. Figures 3.5, 3.6, and 3.7 show that most parcels initiate just below or at the base of the strongest updrafts during periods when the updraft volume is largest. This enhanced advection would easily be capable of advecting parcels from 4-8 km upward to final heights above 8 km. Parcels would also likely be undergoing positive vertical acceleration, capable of transport to levels above 8 km of the storms. Regardless, the total fraction of parcels that end above 8 km after parcel advection (black bars) appears uniformly around 50% for all cases. From this, we can conclude that both normal and anomalous

polarity thunderstorms appear to produce a relatively equal proportion of flash parcels to the upper troposphere ( $z > 8$  km MSL) resulting from two different processes for each polarity structure. Advection resulting from enhanced updraft strength and volume appears to dominate the number of flash channel parcels ending above 8 km in the anomalous cases, while location ultimately determines the resulting final locations above 8 km of flash parcels in the normal polarity cases. The fact that significantly more flashes and channel length occurs in the anomalous cases leads to a net larger quantity of flash channel parcels entering the upper troposphere. This has important consequences as will be discussed in Section 3.6 when it comes to LNO<sub>x</sub> mixing ratios.

Figure 3.18 demonstrates the net effect of advection on the vertical distribution of total FCL for each storm. In this figure, flash channel parcels, each representing 1 km of FCL, are integrated along the vertical axis for each storm. The enhanced vertical motions in the three anomalous polarity Colorado storms has a clear impact on the final profile of total FCL after advection (“Adveted”) compared to the original vertical distribution (“Original”). The bimodal redistribution of parcels seen in Figs. 3.5, 3.6, and 3.7 for the anomalous storms is well displayed in the “Adveted” profiles. However, the placement of flash channel parcels at greater heights and weaker vertical winds causes less redistribution of the parcels and so the “Adveted” curves remain more tightly bound to the “Original” curves for the normal polarity Alabama cases.

### 3.5.2. Microphysics, charging, and initial parcel locations

Examining flash channel parcel initiation in relation to reflectivity also reveals several interesting findings. First, flash channels appear to occur more frequently just downwind of reflectivity cores. This is demonstrated especially well in the June 6 Colorado anomalous storm in Fig. 3.3 where the densest areas of FCL contouring appear just east of the reflectivity core –

slightly down shear of the main updraft. Weiss et al. (2012) also found a tendency for flashes to traverse regions down wind of the main updrafts of supercells. Vertical wind speeds are lower outside these areas as well, which would allow for more graupel fallout. Non-inductive charging theory states that most charge transfer tends to occur between graupel and ice crystals, so greater charge transfer can occur and stronger electric fields can build in these areas (e.g. Workman and Reynolds 1950; Takahashi 1978; Jayaratne 1983; Dye et al. 1986). Figure 3.3 shows that indeed, the densest concentration of FCL appears to occur in volumes of predominantly hail (red), high density graupel (yellow), and low density graupel (green) hydrometeor regions of the June 6 storm. As hydrometeors continue to collide, positive and negative charge zones build with an electric field strengthening between. Eventually, air between these charge zones breaks down and lightning occurs (Williams 1985). Though not as compelling, similar trends in flash channel contouring appear for the other four storms considering the shear appears to be lower (see Figs. 3.4 and 3.12).

It makes sense that most flash channels occur in areas surrounding storm updraft cores as high shear occurs in the vertical wind, likely aiding in the collision efficiency between hydrometeors. In fact, Fig. 3.19 shows that nearly 75% of flash channel parcels appear to initiate in areas of weaker vertical motions ( $|w| \leq 5 \text{ ms}^{-1}$ ) and lower reflectivity for all five cases. Also, relatively few flash channels (< 15%) appear to occur in areas with updrafts/downdrafts exceeding  $10 \text{ ms}^{-1}$  or reflectivity values over 60 dBZ. This is remarkably similar to findings for a storm in Northeast Colorado during the STERAO field campaign in 1996, where a majority of flash sources were located in moderate updrafts downshear of the main storm updraft and downdraft (Dye et al. 2000). In that study, Dye et al. (2000) acknowledges the difficulty yet importance in obtaining lightning spatial and temporal coverage in relation to storm convective

motions, highlighting the importance of this study in providing observational insight into understanding where lightning occurs.

Further investigation reveals that most flash channels appear to originate outside the strongest reflectivity echoes among the five cases (see Fig. 3.20). This is not surprising considering that most flash channels were located just down shear of the main convective updrafts with higher reflectivity as seen in Figs. 3.3, 3.4, and 3.12. The right-hand plots of Fig. 3.8 and 3.9 provide a clearer view of the number of parcels initiating within various reflectivity volumes with height. While there is more initiation in high reflectivity volumes in the June 6 storm, relatively similar fractions of parcels appear to initiate within each reflectivity threshold, regardless of storm region/polarity (though less initiate in higher reflectivity values above 6 km in the June 11 Alabama storm). Figure 3.20 quantifies these initiations for all heights within each storm showing the fraction of parcels initiating within each reflectivity volume. Note that the 10 dBZ volume includes all higher reflectivity values (20 dBZ, 30 dBZ, 40 dBZ, 50 dBZ etc.) so all bars need not sum to unity for each storm. Notice that over 75% of flash channel parcels initiate within reflectivity values of at least 20 dBZ. The weaker June 11 Alabama storm merged with a weaker, decaying cell, which can also be seen in the smaller fraction of parcels initiating within at least 30 dBZ. These results confirm the 20 dBZ horizontal flash channel and subsequent LNO<sub>x</sub> findings of MacGorman and Rust (1998) used in the modeling techniques of DeCaria et al. (2000, 2005). This methodology appears valid considering these results between two sets of different storms from different regions and environments.

In terms of hydrometeor type, most flash channel parcels originate in areas predominantly identified as either low and high density graupel or hail for all cases except the June 11 Alabama storm. For example, Fig. 3.21 shows that over 30% of flash parcels in four of the five cases

originate in areas predominantly composed of low density graupel, with aggregates, rain, high density graupel, and hail as the next most predominant species. In the June 11 Alabama case, most flash channel initiations occur in aggregates, with low density graupel being the second most common hydrometeor initiation species. This is likely a result of the storm merger with a decaying storm with reflectivity values  $< 35$  dBZ during the middle of its lifetime. The larger volume of weaker vertical motion was not sufficient to produce a larger graupel and hail volume, leading to a large remaining volume of aggregates. All remaining charge equilibrated in these areas after the merger. One limitation to the HID approach is that not all hydrometeors within each grid cell are necessarily of the identified species, rather they are the most likely dominant hydrometeor specie based on radar and sounding observations. The fact that these results across all five storms fit nicely with non-inductive charging theory (i.e. most flash channels initiating between ice crystals and graupel) described by Workman and Reynolds (1950), Takahashi (1978), Jayaratne et al. (1983), and others makes this limitation less discouraging.

### 3.6. LNO<sub>x</sub> concentrations

#### 3.6.1. Calculations

Now that flash channels have been gridded and parcels have been advected and tracked through each storm, LNO<sub>x</sub> can be attributed to the parcels in order to investigate the upper tropospheric NO<sub>x</sub> impact from each storm. The process of producing LNO<sub>x</sub> from lightning has been studied in lab settings, and so we follow a common parameterization method from DeCaria et al. (2000) and Wang et al. (1998) as discussed in section 2.5. This method produces LNO<sub>x</sub> at a given pressure per unit channel length. This parameterization is dependent upon pressure as the availability of diatomic nitrogen and oxygen to encounter flash channels decreases with

increasing height. Figure 3.22a shows profiles of the total lightning produced  $\text{NO}_x$  profiles for each storm before (dotted line = “Original”) an after advection (solid line = “Advection”).  $\text{LNO}_x$  is calculated for each parcel using its initial pressure as interpolated from the nearest/closest National Weather Service sounding (see Appendix A) and then summed for each vertical level. Note that the May 19 0000 UTC KBMX sounding for the May 18 Alabama storm was incomplete, so the May 18, 1200 UTC KBMX sounding was used instead. “Original” lines are summed  $\text{LNO}_x$  values if parcels were kept stationary at their initiation locations when and where flash channels occurred. “Advection” lines are calculated after all flash channel parcels have undergone advection from the storm winds.

Calculating the  $\text{LNO}_x$  mixing ratios proceeds as follows. For the vertical profiles of each storm, the total concentration of  $\text{LNO}_x$  is computed for each level as a sum for all parcels at that level. The parcels are then interpolated onto an empty 3-D grid at 1.0 km resolution and the total number of grid cells containing parcels is summed for each vertical level and converted to moles of air via the Ideal Gas Law. Figure 3.23 shows the number of grid cells or volume the parcels are contained within for each storm after advection has taken place to calculate these mixing ratios. With these, the moles of air are calculated for each level in each case and the fraction of moles of  $\text{LNO}_x$  to moles of air in parts per billion (ppb) are calculated for each vertical level in each case. Note that this method includes all flash parcels after advection for the “Advection” plots, even if they exited the tracked cell volume at the end of the storm lifetime. These results can be seen in Fig. 3.22b.

### 3.6.2. Anomalous polarity cases

After closer examination, upward transport of flash channel parcels (and  $\text{LNO}_x$ ) clearly dominates in the anomalous polarity cases. For example, 63% (June 6), 84% (June 27), and 40%

(June 28) of the final advected LNO<sub>x</sub> profiles above 8 km is contributed to by flash channel parcels that were advected upward by 2 km or more compared to only 12% (May 18) and 8% (June 11) in the two normal polarity storms. The profiles after advection for the June 6 and 27 anomalous storms are nearly a reversal of the original profiles before advection took place where parcels transition from one mode in height to two. This is not surprising considering these two storms produce the most flash channel parcels and the vertical wind speeds that many parcels initiate within were much greater (see Figs. 3.8 and 3.19). This tendency for enhanced vertical transport is comparable to Ott et al. (2010) who found enhanced LNO<sub>x</sub> mass fractions above 8 km for modeled mid-latitude storms, though less defined than what is seen for these three anomalous polarity storms. They also found a resulting bimodal distribution in the LNO<sub>x</sub> profile after convection but with a lower mode at approximately 4.5 km rather than near or in the boundary layer. Updraft volumes exceeding 5 ms<sup>-1</sup> peaked at higher values (~800 km<sup>3</sup> for June 6 storm and ~400 km<sup>3</sup> for the June 27 storm) and volumes remained larger throughout the storm lifetimes compared to the other cases (see Figs. 3.5 and 3.6). Note that the mixing ratio maxima in Fig. 3.22b appear larger than the concentration profiles in Fig. 3.22a because pressure and air density are lower in the upper portion of storms. While the mixing ratio of LNO<sub>x</sub> above 8 km after advection in the June 28 case is lower than that of the other two Colorado cases, the volume into which parcels were distributed was much larger, therefore causing a lower density of LNO<sub>x</sub> at these levels. The updraft volume of this storm remained lower over its lifetime than the other two anomalous storms, but larger over the storm's duration than that for the two Alabama cases.

Overall for these three anomalous storms, 14% of all flash channel parcels originated in updrafts  $\geq 5 \text{ ms}^{-1}$  compared to 7% in the normal polarity cases (16% to 8% when factoring out parcels that started in areas without sufficient hydrometeor content needed to determine wind

velocities by Doppler radar). These results suggest that the enhanced updraft strength and updraft width characteristic of anomalous storms helps to transport LNO<sub>x</sub> formed from FCL upward to final heights above 8 km. This artifact is well represented in Fig. 3.22c where the vertical profiles of LNO<sub>x</sub> contributed to by parcels advecting upward, downward, or within 2 km are normalized by the total LNO<sub>x</sub> production in the storm. Results from this reveal the larger fraction of LNO<sub>x</sub> above 8 km in the anomalous Colorado cases contributed to by upward advected parcels. On the other hand, the fractions of LNO<sub>x</sub> at every level above 6 km contributed to by parcels remaining within 2 km of their initiation heights is much larger for the two normal polarity Alabama cases, further suggesting that parcels and LNO<sub>x</sub> tended to remain closer to where formed.

### 3.6.3. Normal polarity cases

LNO<sub>x</sub> concentration and mixing ratio profiles appear to remain more uniform with height for the normal polarity cases in Alabama. There is some upward transport from 10-12 km evident in Fig. 3.22c, but not nearly the extent to that seen in the anomalous polarity storms. This is congruent with the lower proportion of flash channels initiating within intense updrafts in these cases. Updrafts tended to remain weaker as seen in Figs. 3.13d and 3.14d, creating less available potential upward transport volume for flash channels to traverse. With this, less LNO<sub>x</sub> is created in rising updraft parcels, causing it to remain near levels at which it is created. While the proportion of flash channel parcels ending above 8.0 km is still around 50% in these two cases, more parcels originated at or above 8.0 km to begin with, meaning the contributions of these normal polarity cases to upper tropospheric NO<sub>x</sub> is driven more so by flash channel initial locations (above 8.0 km) than by vertical advection. Moreover, a larger proportion of parcels tended to stay within 2 km of their originating heights in these cases than the anomalous cases

according to Fig. 3.9. While only two cases of normal polarity cases were analyzed, they appear representative of average storm structure for northern Alabama following studies by Fuchs et al. (2015, 2016), and Fuchs (2017). These resulting vertical profiles of LNO<sub>x</sub> compare well to those for modeled subtropical storms by Ott et al. (2010) who found a “C-shaped” vertical profile with a mode in LNO<sub>x</sub> mass fractions also around 8 km.

Figures 3.24-3.28 show two dimensional cumulative distributions of the LNO<sub>x</sub> mixing ratios of the storms before and after advection of the flash channel parcels. Mixing ratio values were computed similarly to those in Fig. 3.22b but not just along the vertical axis. Instead of summing all the grid cells with parcels for each level when calculating the number of moles of air, parcels are added to grid cells at each z- and y-distance locations existing along the x-axis into and out of the page to calculate the background volume of air. If there are less grid cells to contain parcels in these two dimensions than for the corresponding whole level of the storm, as is used in Fig. 3.22b, the mixing ratio will be higher for these locations. Therefore, values show more detailed areas of higher LNO<sub>x</sub> concentrations with this added dimension, especially in the June 6 storm. This figure also serves as a good representation of the stronger vertical advection at play in this case leading to the bimodal final distribution of LNO<sub>x</sub>. The larger values found near 13 km in the anomalous cases follows other studies where most LNO<sub>x</sub> was found to reside in the anvil of storms after they begin to decay (e.g. Ridley et al. 1996; Huntrieser et al. 2016). However, the LNO<sub>x</sub> mixing ratios appear much more uniform in the vertical for the normal polarity cases with no clear upper level maxima, not just in the anvil as in the anomalous storm cases. Figure 3.23 shows the number of grid cells that parcels are contained within after advection has taken place. Notice that flash channel parcels are distributed within fewer grid cells with height in the May 18 case (purple curve) than the June 11 case (green curve), yet the May 18 case produced more flash

channel parcels in total. Therefore, the  $\text{LNO}_x$  concentration is confined to less storm volume in the May 18 case and explains the enhanced mixing ratio values in the “After Advection” for this storm compared to that in the June 11 storm.

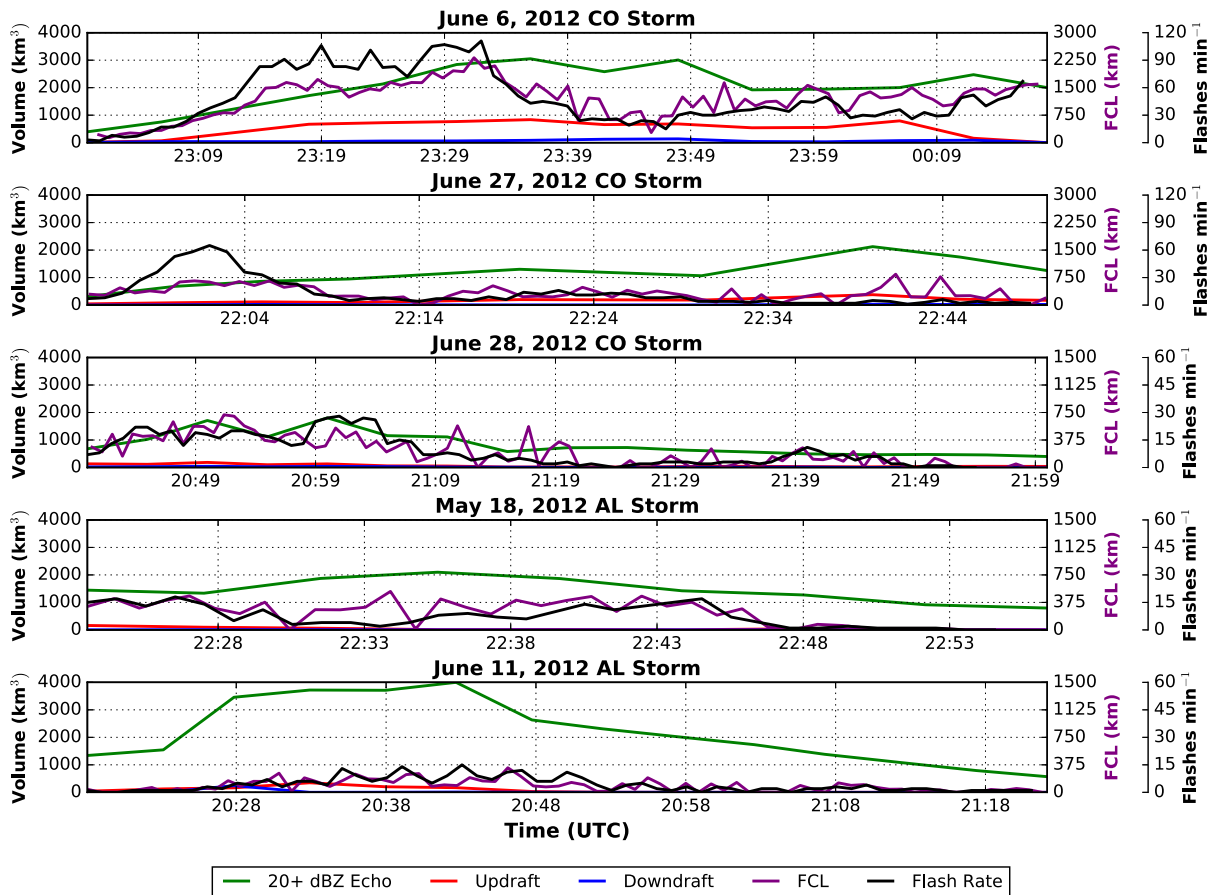


Figure 3.1: Various storm volumes, total FCL (purple), and flash rate (black) over each storm’s lifetime. Reflectivity echo volumes at or above 20 dBZ are in green, updraft volumes at or above  $5 \text{ ms}^{-1}$  are in red, and downdraft volumes at or above  $5 \text{ ms}^{-1}$  are in blue. Left y-axes correspond to all volume time series, “FCL (km)” y-axes correspond to total FCL time series, and “Flashes  $\text{min}^{-1}$ ” y-axes correspond to flash rate time series. Note that the right y-axes of the bottom three storm plots are half of the first two upper plots.

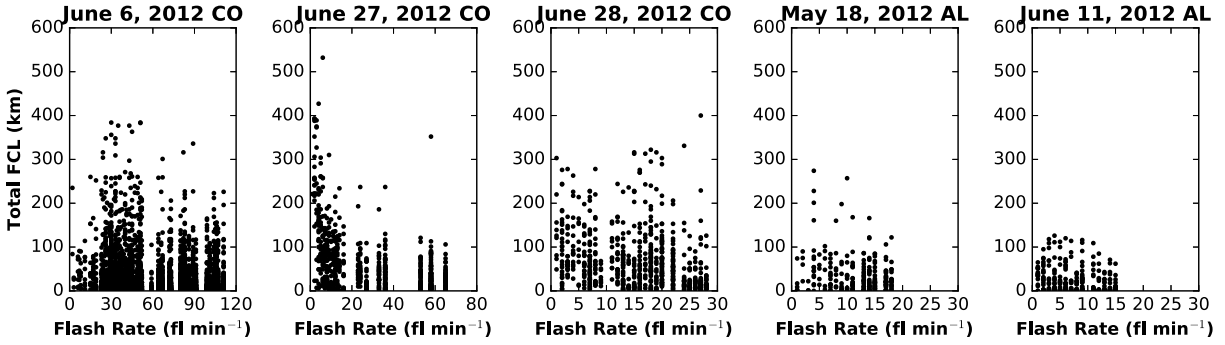


Figure 3.2: Scatterplot of flash rate to total FCL for each flash in each storm. As the flash rate increases in storms the total channel length appears to decrease. Several outlier flashes with high flash rates and extended channel length appear for the June 28, 2012 Colorado storm. Note that the x-axes differ among these subplots.

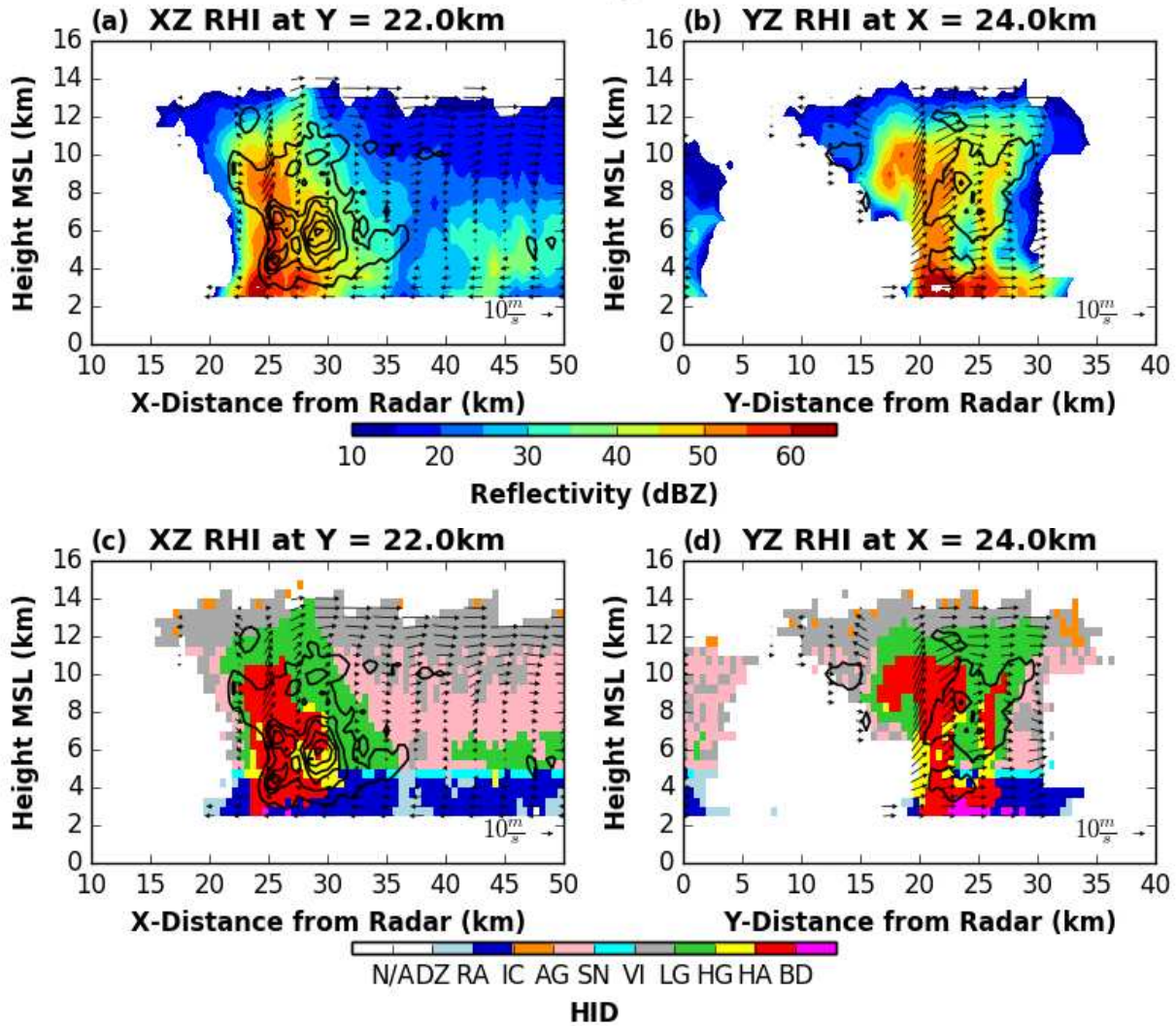


Figure 3.3: Reflectivity and HID cross sections through the June 6, 2012 CO thunderstorm at 2329 UTC. (a): reflectivity cross section along X-Z axes at  $y = 22.0$  km with U, W wind vectors. (b): reflectivity cross section along Y-Z axes at  $x = 24.0$  km with V, W wind vectors. (c) and (d): same as (a) and (b) but for HID fields. HID fields are not applicable (“N/A”), drizzle (“DZ”), Rain (“RA”), ice crystals (“IC”), aggregates (“AG”), snow (“SN”), vertical ice (“VI”), low-density graupel (“LG”), high-density graupel (“HG”), hail (“HA”), and big drops (“BD”). FCL contoured in black at 2.5, 10, 15, 20, and 25 km. Note that ground level is  $\sim 1.7$  km for this Colorado case.

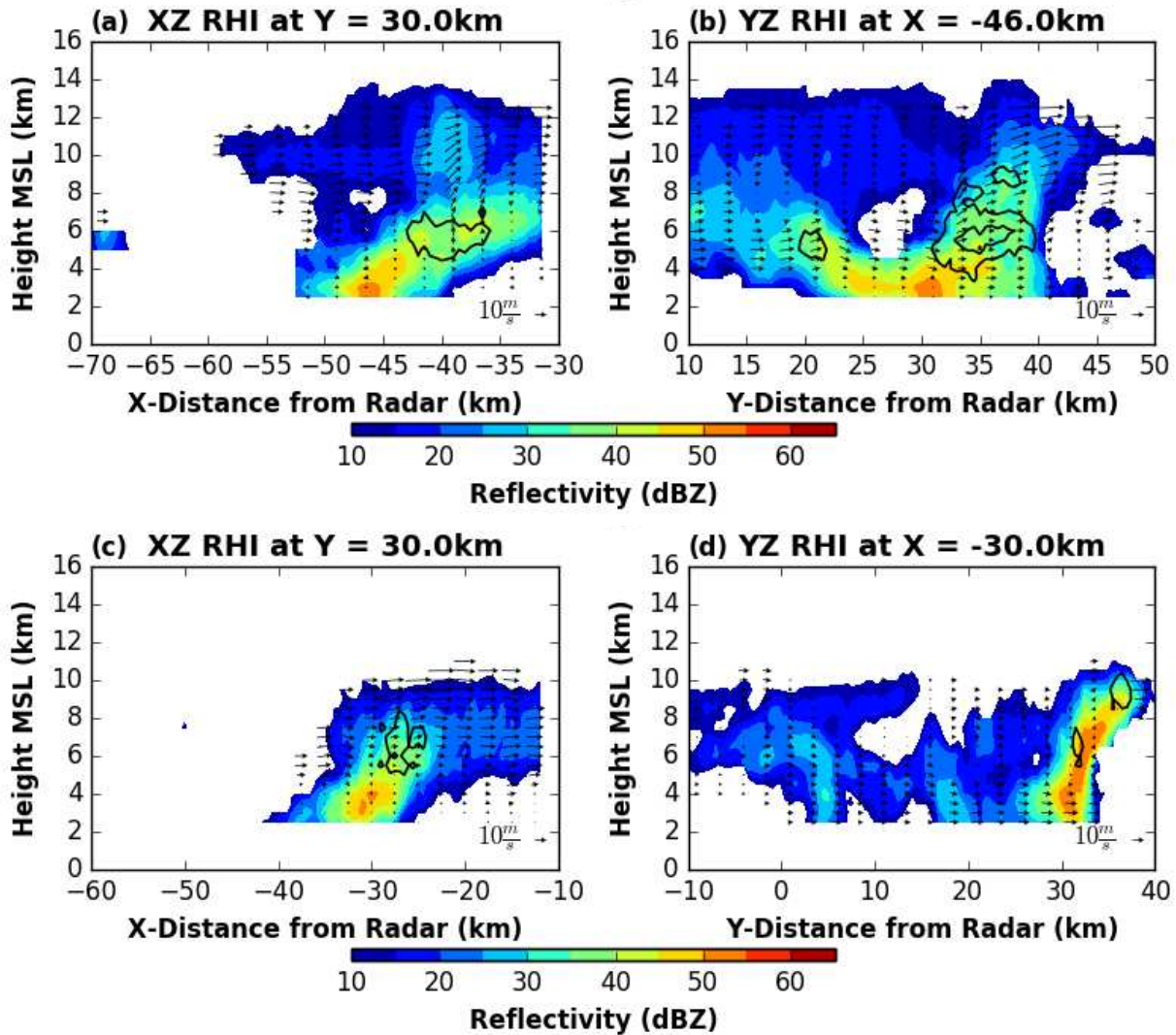


Figure 3.4: Vertical reflectivity cross sections through the June 27, 2012 CO thunderstorm at 2239 UTC (a, b) and June 28, 2012 CO thunderstorm at 2144 UTC (c, d). (a): cross section along X-Z axes at  $y = 30.0$  km with U, W wind vectors. (b): cross sections along Y-Z axes at  $x = -46.0$  km with V, W wind vectors. (c): cross section at  $y = 30.0$  km with U, W wind vectors. (d): cross section at  $x = -30.0$  km with V, W wind vectors. FCL contoured in black for both plots at 2.5, 10, 15, 20, and 25 km. Note that ground level is  $\sim 1.7$  km for the Colorado case.

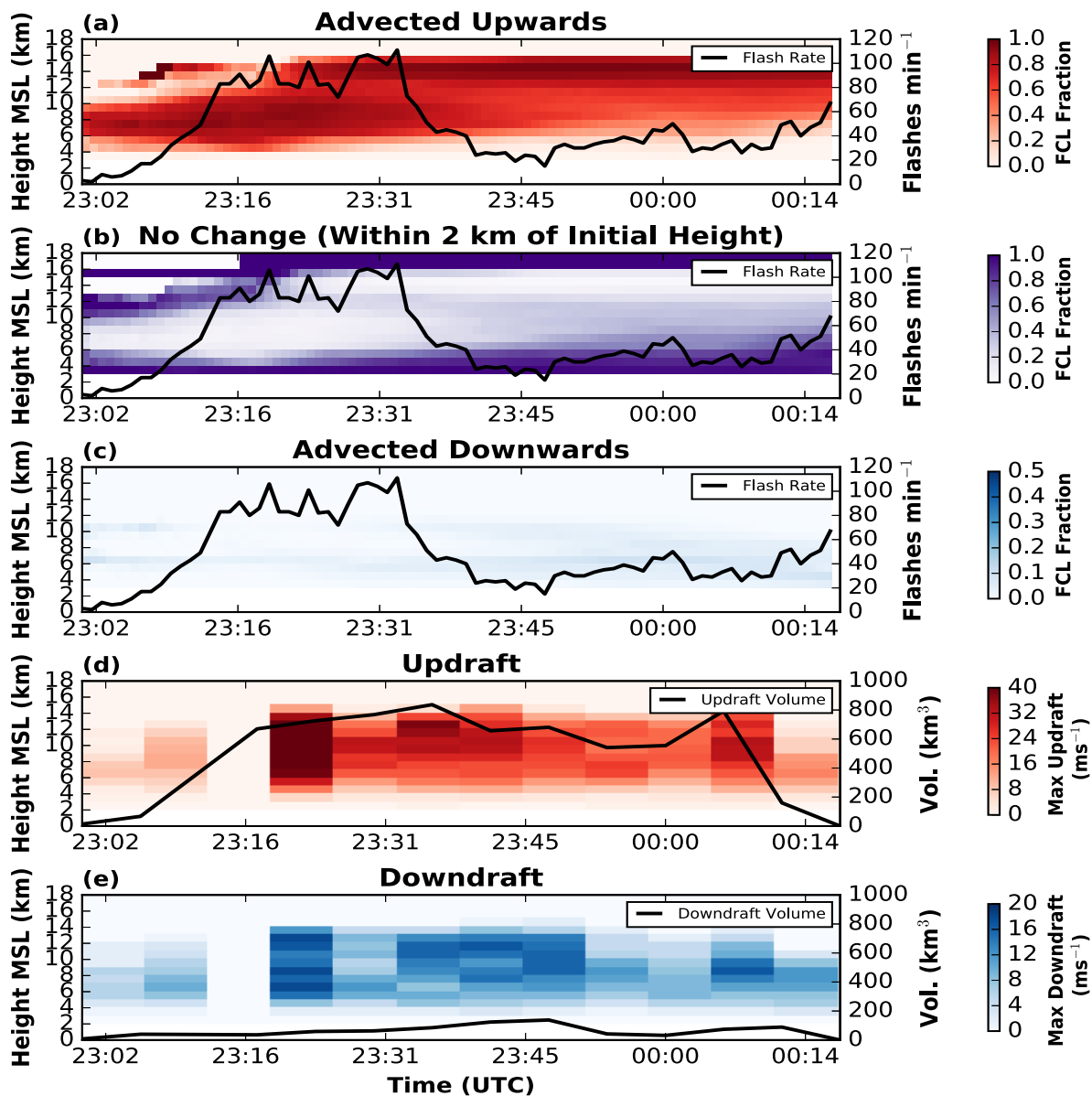


Figure 3.5: Time series of storm intensity parameters for the June 6, 2012 Colorado storm. (a): time series of the fraction of total FCL at each 1 km height in the storm advecting upward more than 2.0 km from initiation and flash rate (black line). (b) time series of the fraction of total FCL at each 1 km height in the storm remaining within 2.0 km of initiation and flash rate (black line). (c): time series of the fraction of total FCL at each 1 km height in the storm advecting downward more than 2.0 km and flash rate (black line). (d): maximum updraft at each level of storm and total updraft volume exceeding  $5.0 \text{ ms}^{-1}$  (black line). (e): maximum downdraft at each level of storm and total downdraft volume exceeding  $5.0 \text{ ms}^{-1}$  (black line). Note that ground level is  $\sim 1.7$  km for this storm.

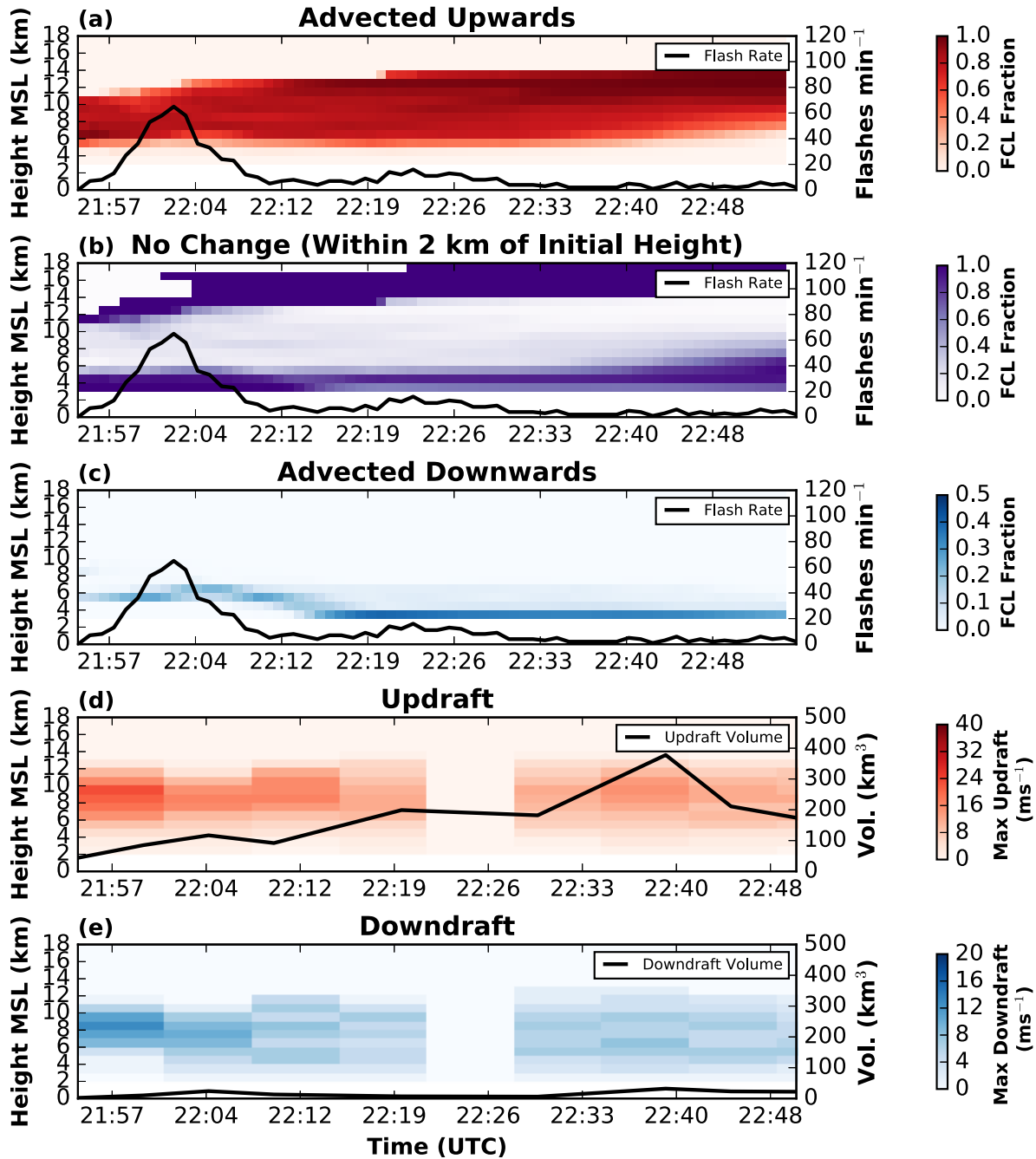


Figure 3.6: Same as Fig. 3.5 except for the June 27, 2012 Colorado case.

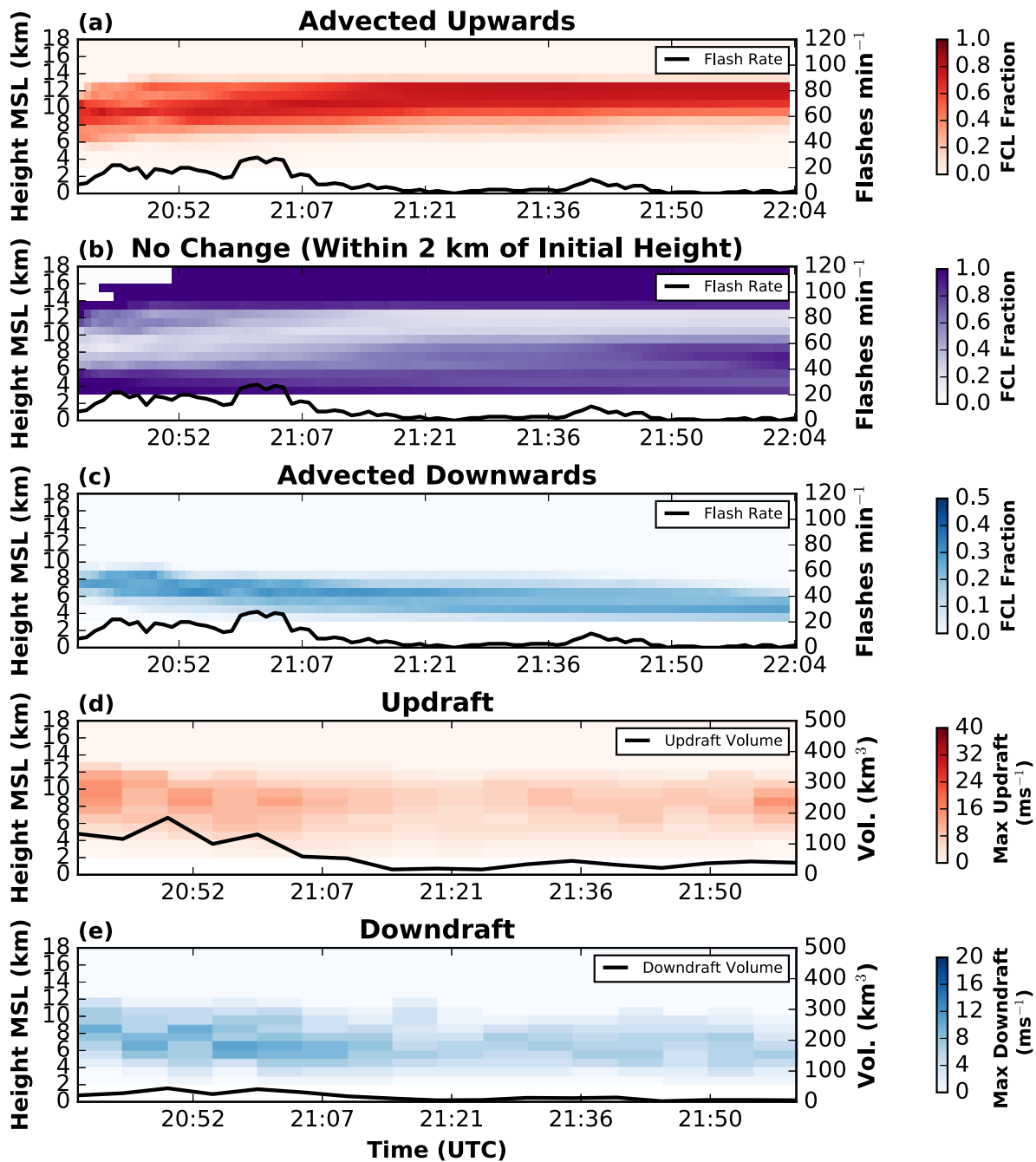


Figure 3.7: Same as Fig. 3.5 except for the June 28, 2012 Colorado case.

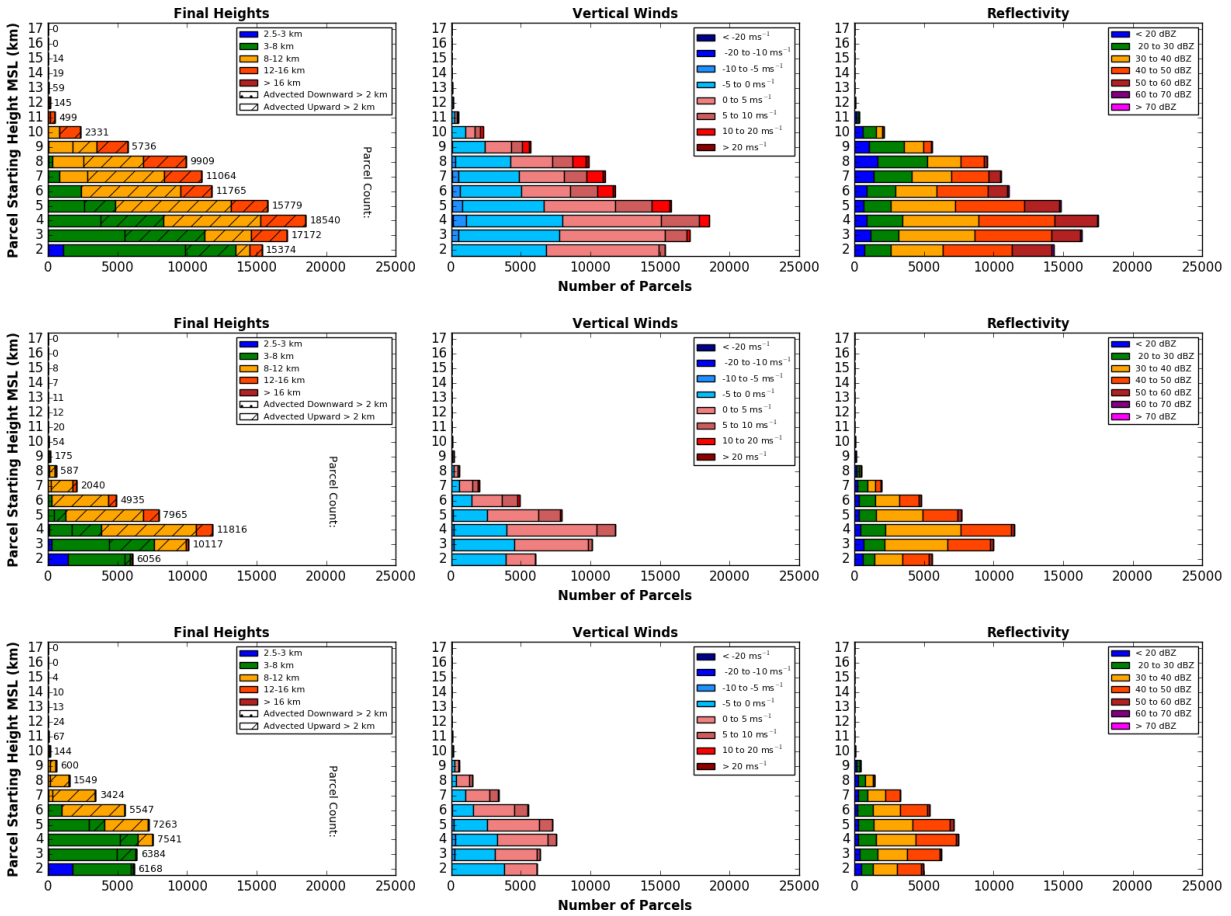


Figure 3.8: Bar plots of the vertical distribution of flash channel parcels by initiation height at 1 km increments for the June 6 (top), 27 (middle), and 28 (bottom), 2012 Colorado storm cases. Parcels are binned into 1 km vertical height increments based upon initiation height (note y-axis labels are lowest height in each 1 km increment). Left-most plots are colored by number of parcels advecting to various height ranges. Hatched areas represent parcels that end more than 2 km above initiation height, and dotted areas, represent parcels that end more than 2 km below initiation height. Note that dotted areas are quite small, further showing that transport of flash channel parcels by convective downdrafts is much less than that by updrafts. Number of parcels originating within each 1 km vertical height range are shown at the end of each bar. Middle column plots for each case are colored by vertical wind velocity ranges in which parcels initiate. Right-most plots are colored by reflectivity volume ranges with which parcels initiate. Note that ground level is  $\sim 1.7$  km in these three cases.

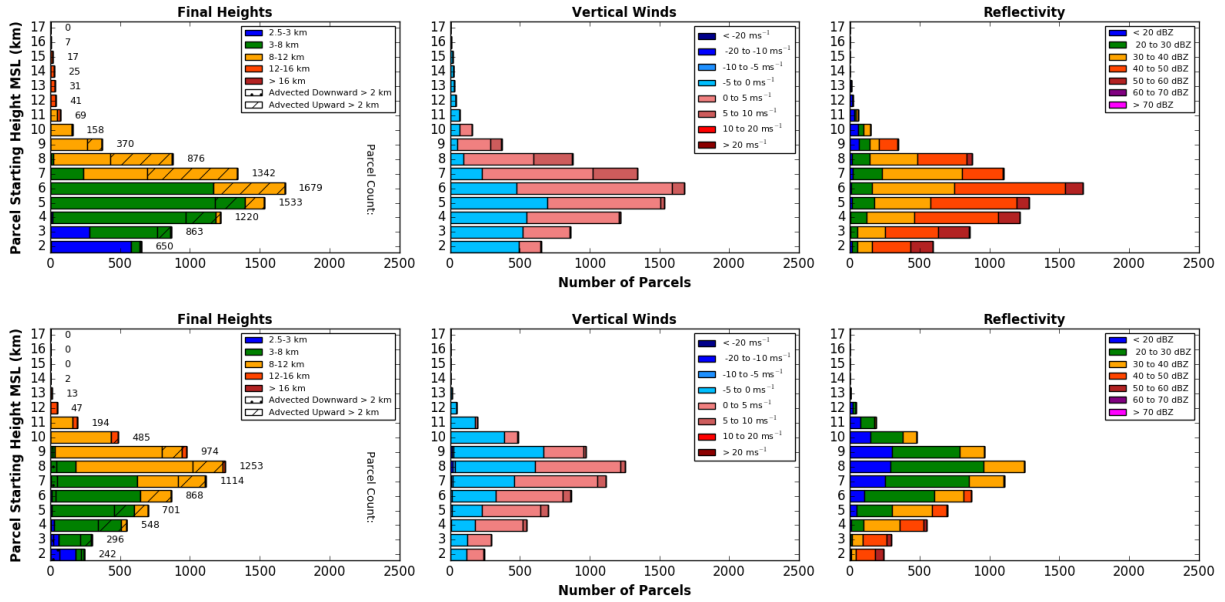


Figure 3.9: Same as Fig. 3.8 but for the May 18 (top) and June 11 (bottom), 2012 Alabama storm cases. Note the x-axis scale is one tenth that of the Colorado storms and ground level is  $\sim 0.2$  km in these cases. Also, downward transport more than 2 km (dotted sections of left-most plots) is quite limited for these storms, suggesting even less downward advection of parcels and associated LNO<sub>x</sub>.

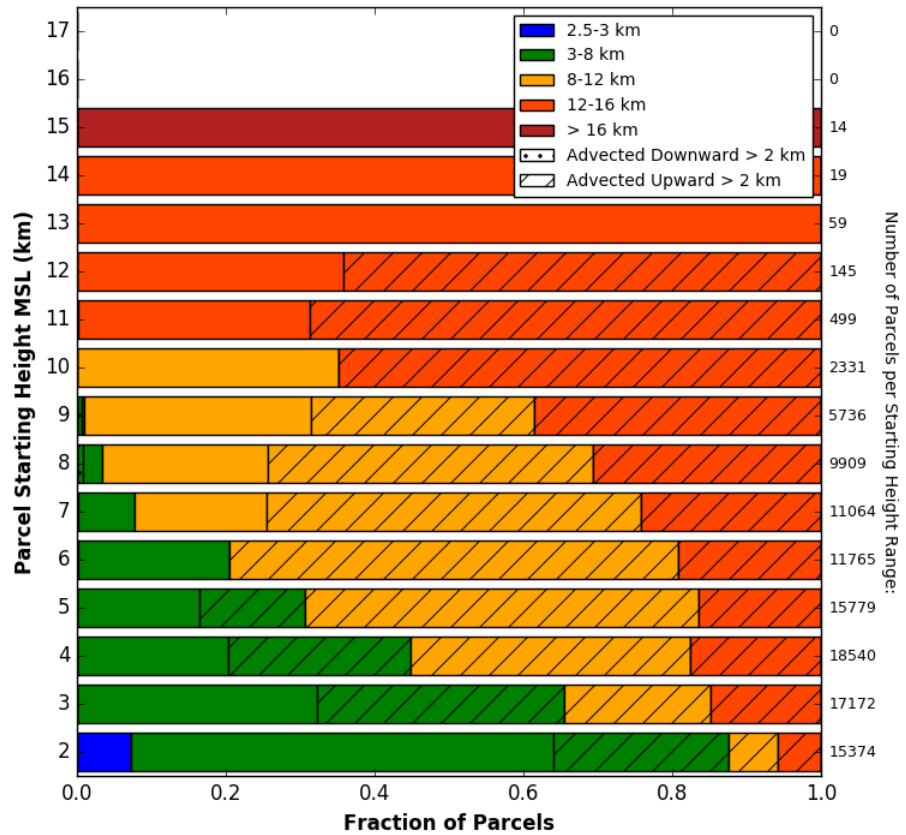


Figure 3.10: Normalized version of “Final Heights” plot for the June 6 Colorado storm in Fig. 3.8. Each colored final height bar at each vertical level is normalized by total number of flash channel parcels initiating at that corresponding level. Hatching represents parcels advecting upward more than 2 km from initial height, and dotted areas represent parcels advecting downward more than 2 km from initial height (very small amount for this storm). Number of parcels originating within each 1 km vertical height level are listed to the right.

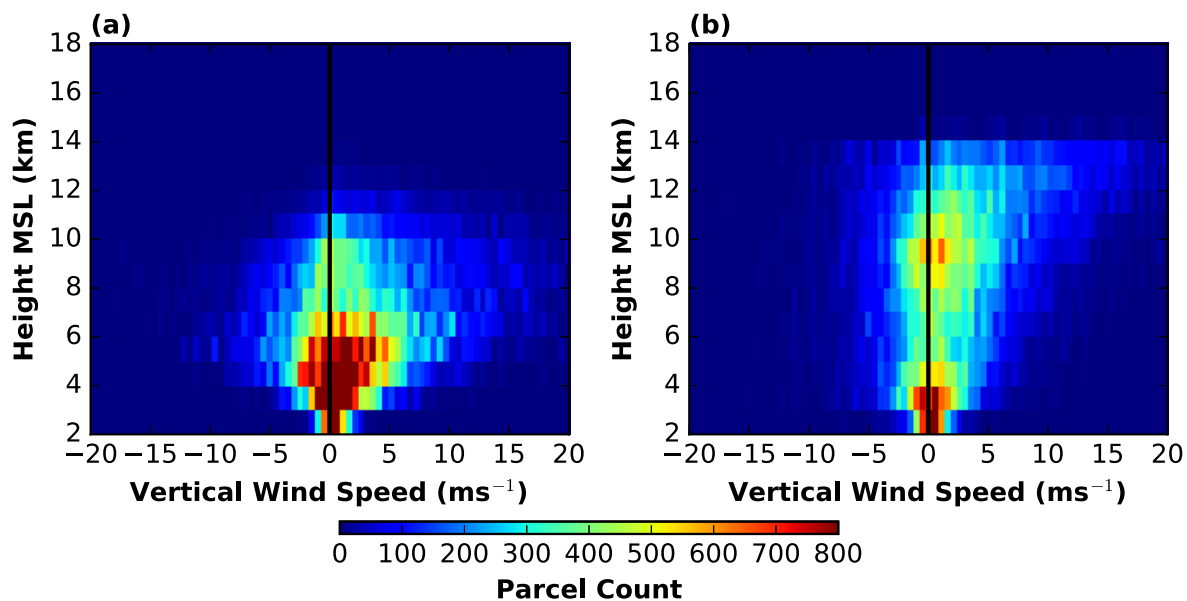


Figure 3.11: Cumulative distributions of flash channel parcels binned by initial vertical wind speed and initial height (a) and initial vertical wind speed and final height (b) for the June 6, 2012 Colorado storm. Notice the final bimodal distribution of parcels and the trend for parcels to end at heights above 8 km and to initiate in positive vertical motion in plot (b), suggesting deep upward transport of LNO<sub>x</sub>.

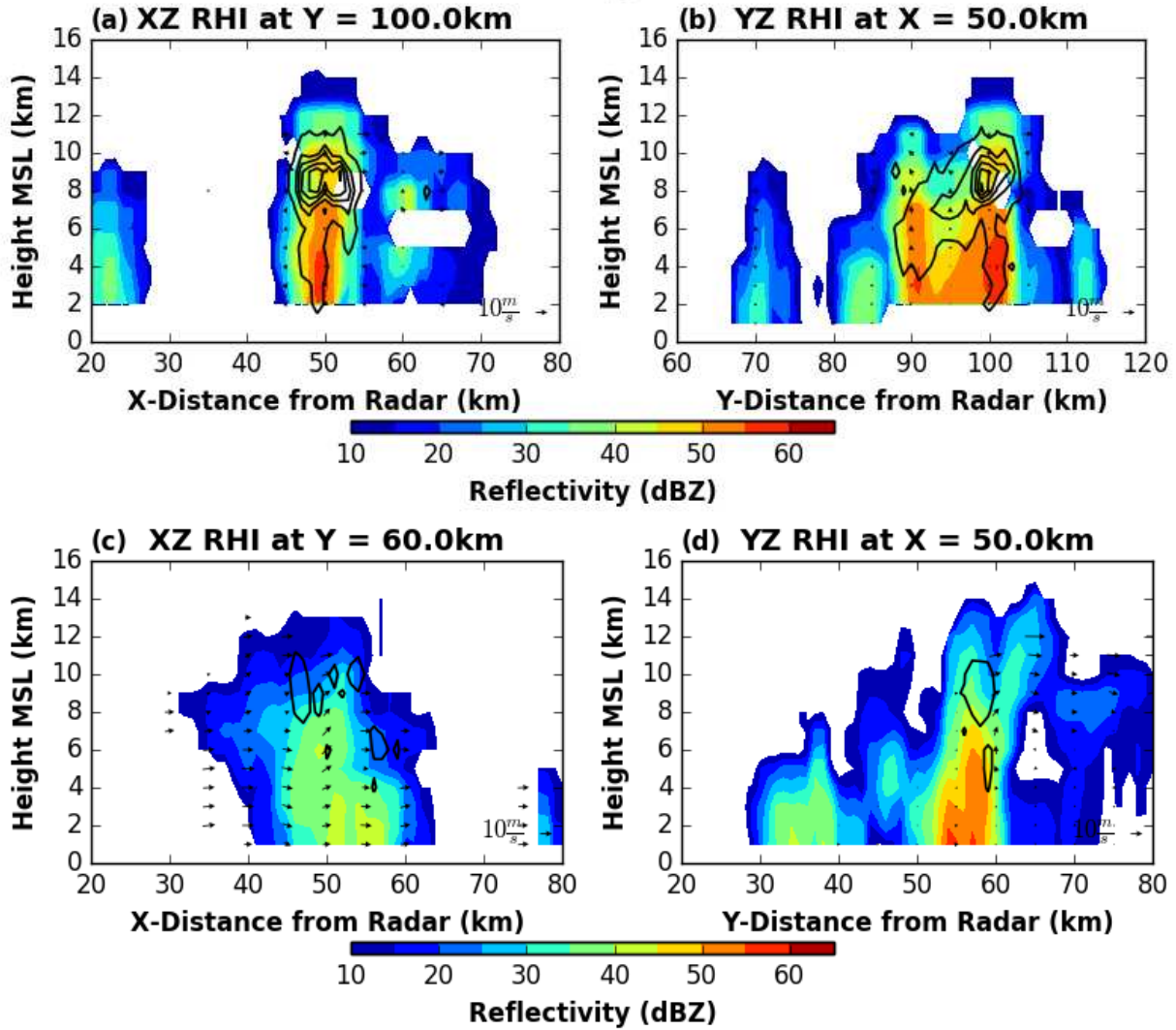


Figure 3.12: Vertical reflectivity cross sections through the May 18, 2012 AL thunderstorm at 2223 UTC (a, b) and June 11, 2012 Alabama thunderstorm at 2042 UTC (c, d). (a): cross section along X-Z axes at  $y = 100.0$  km with U, W wind vectors. (b): cross section along Y-Z axes at  $x = 50.0$  km with V, W wind vectors. (c): cross section along X-Z axes at  $y = 60.0$  km with U, W wind vectors. (d): cross section along Y-Z axes at  $x = 50.0$  km with V, W wind vectors. FCL contoured in black for both plots at 2.5, 10, 15, 20, and 25 km.

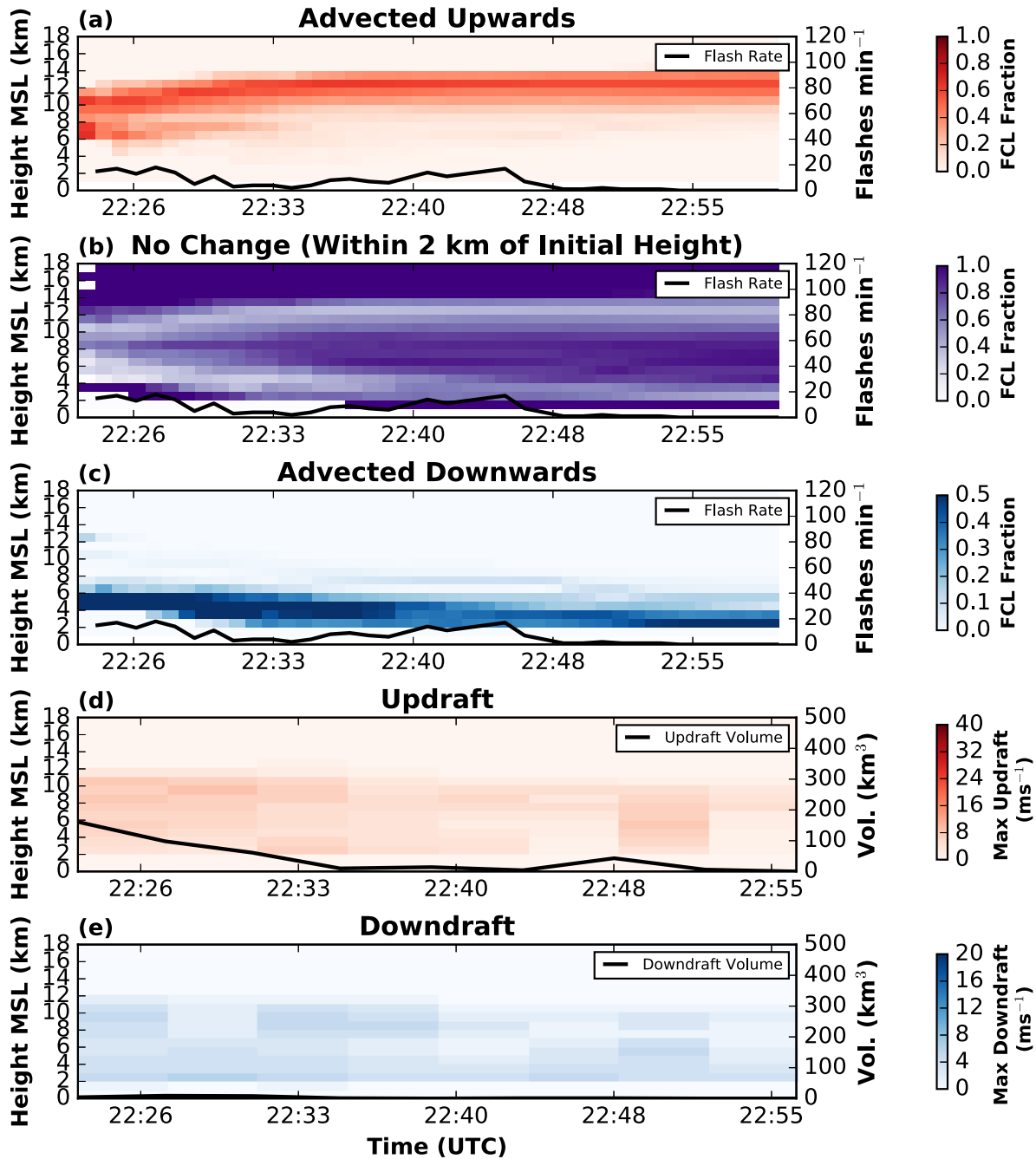


Figure 3.13: Same as Fig. 3.5 except for the May 18, 2012 Alabama storm. Note ground level is around 0.2 km in this case.

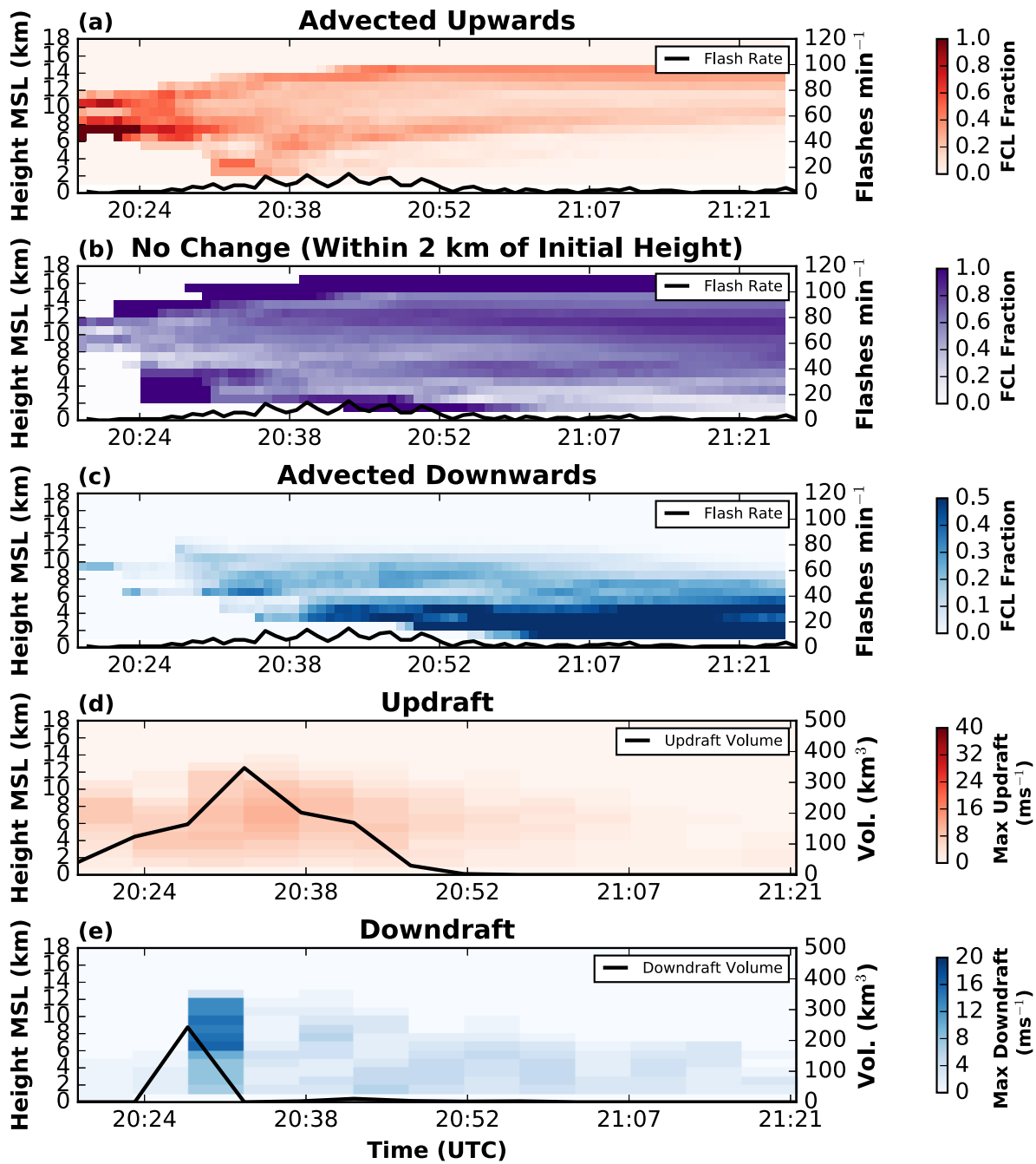


Figure 3.14: Same as Fig. 3.5 except for the May 18, 2012 Alabama storm. Note ground level is around 0.2 km in this case.

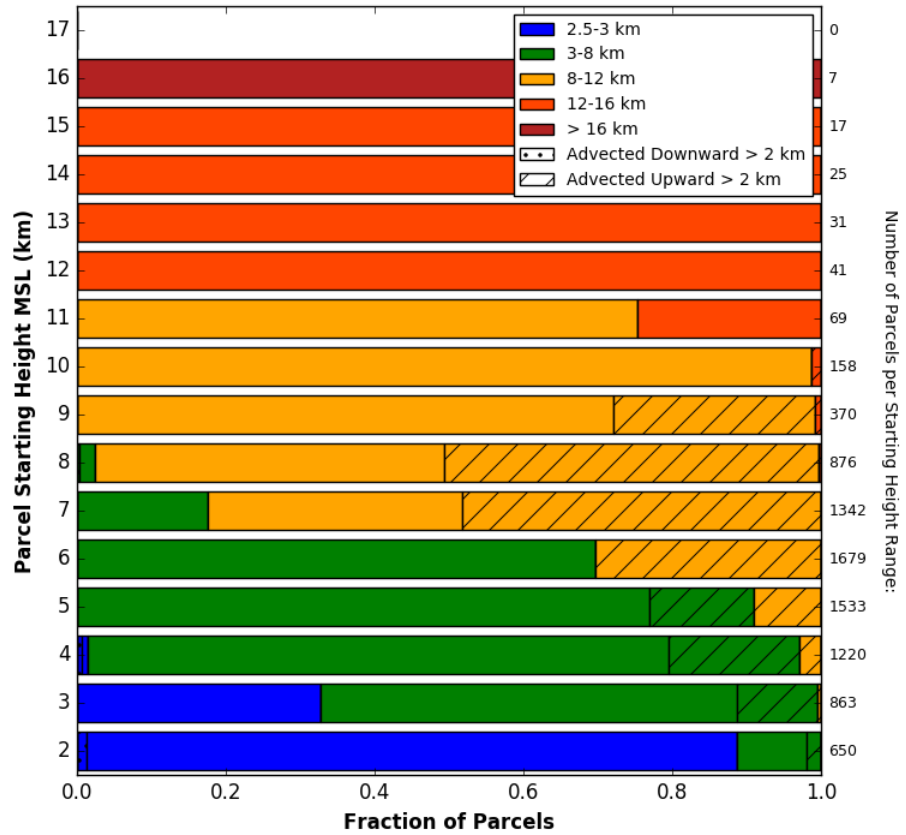


Figure 3.15: Same as Fig. 3.10 but for the May 18 Alabama storm and its respective flash channel parcels. Notice the reduced hatched fraction of parcels at each vertical level representing less parcels advecting upward more than 2 km.

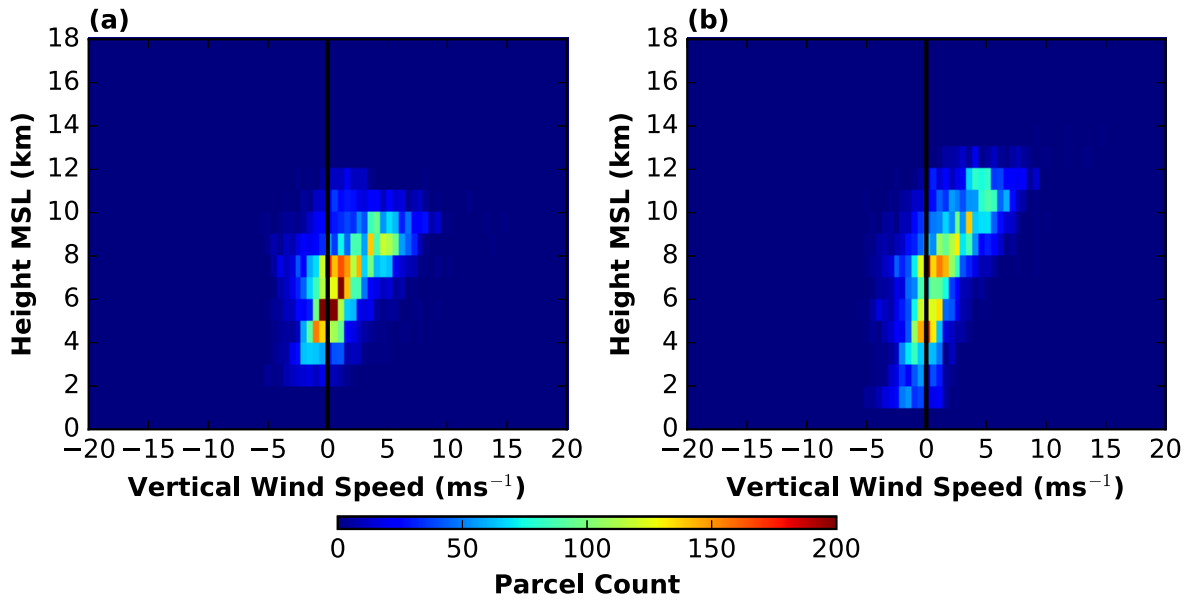


Figure 3.16: Same as Fig. 3.11 but for the May 18, 2012 Alabama storm. Note the color bar is scaled to one fourth that of Fig. 3.11 due to the significantly lower number of total flash channel parcels. Notice that less redistribution of parcels appears to take place from initial heights to final heights of parcels in the May 18 case whereas a more pronounced bimodal distribution with a larger concentration of parcels end above 8 km in the June 6 case.

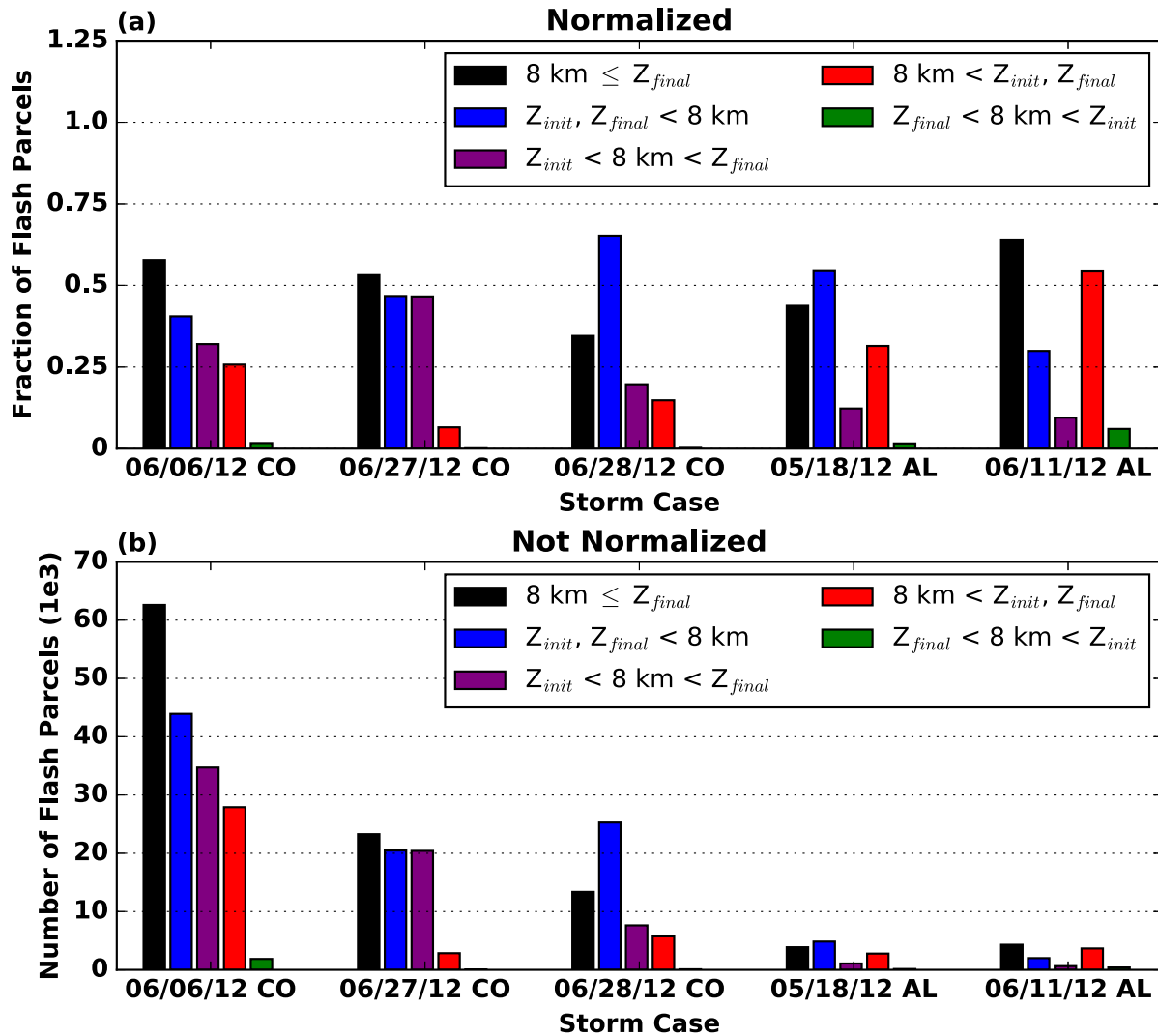


Figure 3.17: (a): fractions of all flash channel parcels advecting around 8.0 km for each thunderstorm and total amount of flash channel parcels advecting around 8.0 km not normalized for each thunderstorm (b). Notice around 50% of parcels end above 8.0 km for all cases (black bars). More parcels advect from below to above 8.0 km in the Colorado cases (purple bars) while more parcels initiate and remain above 8.0 km in the Alabama cases (red bars).

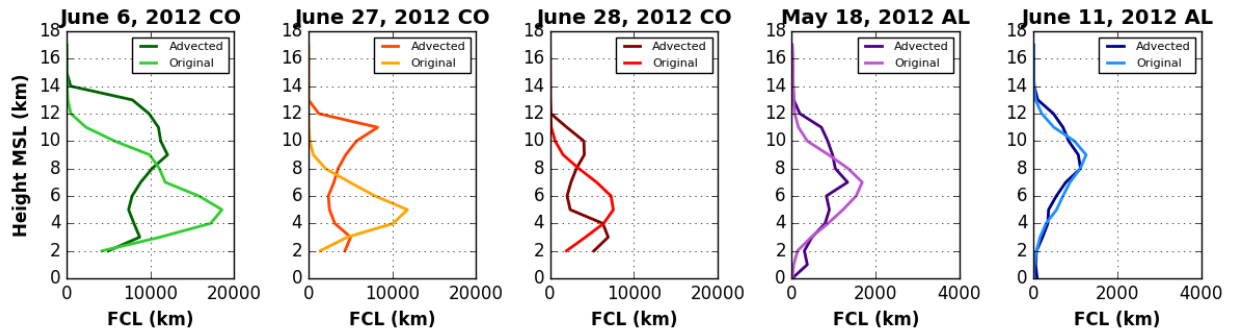


Figure 3.18: Vertical distribution profile of FCL integrated over all parcels before (“Original”) and after advection (“Advised”) for each storm. Created from the initial and final parcels locations with each parcel representing 1 km of FCL based on the 1 km resolution used in the trajectory analysis. Notice the stronger advection creating the bimodal shape in the “Advised” profile of the anomalous Colorado cases.

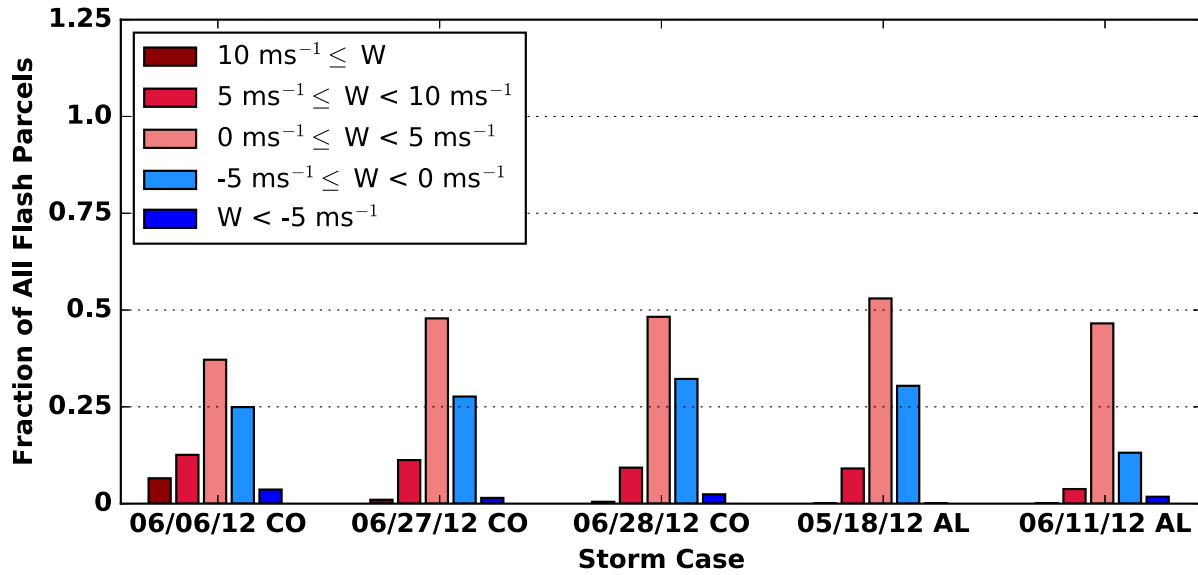


Figure 3.19: Fraction of total number of flash channel parcels initiating within various vertical wind velocity volumes for all five cases. Notice a higher fraction of parcels initiate in winds  $\geq 5.0 \text{ ms}^{-1}$  in the anomalous Colorado storms (right three cases). Also note, most parcels appear to initiate in weak vertical winds of  $\pm 5.0 \text{ ms}^{-1}$ .

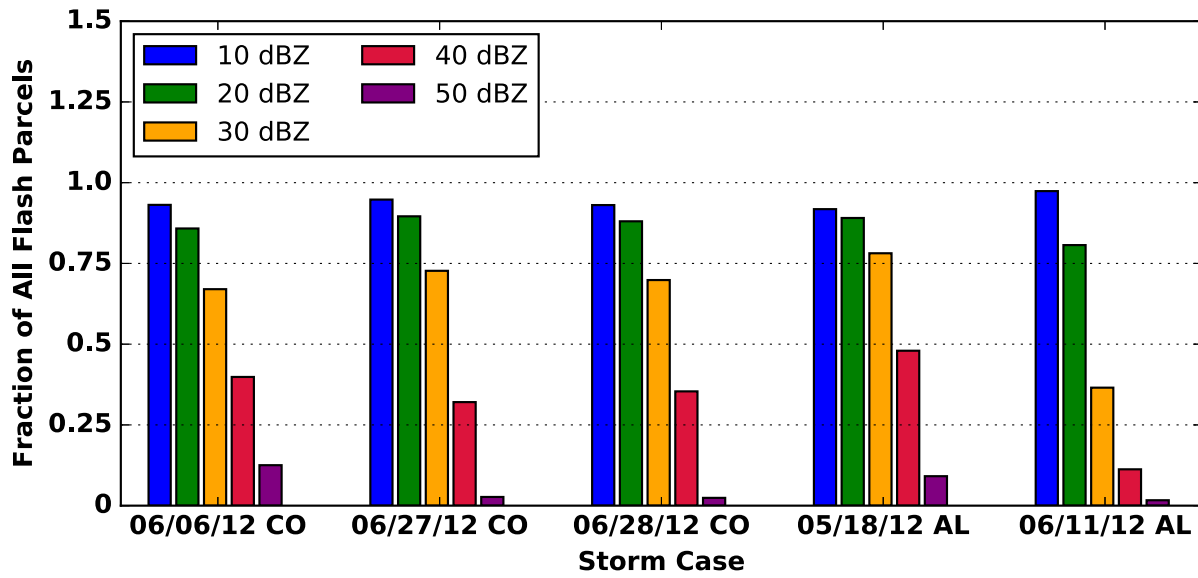


Figure 3.20: Fraction of total number of flash channel parcels initiating within reflectivity volume thresholds for all five cases. Notice fraction of parcels initiating within 20 dBZ (green) is comparable between all storms.

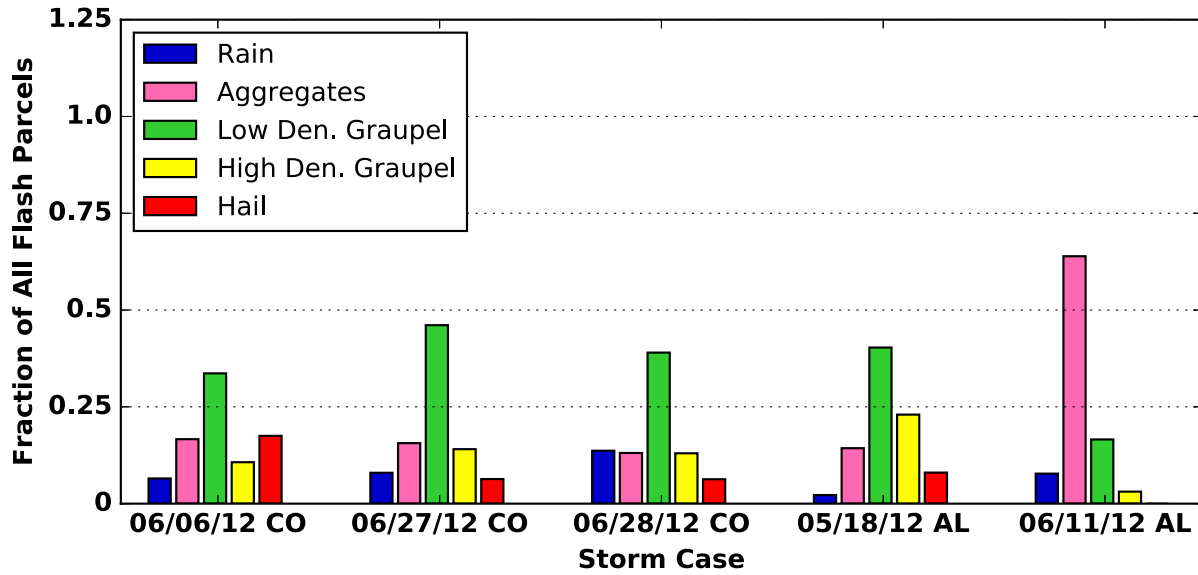


Figure 3.21: Fraction of total number of flash channel parcels initiating within various predominant hydrometeor volumes for all five cases. Notice a higher fraction of parcels initiate within volumes dominated by low density graupel but less channels within rain following non-inductive charging theory. Species listed are the top five volumes flash channel parcels most commonly initiate within, however flash channel parcels also initiate, though less frequently, within other dominant hydrometeor volumes.

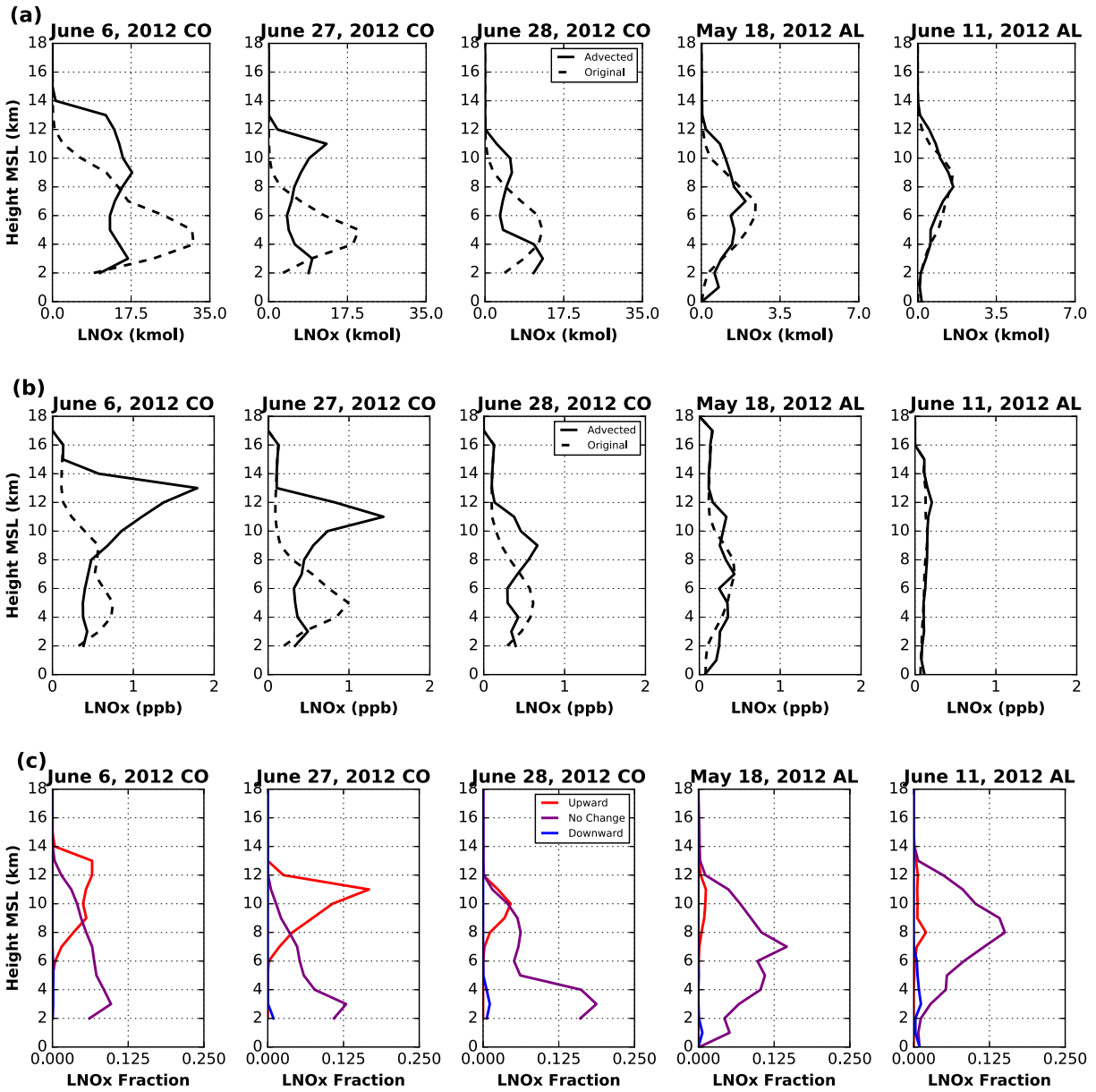


Figure 3.22: Vertical distribution of  $LNO_x$  for all thunderstorm cases in kilo moles (a) and parts per billion mixing ratios (b). Vertical profile of the  $LNO_x$  fraction at each level of the total  $LNO_x$  produced within each storm (c) categorized by contributions from parcels advecting  $\geq 2.0$  km (red), from parcels remaining within 2.0 km of initiation height (purple), and from parcels advecting downward  $\geq 2.0$  from initiation height (blue). Dashed lines represent values if flash channel parcels remained stationary at initiation locations without undergoing advection and solid lines represent values after flash channel parcels have been advected over storm lifetimes. Note that the x-axes' scales for May 18 and June 11 Alabama cases are one fifth that of Colorado storm cases in plot (a). Also, note that ground level is  $\sim 1.7$  km for the Colorado cases and  $\sim 0.2$  km for the Alabama cases.

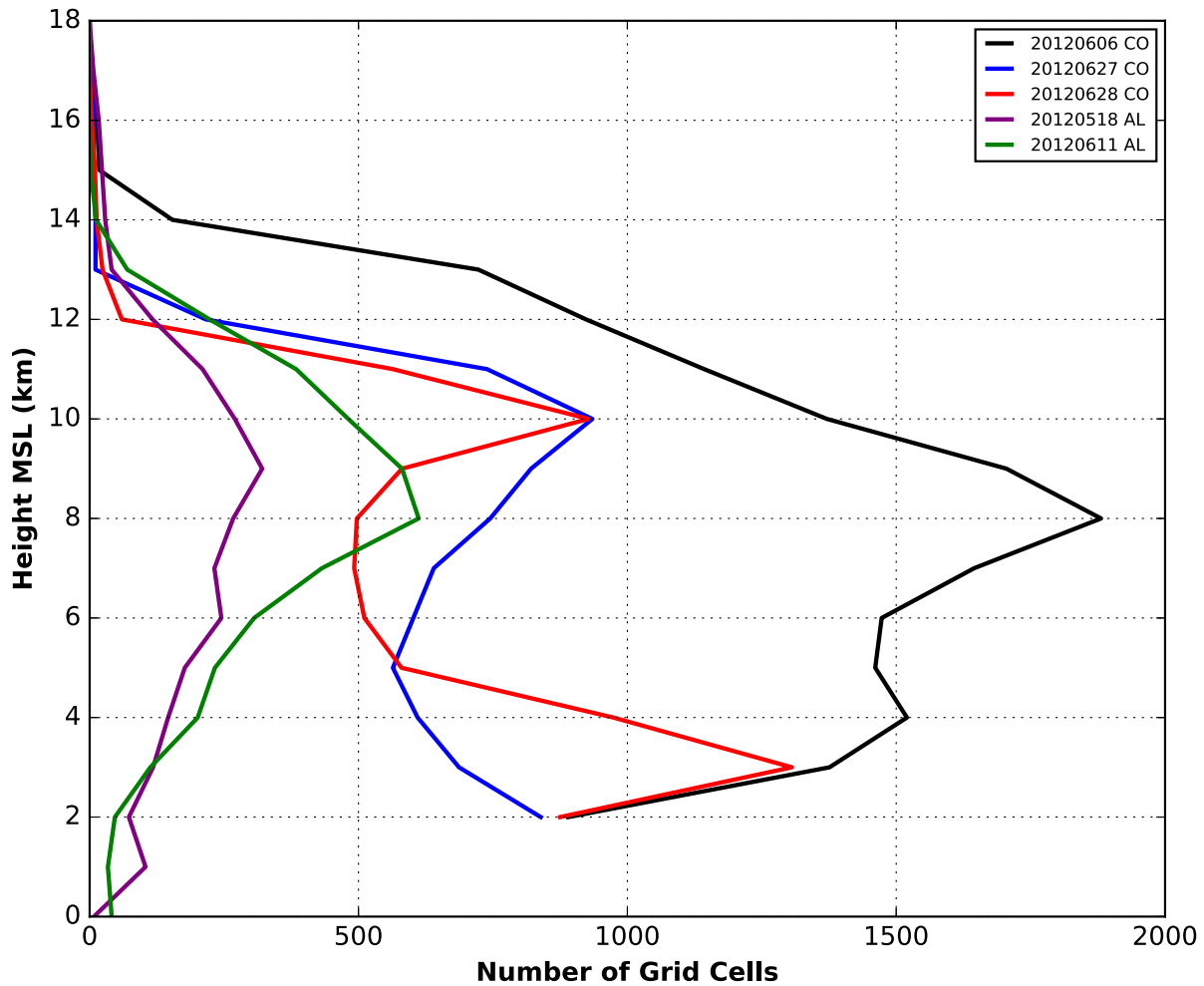


Figure 3.23: Vertical distribution of the number of grid cells containing flash channel parcels within the domain of each storm after all flash channel parcels have been advected in the trajectory analysis. These profiles represent the volume of environmental air that is used to calculate the mixing ratio values for each vertical level used in Fig. 3.22b. Each grid cell has a volume of  $1 \text{ km}^3$ . Note that ground level is  $\sim 1.7 \text{ km}$  in the Colorado cases versus  $\sim 0.2 \text{ km}$  in the Alabama cases.

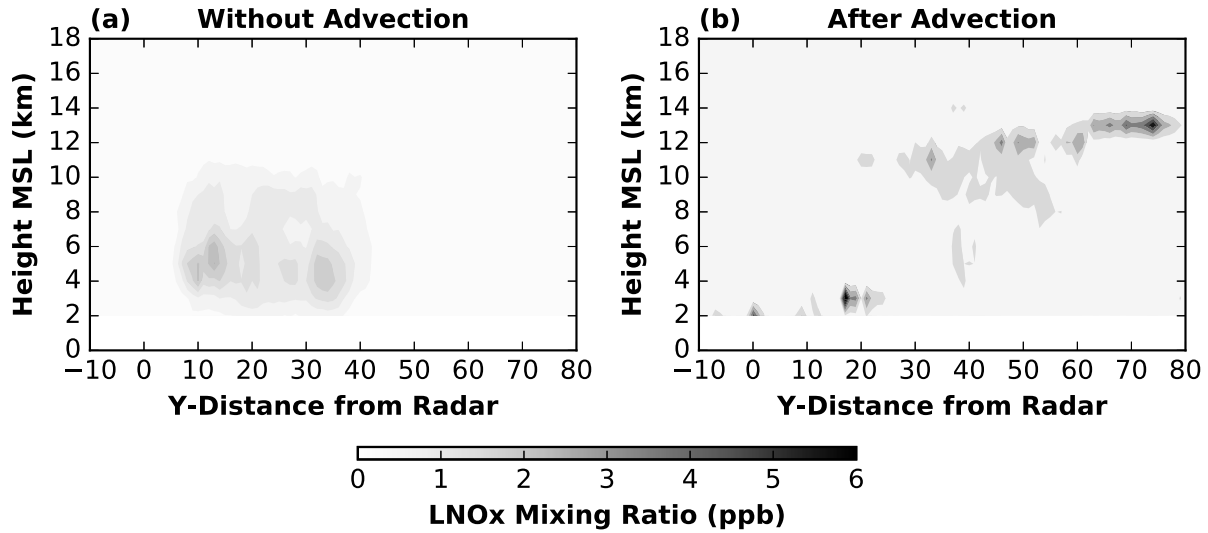


Figure 3.24: LNO<sub>x</sub> mixing ratios in parts per billion integrated along x-axes of June 6, 2012 Colorado storm. (a): values if flash channel parcels are kept at initiation locations and values after parcels advect throughout storm lifetimes (b). Note that ground level is ~1.7 km for this Colorado case.

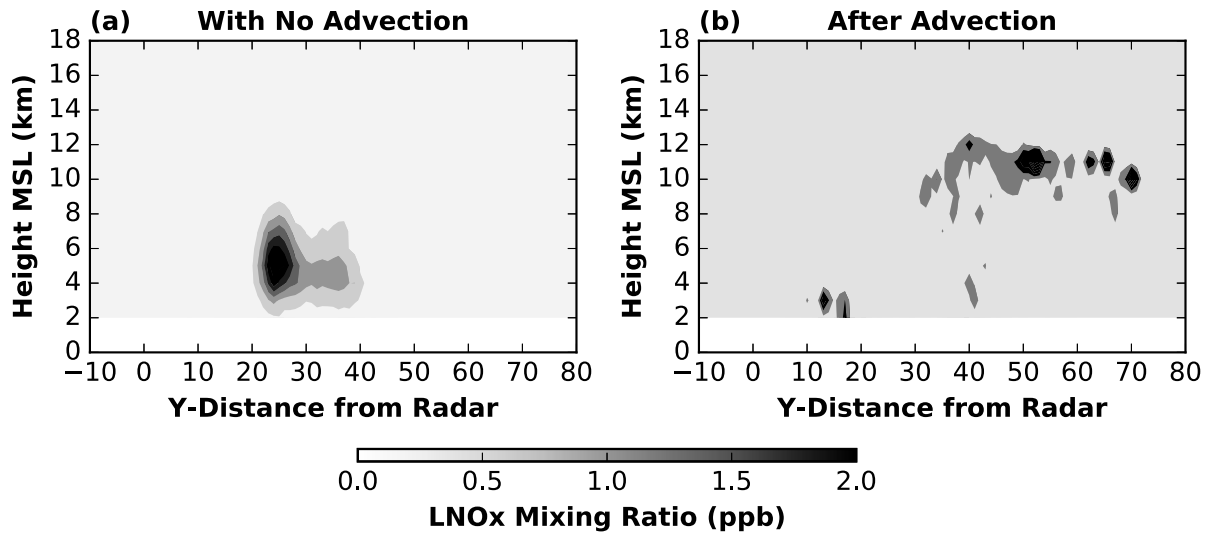


Figure 3.25: Same as Fig. 3.24 except for the June 27, 2012 Colorado case. Note that the color scale is one third that of the June 6, 2012 Colorado storm and that ground level is  $\sim 1.7$  km for this Colorado case.

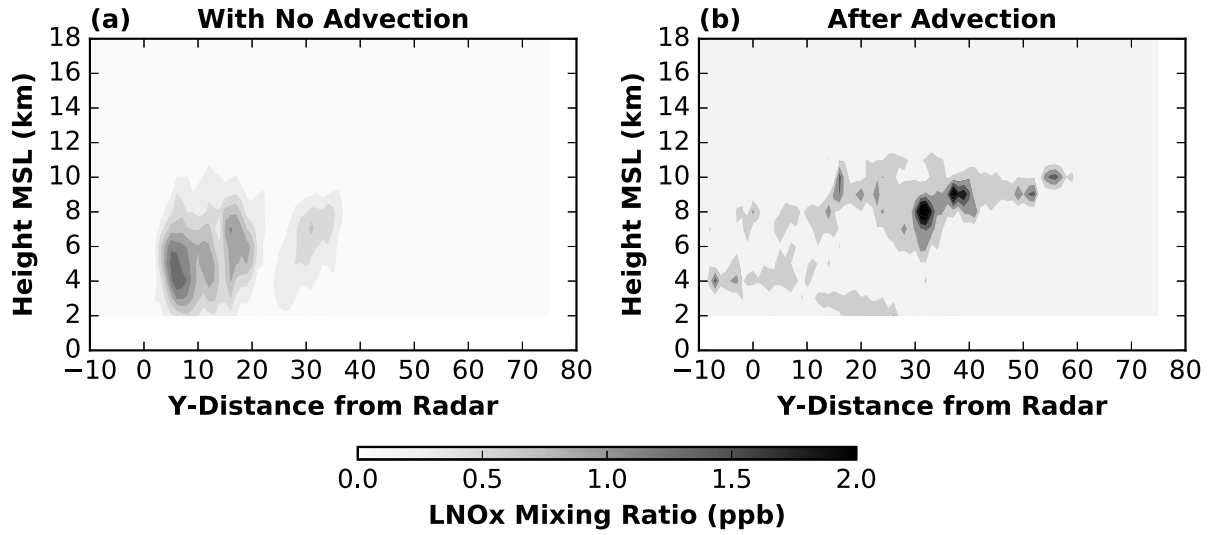


Figure 3.26: Same as Fig. 3.24 except for the June 28, 2012 Colorado case. Note that the color scale is one third that of the June 6, 2012 Colorado storm and that ground level is  $\sim 1.7$  km for this Colorado case.

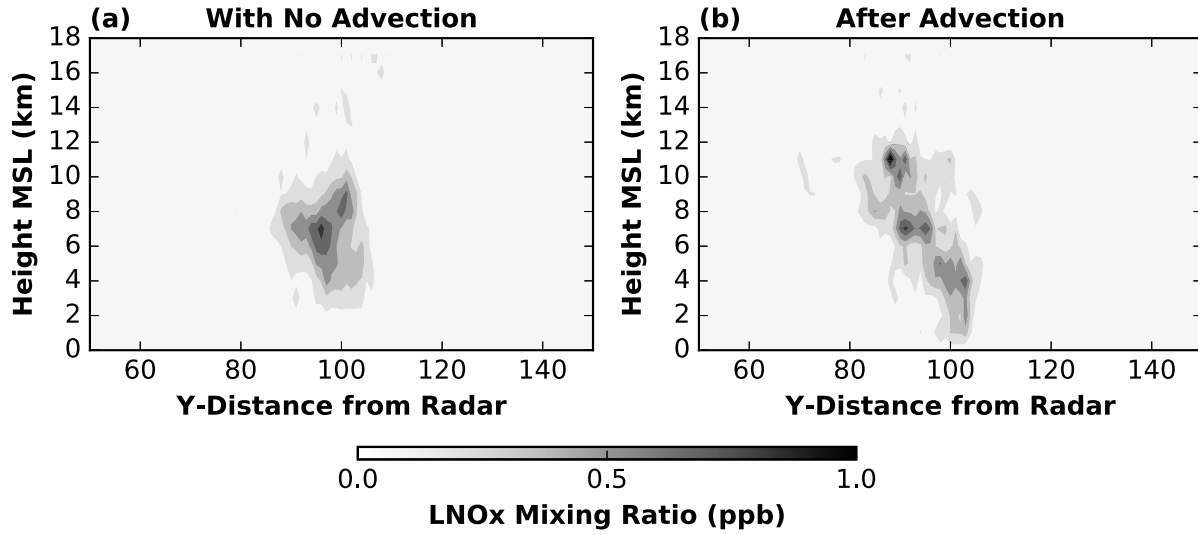


Figure 3.27: Same as Fig. 3.24 except for the May 18, 2012 Alabama case. Note that the color scale is one sixth that of the June 6, 2012 Colorado storm and that ground level is  $\sim 0.2$  km for this Alabama case.

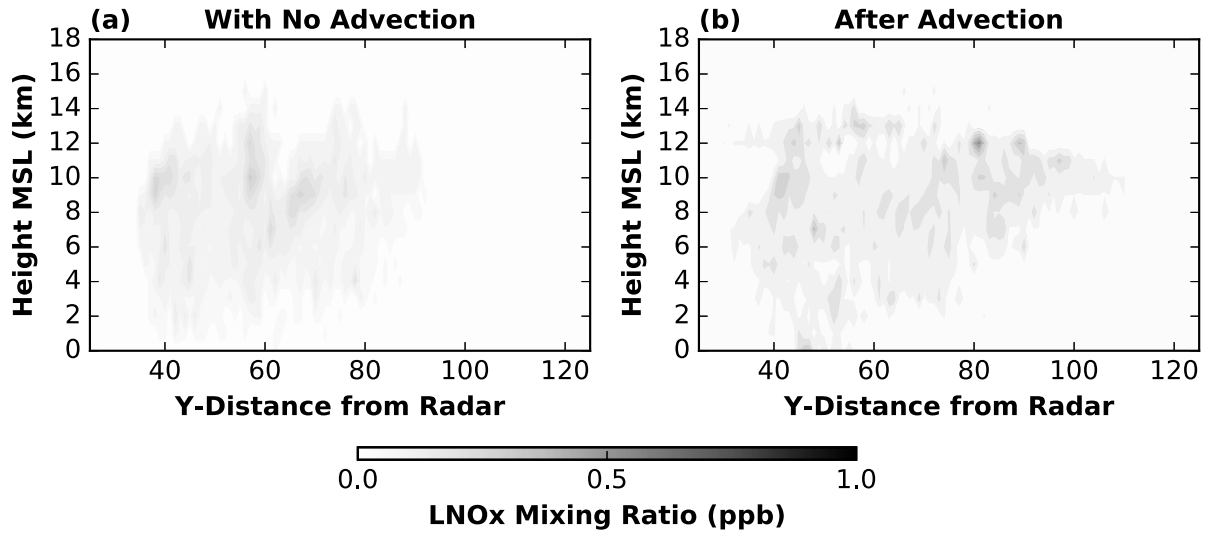


Figure 3.28: Same as Fig. 3.24 except for the June 11, 2012 Alabama case. Note that the color scale is one sixth that of the June 6, 2012 Colorado storm and that ground level is  $\sim 0.2$  km for this Alabama case.

Table 3.1: Various Measurements for Each Storm Event

	<u>Anomalous Polarity</u>				<u>Normal Polarity</u>		
	June 6, 2012 CO	June 27, 2012 CO	June 28, 2012 CO	Mean	May 18, 2012 AL	June 11, 2012 AL	Mean
<b>Timespan (UTC)</b>	2259 - 0017	2154 - 2254	2039 - 2159	N/A	2223 - 2256	2018 - 2122	N/A
<b>Total Flashes<sup>a</sup></b>	3737	723	680	1713	238	267	253
<b>Peak Flash Rate (fl. min<sup>-1</sup>)<sup>a,b</sup></b>	111	65	28	68	18	15	11
<b>Mean Initial FCL Height (MSL km)</b>	5.9	5.1	5.5	5.5	6.6	7.9	7.3
<b>Max 35 dBZ Height (MSL km)</b>	13.0	12.0	11.0	12.0	12.0	11.0	11.5
<b>Max 20 dBZ Volume (km<sup>3</sup>)<sup>c</sup></b>	3051	2125	1805	2327	2098	4000	3049
<b>Max Updraft (ms<sup>-1</sup>)<sup>c</sup></b>	38	17.6	15.1	23.6	9.1	11.3	10.2
<b>Max Downdraft (ms<sup>-1</sup>)<sup>c</sup></b>	17.9	10.1	11.3	13.1	6.4	16.6	11.5
<b>Approximate LCL (MSL km)<sup>d</sup></b>	3.8	3.5	4.2	3.8	1.0	0.7	0.9

<sup>a</sup>Flashes were attributed to each storm if they occurred within the storm identified cell or up to 10.0 km outside of the cell. <sup>b</sup>Flash rates were calculated every minute through respective storm lifetimes. <sup>c</sup>20 dBZ volume and maximum updrafts and downdrafts were calculated within each storm cell boundary extended upward along the z-axis. <sup>d</sup>Lifting condensation levels (LCLs) and boundary layer tops are estimated from University of Wyoming archived NWS soundings.

Table 3.2: LNO<sub>x</sub> Estimates for Each Storm Event

	<u>Anomalous Polarity</u>				<u>Normal Polarity</u>		
	June 6, 2012 CO	June 27, 2012 CO	June 28, 2012 CO	Mean	May 18, 2012 AL	June 11, 2012 AL	Mean
<b>Total Flash Channel Parcels</b>	108,406	43,803	38,738	190,947	8,881	6,737	7,809
<b>Approx. Boundary Layer Top (MSL km)<sup>a</sup></b>	3.6	4.8	4.8	4.4	2.5	0.8	1.7
<b>Single Flash LNO<sub>x</sub> Production Range (moles)<sup>b</sup></b>	2 – 1030	2 – 1449	5 - 1062	3-1180	2 - 638	3 - 269	3-454
<b>Mean LNO<sub>x</sub> per Flash (moles)<sup>b</sup></b>	72.4	158.0	142.8	124.4	92.5	60.7	76.6
<b>Total LNO<sub>x</sub> Produced (kmol)<sup>b</sup></b>	171.8	74.6	64.8	103.7	13.3	9.3	11.3
<b>LNO<sub>x</sub> from Parcels Advected Upward ≥ 2 km &amp; Ending &gt; 8 km<sup>b</sup></b>	63.1%	84.2%	39.8%	62.4%	11.5%	8.4%	10%
<b>LNO<sub>x</sub> from Parcels Ending Above Boundary Layer<sup>a,b</sup></b>	84.1%	56%	35.4%	58.5%	96.8%	99.9%	98.4%

<sup>a</sup>Boundary layer tops estimated from University of Wyoming archived NWS soundings. <sup>b</sup>LNO<sub>x</sub> production follows parameterization in Wang et al. (1998) using initial pressure of each parcel.

## CHAPTER 4 DISCUSSION

### 4.1. DC3 aircraft measurements

In situ observations of ambient  $\text{NO}_x$  concentrations and mixing ratios were measured during the DC3 field campaign. The NASA DC-8 normally measured concentrations in inflow areas while the National Science Foundation (NSF)/National Center for Atmospheric Research (NCAR) Gulfstream-V (G-V) aircraft measured outflow concentrations in the outer portions of 17 thunderstorm anvils. Occasionally the aircraft reversed their roles with the DC-8 penetrating thick anvil tops close to the deepest convection on a routine basis. Subtracting the inflow values from outflow  $\text{NO}_x$  values allows for the calculation of total  $\text{LNO}_x$  contributions. Unfortunately, measurements were not individually taken for these five storms though measurements were taken for other storms in both Colorado and Oklahoma during DC3. Stratospheric air was found to penetrate the tropopause in the June 6 storm, causing stratospheric ozone to mix into the storm anvil rendering  $\text{LNO}_x$  measurements less distinguishable. Additionally, transport was low due to weak environmental winds in the Alabama storms, causing weak transport of storm anvil outflow and increased likelihood of under-representative  $\text{LNO}_x$  concentrations (Pollack et al. 2016).

Observational analysis from Pollack et al. (2016) reveal similar  $\text{LNO}_x$  production per flash to those inferred from the current study which is based on channel length and includes detailed advection by storm updrafts and downdrafts, something that the Pollack et al. study did not include. The mean  $\text{LNO}_x$  production per flash in each storm in this study was approximately 72 moles (June 6), 158 moles (June 27), 143 moles (June 28), 92 (May 18), and 61 moles (June 11). In Pollack et al. (2016), production per flash based on all observed thunderstorms from the DC3 campaign was estimated to be 60 to 570 moles with larger uncertainty existing for larger

estimates from three Colorado storms (18 May, 12 June, and 22 June 2012). Additionally, Barthe and Barth (2008) found LNO<sub>x</sub> production to be  $\sim 121 \pm 41$  moles fl.<sup>-1</sup> for simulations of a STERAO storm characterized by high cloud base and high shear, like those in our Colorado sampled storms. However, Pollack et al. (2016) did not consider possible LNO<sub>x</sub> transport from convective downdrafts when computing these production estimates since outflow measurements were only recorded at one flight level.

#### 4.2. LNO<sub>x</sub> within the boundary layer

Pollack et al. (2016) note that previous studies (i.e. Chameides et al. 1987; Skamarock et al. 2003) found little evidence for LNO<sub>x</sub> entering the boundary layer and therefore follow similar assumptions. But this could still be an important LNO<sub>x</sub> transport pathway for some thunderstorms. One reason why such uncertainty regarding this transport pathway remains is that measuring in situ NO<sub>x</sub> specifically attributable to lightning at these lower heights would likely be difficult due to the shorter NO<sub>x</sub> lifetimes and aircraft safety concerns (Schumann and Huntrieser 2007).

Fortunately, results from this study provide further insight into this conundrum. Note that we get around the difficulty in measurements but still retain the in situ/real-time component by using LMA data to represent flash channels while introducing LNO<sub>x</sub> when and where it occurs into our thunderstorm case studies. Also note, this aspect separates this study from previous modeling studies that parameterize flash channel construction and LNO<sub>x</sub> production rather than utilizing actual observations. For example, Fig. 3.22a shows that an appreciable amount of LNO<sub>x</sub> exists in the lowest levels of the anomalous cases after parcels have undergone advection. In fact, further investigation shows that approximately 16% (June 6), 44% (June 27), 65% (June 28), 3.0% (May

18), and 0.1% (June 11) of the total LNO<sub>x</sub> produced from each thunderstorm lies in the boundary layer (as estimated from soundings listed in Appendix A; boundary layer heights listed in Table 3.2) after advection of flash channel parcels has occurred. Contrary to previous assumptions, this is an appreciable fraction of the total LNO<sub>x</sub> for the anomalous thunderstorm cases, especially for the June 27 and 28 storms. Future work is required to explicitly state that anomalous storms produce an appreciable fraction of their total LNO<sub>x</sub> within the boundary layer, though the lower mode in flash channel initiation in our anomalous storms similar to that in Fuchs (2017) suggests these three cases represent anomalous storm structure.

Figure 3.22c shows clear peaks in the purple curves for each of these three cases, meaning that flash channel parcels that remained relatively stationary (within 2 km of initial heights) contribute to most of the LNO<sub>x</sub> that does exist within the boundary layer. For clarification, these curves show the fraction of total LNO<sub>x</sub> for each particular storm that is contributed to by parcels remaining within 2 km of their initial heights. Therefore, according to these trajectory analyses, nearly all the LNO<sub>x</sub> at the lowest levels of these storms results from parcels that remain close to their initial heights. This also appears to be the case for the two normal polarity Alabama cases, though less LNO<sub>x</sub> appears to reside in lower levels of these storms. Examining the positioning of updrafts in the anomalous storms in Figs. 3.5d, 3.6d, and 3.7d show that maximum updrafts occur within cloud level and above the lifting condensation level (LCL) for each of these storms (see Table 3.1 for LCLs). Since most flash channel parcels are created just above these LCLs and below the base of these updraft cores (FCL modes ~5.5 km), parcels are on the brink of undergoing strong upward transport by intense updrafts or remaining in areas of weak to moderate vertical motion and remaining more stationary. Figure 3.8 shows how an appreciable fraction of parcels appear to originate in the lowest two vertical levels of these three anomalous

storms, yet very few parcels originate in intense updrafts  $> 5 \text{ ms}^{-1}$ . This is also seen in the left-hand plot in Fig. 3.11 where fewer parcels appear to initiate within stronger vertical wind speeds at the lowest levels of the June 6 storm. The overall lower mode in flash channel (parcel) initiation within these three anomalous Colorado thunderstorms appears to position a large fraction parcels directly beneath the strongest updraft cores. Since most parcels also appear to form on the periphery of updraft cores as previously discussed, not all flash channel parcels have the opportunity to enter the strongest updraft cores. Thus, flash channel parcels either remain in the lowest 2 km (providing a source of  $\text{NO}_x$  to remain in the boundary layer) of the storm or undergo strong upward advection to heights above 8 km, working to create the distinct bimodal final distribution of flash channel parcels (length) seen in Fig. 3.18. Table 3.2 lists these values for reference.

#### 4.3 Justification discussion

Figure 3.2 suggest that flashes tended to be shorter during high flash rate periods of the storms in this study, likely explaining why our estimates compare well with Pollack et al. (2016). For example, when the total  $\text{LNO}_x$  production is divided into the number of flashes for each storm, as is done in the Pollack et al. study, it is inherently assumed that flash length is the same among all flashes when, in fact, we have demonstrated that FCL and  $\text{LNO}_x$  production are highly variable (see Table 3.2 for  $\text{LNO}_x$  per flash ranges for each storm). The preponderance of shorter flashes at times would inherently produce less  $\text{LNO}_x$ , but if some transport to the boundary layer occurs (not accounted for in Pollack et al. 2016), averaging over all flashes could produce similar results. In other words, the  $\text{LNO}_x$  that is transported to or that forms from flashes within the boundary layer limits the total potential  $\text{LNO}_x$  to be measured by aircraft at higher levels, just as

shorter flashes producing less LNO<sub>x</sub> does in the first place. Therefore, not taking aircraft measurements of LNO<sub>x</sub> in the boundary layer could be accounted for by the variance in flash size/length when total production is averaged over all flashes. These results increase confidence in LNO<sub>x</sub> production on a flash by flash basis though this artifact supports the need for further investigation into the LNO<sub>x</sub> production per flash using channel length for different regions of the world.

## CHAPTER 5 CONCLUSIONS

### 5.1. Summary

In this study, over 5000 flashes with a total of over 206,500 km of channel length observed from VHF Colorado and Northern Alabama LMA networks are divided into 1.0 km flash channel parcels for five thunderstorm cases during the DC3 field campaign. Parcels are then advected within each storm at 50 second time steps following the 3-D wind fields derived from dual-Doppler analysis. The mean of flash channel initiation height was found to be lower in the anomalous polarity Colorado storms (~5.5 km) than in the normal polarity Alabama storms (~7.5 km), which agrees with climatology discussed by Fuchs (2017). Updrafts also tended to be broader and more intense in these storms, especially the June 6, 2012 storm where values approached  $40 \text{ ms}^{-1}$  at times, with larger updraft volumes (over  $5 \text{ ms}^{-1}$ ) throughout their lifetimes. Even though flash channels tended to initiate at lower levels, the enhanced updrafts were found to efficiently advect flash channel parcels to higher altitudes in the anomalous thunderstorms. Moreover, a larger fraction (~70%) of parcels in the mid-levels (4-9 km) of these storms tended to advect upward by more than 2.0 km compared to the normal polarity cases (~35%), resulting in few parcels remaining near their initiation heights in the mid-levels of these anomalous storms.

The more efficient transport of flash channel parcels in the anomalous storms causes a more distinct bimodal distribution in the final  $\text{LNO}_x$  mixing ratios with appreciable transport to the upper troposphere while some parcels are not advected upward and remain near or within the boundary layer. The larger number of flashes (and channel length) in the anomalous storms in conjunction with this more efficient transport ultimately leads to higher amounts of  $\text{LNO}_x$

residing in the upper troposphere, where longer lifetimes exist. This suggests that on average, anomalous polarity thunderstorms have a more substantial impact on potential tropospheric ozone production than normal polarity thunderstorms. It is important to note that the environmental conditions such as elevated CAPE, reduced warm cloud depth, storm updraft width, shear, etc. play an important role in the developing charge structure that defines the storm polarity in the first place, thus it is not solely the distribution of charge and polarity that cause these differences in LNO<sub>x</sub> production and transport. For example, increased updraft strength and width are thought to play important roles in increasing the super-cooled liquid water content into storms that form in high CAPE and high cloud base environments, which then likely plays an important role in forming the charge structure of anomalous thunderstorms as was discussed in Section 1.2.2 (Saunders and Peck 1998; Williams et al. 2005; Bruning et al. 2014; Fuchs 2017). Studies of more thunderstorm cases should be completed in the future to further solidify this argument and develop more robust statistical significance for these statements.

## 5.2. Normal versus anomalous polarity

Once converted from FCL to LNO<sub>x</sub> following the parameterization from DeCaria et al. (2000) and Wang et al. (1998), enhanced concentrations and mixing ratios above 8 km in the anomalous polarity thunderstorms were found, though elevated values above this level occur in all five cases. For example, peak LNO<sub>x</sub> mixing ratios above 8 km were nearly two to three times as large in the June 6 and June 27 cases compared to the other three cases. More of these parcels were found to originate in updrafts of the three anomalous polarity cases resulting in nearly 25% of all parcels originating below 8 km to advect to above 8 km (from the lower to upper troposphere). However, relatively few parcels originated above 8 km in these storms. Thus,

nearly half of all flash channel parcels ended up above 8 km at the end of each storm's lifetime for these three cases. On the other hand, a greater proportion of flash channel parcels originated above 8 km in the normal polarity Alabama cases, with fewer parcels advecting from below to above this level as occurs in the anomalous Colorado cases. Results between both storm structures reveal that nearly half of parcels end up above 8 km at the end of each storm's lifetime. Therefore, the processes leading to similar upper tropospheric LNO<sub>x</sub> fractions can be divided into two processes – (1) advection-driven distribution in the anomalous polarity storms, and (2) location-driven distribution in the normal polarity thunderstorms. Since significantly more flashes (and larger channel length) tend to occur in storms of anomalous polarity like the June 6 storm, more total LNO<sub>x</sub> is created for these storms. This leads to overall higher mixing ratios of LNO<sub>x</sub> in the upper troposphere downwind of and following these storms. Since the lifetime of NO<sub>x</sub> is longer at these levels, increased LNO<sub>x</sub>-induced ozone production is likely to take place in the residual anvil air in the following days. These results suggest that storms of anomalous polarity have a larger impact in upper tropospheric LNO<sub>x</sub> and potential downstream ozone production, though examining more cases in future work must be done to substantiate this conclusion.

Results from this study compare well in some areas to those of previous studies. For example, appreciable LNO<sub>x</sub> appears to remain in the lower troposphere/boundary layers in the anomalous Colorado storms as a result of the lower mode in the initiation of flash channels by height. While this contradicts findings of previous studies, it is somewhat in agreement with the emission profile suggested by Pickering et al. (1998) who includes a strong upper-level LNO<sub>x</sub> peak along with a peak in the boundary layer, though the peak in the boundary layer of the three anomalous storms does not necessarily reside directly at the surface (~1.7 km; see Fig. 3.22).

The resulting vertical profiles in LNO<sub>x</sub> in the anomalous polarity storms also appear to best match that of modeled mid-latitude storms in a study by Ott et al. (2010), while the normal polarity storms appear to best match that of modeled subtropical storms. LNO<sub>x</sub> production per flash compare well to observations listed in Pollack et al. (2016) and Barthe and Barth (2008). These results are for five storms only, so future investigation of more storms will help solidify these findings and develop more robust statistical evidence for the differences in LNO<sub>x</sub> production in anomalous versus normal polarity storms.

### 5.3 Flash channel parcel originations

As previously noted, DeCaria et al. (2005) note that MacGorman and Rust (1998) found most flash channels occur within the 20 dBZ reflectivity volume of storms. They make use of this to limit the horizontal distribution of flash channels following a pre-defined vertical profile. This method appears to be accurate with approximately 80% of all flash channel parcels in this study initiating in reflectivity values of at least 20 dBZ. However, it may also be beneficial to scale flash channel introduction to areas of weaker vertical motion ( $|w| \leq 5 \text{ ms}^{-1}$ ) since nearly 75% of flash channel parcels in each case of this study initiate within these regions surrounding stronger reflectivity and updraft cores. Scaling flash channel distribution to areas of low and high density graupel may also benefit modelers since most flash parcels originate in these regions for this study, though various models may produce ice mass differently depending on the microphysics scheme used. Also, identification of hydrometeors from radar-retrieved fields is an imperfect process with inherent limitations and, naturally, not all hydrometeors within a given volume are not uniquely the exact identified specie. Correctly placing LNO<sub>x</sub> in the vertical according to profiles representative to storms of the same region must also occur, otherwise unrealistic

convective transport may occur. If flash channels are scaled to these storm volumes, redistribution by storm winds will likely better resemble realistic storm patterns. Future work should examine the effect of such changes to LNO<sub>x</sub> parameterizations to analyze their potential benefit.

#### 5.4. Closing statements

For this study, numerous flash channels were divided into 1.0 km flash length parcels and the convective transport of NO<sub>x</sub> generated by flash channels was studied in detail for five thunderstorms representing typical polarity structures commonly found in Colorado and Alabama. These results provide better understanding into the different contributions and impact of normal and anomalous polarity thunderstorms to upper tropospheric NO<sub>x</sub> production. Total FCL and LNO<sub>x</sub> production appear to vary widely between flashes within individual thunderstorms, which also vary in total flash production depending on environmental conditions (that are regionally dependent). Investigation of flash channel occurrence in the storms of this study show current distribution methods and parameterizations to be reasonable, however possible modifications can be made. Results suggest possible modifications could include scaling roughly 75% of the LNO<sub>x</sub> inserted within the 20 dBZ volume to areas of weaker vertical motion and hail, high density graupel, and low density graupel HID regions. These improvements in LNO<sub>x</sub> parameterizations in chemical transport and global climate modeling for storms in the Southeast and High Plains regions of the United States. In the end, upper tropospheric ozone production appears to be highly dependent upon not only the number of flashes and channel length that produce LNO<sub>x</sub> but also where this LNO<sub>x</sub> is transported once it is created, all of which is fundamentally affected by thunderstorm charge structures and cloud dynamics. Utilizing

appropriate FCL vertical distributions is necessary to correctly model storms of a particular environment. The variance found in this study highlights the need to further investigate thunderstorm total flash and channel length production in a wide variety of storm types and respective locations. Future work focusing on storms in other regions of the world will only enlighten our understanding of the variance in lightning activity and LNO<sub>x</sub> production by region. Natural lightning NO<sub>x</sub> production will be better parameterized when combined with results for this study for the two regions of the U.S., and hopefully with future research to come.

## REFERENCES

- Barthe, C., and M. C. Barth, 2008: Evaluation of a new lightning-produced NO<sub>x</sub> parameterization for cloud resolving models and its associated uncertainties. *Atmos. Chem. Phys.*, **8**, 4691–4710.
- Barth, M. C., and coauthors, 2015: The Deep Convective Clouds and Chemistry (DC3) Field Campaign. *Bull. Amer. Meteor. Soc.*, **96**, 1281–1309.
- Basarab, B. M., S. A. Rutledge, and B. R. Fuchs, 2015: An improved lightning flash rate parameterization developed from Colorado DC3 thunderstorm data for use in cloud-resolving chemical transport models. *Journal of Geophysical Research: Atmospheres*, **120 (18)**, 9481–9499.
- Bruning, E. C. and D. R. MacGorman, 2013: Theory and observations of controls on lightning flash rate spectra. *J. Atmos. Sci.*, **70**, 4012–4029.
- Bruning, E. C., 2013: Streamed clustering of lightning mapping data in Python using sklearn. *Scientific Computing With Python*, Vol. 2.
- Bruning, E., S. A. Weiss, and K. M. Calhoun, 2014: Continuous variability in thunderstorm primary electrification and an evaluation of inverted-polarity terminology. *Atmos. Res.*, **135**, 274–284.
- Carey, L. D., M. J. Murphy, T. L. McCormick, and N. W. Demetriades, 2005: Lightning location relative to storm structure in a leading-line trailing stratiform mesoscale convective system. *J. Geophys. Res.*, **110**, D03105.
- Chameides, W. L., D. D. Davis, J. Bradshaw, M. Rodgers, S. Sandholm, and D. B. Bai, 1987: An estimate of the NO<sub>x</sub> production-rate in electrified clouds based on NO observations from the GTE/CITE-1 fall 1983 field operation. *J. Geophys. Res.*, **92**, 2153–2156.
- DeCaria, A. J., K. E. Pickering, G. L. Stenchikov, and L. E. Ott, 2005: Lightning-generated NO<sub>x</sub> and its impact on tropospheric ozone production: A three-dimensional modeling study of a Stratosphere-Troposphere Experiment: Radiation, Aerosols and Ozone (STERAO-A) thunderstorm. *Journal of Geophysical Research: Atmospheres*, **110 (D14)**.
- DeCaria, A. J., K. E. Pickering, G. L. Stenchikov, J. R. Scala, J. L. Stith, J. E. Dye, B. A. Ridley, and P. Laroche, 2000: A cloud-scale model study of lightning-generated NO<sub>x</sub> in an individual thunderstorm during STERAO-A. *Journal of Geophysical Research*, **105**, 11.
- Dolan, B., S. A. Rutledge, S. Lim, V. Chandrasekar, and M. Thurai, 2013: A robust C-band hydrometeor identification algorithm and application to a long-term polarimetric radar dataset. *Journal of Applied Meteorology and Climatology*, **52 (9)**, 2162–2186.

- Dye, J.E., et al., 2000: An overview of the Stratospheric-Tropospheric Experiment: Radiation, Aerosols, and Ozone (STERAO)-Deep Convection experiment with results for the July 10, 1996 storm. *J. Geophys. Res.*, **105 (D8)**, 10 023-10 045.
- Dye, J. E., J. J. Jones, W. P. Winn, T. A. Cerni, B. Gardiner, D. Lamb, R. L. Pitter, J. Hallett, and C. P. R. Saunders, 1986: Early electrification and precipitation development in a small, isolated Montana cumulonimbus. *J. Geophys. Res.*, **91 (D1)**, 1231–1247.
- Fuchs, B. R., E. C. Bruning, S. A. Rutledge, L. D. Carey, P. R. Krehbiel, and W. Rison, 2016: Climatological analyses of LMA data with an open-source lightning flash-clustering algorithm. *Journal of Geophysical Research: Atmospheres*, **121 (14)**, 8625- 8648.
- Fuchs, B. R., S. A. Rutledge, E. C. Bruning, J. R. Pierce, J. K. Kodros, T. J. Lang, D. R. MacGorman, P. R. Krehbiel, and W. Rison, 2015: Environmental controls on storm intensity and charge structure in multiple regions of the continental United States. *Journal of Geophysical Research: Atmospheres*, **120 (13)**, 6575-6596.
- Fuchs, B. R., 2017: Microphysical, dynamical, and lightning processes associated with anomalous charge structures in isolated convection. *Ph.D. Dissertation, Colorado State University*.
- Fuchs, B. R., 2014: Factors affecting lightning behavior in various regions of the United States. *Master's Thesis, Colorado State University*.
- Huntrieser, H., and coauthors, 2016: Injection of lightning-produced NO<sub>x</sub>, water vapor, wildfire emissions, and stratospheric air to the UT/LS as observed from DC3 measurements. *Journal of Geophysical Research: Atmospheres*, **121**, 6638–6668.
- Jayarathne, E. R., C. P. R. Saunders, and J. Hallett, 1983: Laboratory studies of the charging of soft-hail during ice crystal interactions. *Q. Jour. of the Roy. Met. Soc.*, **109**, 609-630.
- Kaser, L., E. G. Patton, G. G. Pfister, A. J. Weinheimer, D. D. Montzka, F. Flocke, A. M. Thompson, R. M. Stauffer, and H. S. Halliday, 2017: The effect of entrainment through atmospheric boundary layer growth on observed and modeled surface ozone in the Colorado Front Range. *Journal of Geophysical Research: Atmospheres*, **122**, 6075–6093.
- Krehbiel, P., R. J. Thomas, W. Rison, T. Hamlin, M. Davis, and J. Harlin, 2000: Lightning mapping observations in central Oklahoma. *Eos*, **81 (3)**, 21-25.
- Kuhlman, K. M., D. R. MacGorman, M. I. Biggerstaff, and P. R. Krehbiel, 2009: Lightning initiation in the anvils of two supercell storms. *Geophys. Res. Lett.*, **36**, L07802.
- Lang, T. J., and S. A. Rutledge, 2011: A framework for the statistical analysis of large radar and lightning datasets: Results from STEPS 2000. *Mon. Wea. Rev.*, **139**, 2536-2551.

- Lawrence, M. G., W. L. Chameides, P. S. Kasibhatla, H. Levy II, and W. Moxim, 1995: Lightning and Atmospheric Chemistry: The Rate of Atmospheric NO Production. vol. I, pp. 189–202, CRC Press, Boca Raton, Fla.
- Leighton, P. A., 1961: Photochemistry of Air Pollution. 300 pp., Elsevier, New York.
- MacGorman, D. R., and W. D. Rust, 1998: The Electrical Nature of Storms, 422 pp., Oxford Univ. Press, New York.
- Maggio, C., L. Coleman, T. Marshall, M. Stolzenburg, M. Stanley, T. Hamlin, P. Krehbiel, W. Rison, and R. Thomas, 2005: Lightning-initiation locations as a remote sensing tool of large thunderstorm electric field vectors. *Journal of Atmospheric and Oceanic Technology*, **22** (7), 1059-1068.
- Nault, B. A., J. L. Laughner, P. J. Wooldridge, J. D. Crouse, J. Dibb, G. Diskin, J. Peischl, J. R. Podolske, I. B. Pollack, T. B. Ryerson, E. Scheuer, P. O. Wennberg, and R. C. Cohen, 2017: Lightning NO<sub>x</sub> emissions: reconciling measured and modeled estimates with updated NO<sub>x</sub> chemistry. *Geophysical Research Letters*, **44**, 9479–9488.
- Nelson, S. P., and R. A. Brown, 1987: Error sources and accuracy of vertical velocities computed from multiple-Doppler radar measurements in deep convective storms. *J. Atmos. Oceanic Technol.*, **4**, 233–238.
- Ott, L. E., K. E. Pickering, G. L. Stenchikov, D. J. Allen, A. J. DeCaria, B. Ridley, R.-F. Lin, S. Lang, and W.-K. Tao, 2010: Production of lightning NO<sub>x</sub> and its vertical distribution calculated from three-dimensional cloud-scale chemical transport model simulations. *J. Geophys. Res.*, **115**, D04301.
- Pickering, K. E., Y. Wang, W.-K. Tao, C. Price, and J.-F. Muller, 1998: Vertical distributions of lightning NO<sub>x</sub> for use in regional and global chemical transport models. *Journal of Geophysics Research: Atmospheres (1984-2012)*, **103** (D23), 31 203–31 216.
- Pollack, I. B., C. R. Homeyer, T. B. Ryerson, K. C. Aikin, J. Peischl, E. C. Apel, T. Campos, F. Flocke, R. S. Hornbrook, D. J. Knapp, et al., 2016: Airborne quantification of upper tropospheric NO<sub>x</sub> production from lightning in deep convective storms over the United States Great Plains. *Journal of Geophysics Research: Atmospheres*, **121**, 2002–2028.
- Price, C., J. Penner, and M. Prather, 1997: NO<sub>x</sub> from lightning: 1. Global distribution based on lightning physics. *Journal of Geophysical Research: Atmospheres*, **102** (D5), 5929-5941.
- Ridley, B. A., J. E. Dye, J. G. Walega, J. Zheng, F. E. Grahek, and W. Rison, 1996: On the production of active nitrogen by thunderstorms over New Mexico. *J. Geophys. Res.*, **101** (D15), 20 985–21 005.

- Rison, W., R. Thomas, P. Krehbiel, T. Hamlin, and J. Harlin, 1999: A GPS-based three-dimensional lightning mapping system: Initial observations in central New Mexico. *Geophys. Res. Lett.*, **26**, 3573-3576.
- Saunders, C. P. R., and S. L. Peck, 1998: Laboratory studies of the influence of the rime accretion rate on charge transfer during crystal/graupel collisions. *J. Geophys. Res.*, **103 (D12)**, 13 949–13 956.
- Saunders, C. P. R., W. D. Keith, and R. P. Mitzeva, 1991: The effect of liquid water on thunderstorm charging. *J. Geophys. Res.*, **96**, 11 007-11 017.
- Schumann, U., and H. Huntrieser, 2007: The global lightning-induced nitrogen oxides source. *Atmospheric Chemistry and Physics*, **7 (14)**, 3823-3907.
- Skamarock, W. C., J. E. Dye, E. Defer, M. C. Barth, J. L. Stith, B. A. Ridley, and K. Baumann, 2003: Observational- and modeling-based budget of lightning-produced NO<sub>x</sub> in a continental thunderstorm. *J. Geophys. Res.*, **108 (D10)**, 4305.
- Takahashi, H., K. Suzuki, and G. Stephens, 2017: Land-ocean differences in the warm-rain formation process in satellite and ground-based observations and model simulations. *Quarterly Journal of the Royal Meteorological Society*, **143 (705)**, 1804-1815.
- Takahashi, T., 1978: Riming electrification as a charge generation mechanism in thunderstorms. *Atmos. Sci.*, **35**, 1536-1548.
- Wacker, R. S., and R. E. Orville, 1999: Changes in measured lightning flash count and return stroke peak current after the 1994 U.S. National Lightning Detection Network upgrade: 1. Observations. *J. Geophys. Res.*, **104 (D2)**, 2151–2157.
- Wang, Y., A. W. DeSilva, G. C. Goldenbaum, and R. R. Dickerson, 1998: Nitric oxide production by simulated lightning: Dependence on current, energy and pressure. *J. Geophys. Res.*, **103**, 19 149–19 159.
- Weiss, S. A., D. R. MacGorman, and K. M. Calhoun, 2012: Lightning in the anvils of supercell thunderstorms. *Mon. Weather Rev.*, **140**, 2064-2079.
- Williams, E. R., V. Mushtak, D. Rosenfeld, S. Goodman, and D. Boccippio, 2005: Thermodynamic conditions favorable to superlative thunderstorm updraft, mixed phase microphysics and lightning flash rate. *Atmos. Res.*, **76**, 288–306.
- Williams, E. R., 2006: Problems in lightning physics: The role of polarity asymmetry. *Plasma Sources Science and Technology*, **15 (2)**, S91.
- Williams, E. R., 1989: The tripole structure of thunderstorms. *J. Geophys. Res.*, **94**, 13 151-13 167.

- Williams, E. R., 1985: Large-scale separation in thunderclouds. *J. Geophys. Res.*, **90**, 6013-6025.
- Workman, E. J., and S. E. Reynolds, 1950: Electrical phenomena occurring during the freezing of dilute aqueous solutions and their possible relationship to thunderstorm electricity. *Phys. Rev.*, **78**, 254-259.
- Wu, S., L. J. Mickley, D. J. Jacob, J. A. Logan, R. M. Yantosca, and D. Rind, 2007: Why are there large differences between models in global budgets of tropospheric ozone?. *J. Geophys. Res.*, **112**, D05302.

APPENDIX A

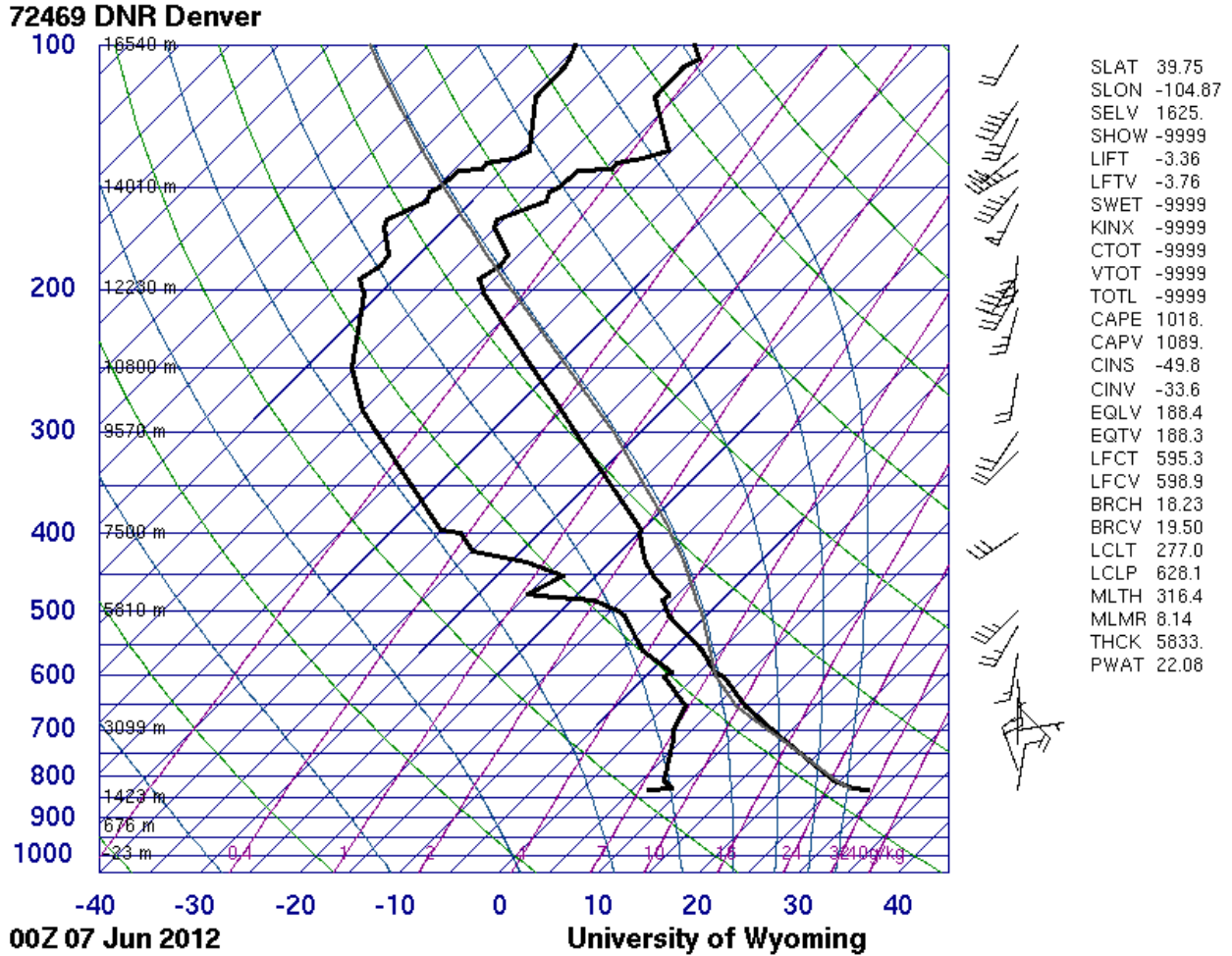


Figure A.1: 0000 UTC June 7, 2012 KDNR sounding SKEW-T for the June 6, 2012 storm event from the University of Wyoming sounding archive website (<http://weather.uwyo.edu/upperair/sounding.html>). The x-axis corresponds to temperature (in °C) (angled blue lines with positive slope) and y-axis corresponds to pressure (in hPa) (horizontal blue lines) decreasing with height. Left-most solid black curve represents the dew point temperature with pressure/height and right-most black curve represents the actual air temperature with pressure/height. Horizontal winds are plotted with height on the right-hand side. All other lines and curves are irrelevant for this study. Pressure and horizontal winds were interpolated onto the 1 km vertical grid for the flash channel parcel trajectory analysis and LNO<sub>x</sub> production. Boundary layer height was estimated to be ~650 hPa (~3.6 km).

**72469 DNR Denver**

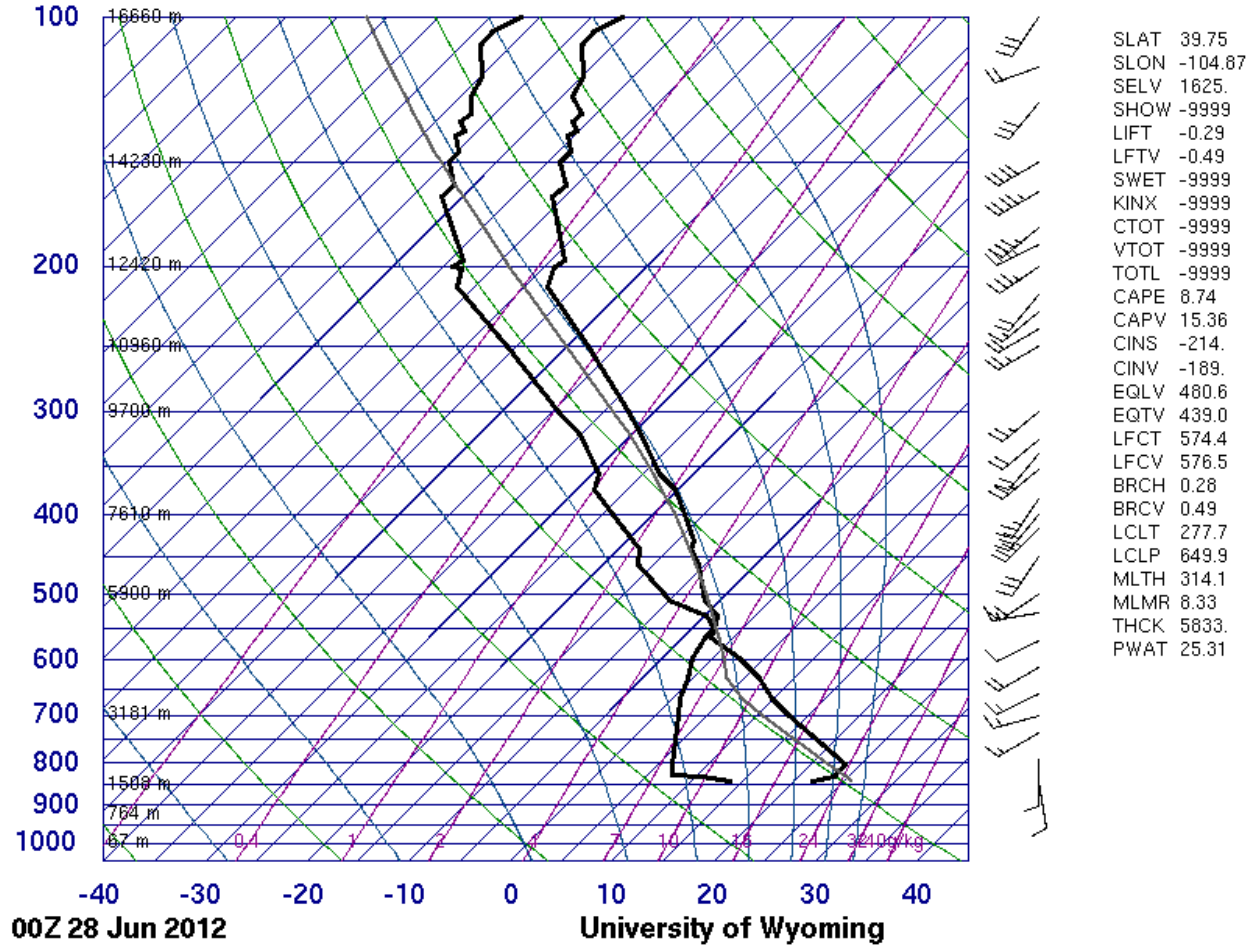


Figure A.2: Same as Fig. A.1 but shown is the 0000 UTC June 28, 2012 KDNR sounding SKEW-T for the June 27, 2012 storm event. Boundary layer height was estimated to be ~560 hPa (~4.8 km).

**72469 DNR Denver**

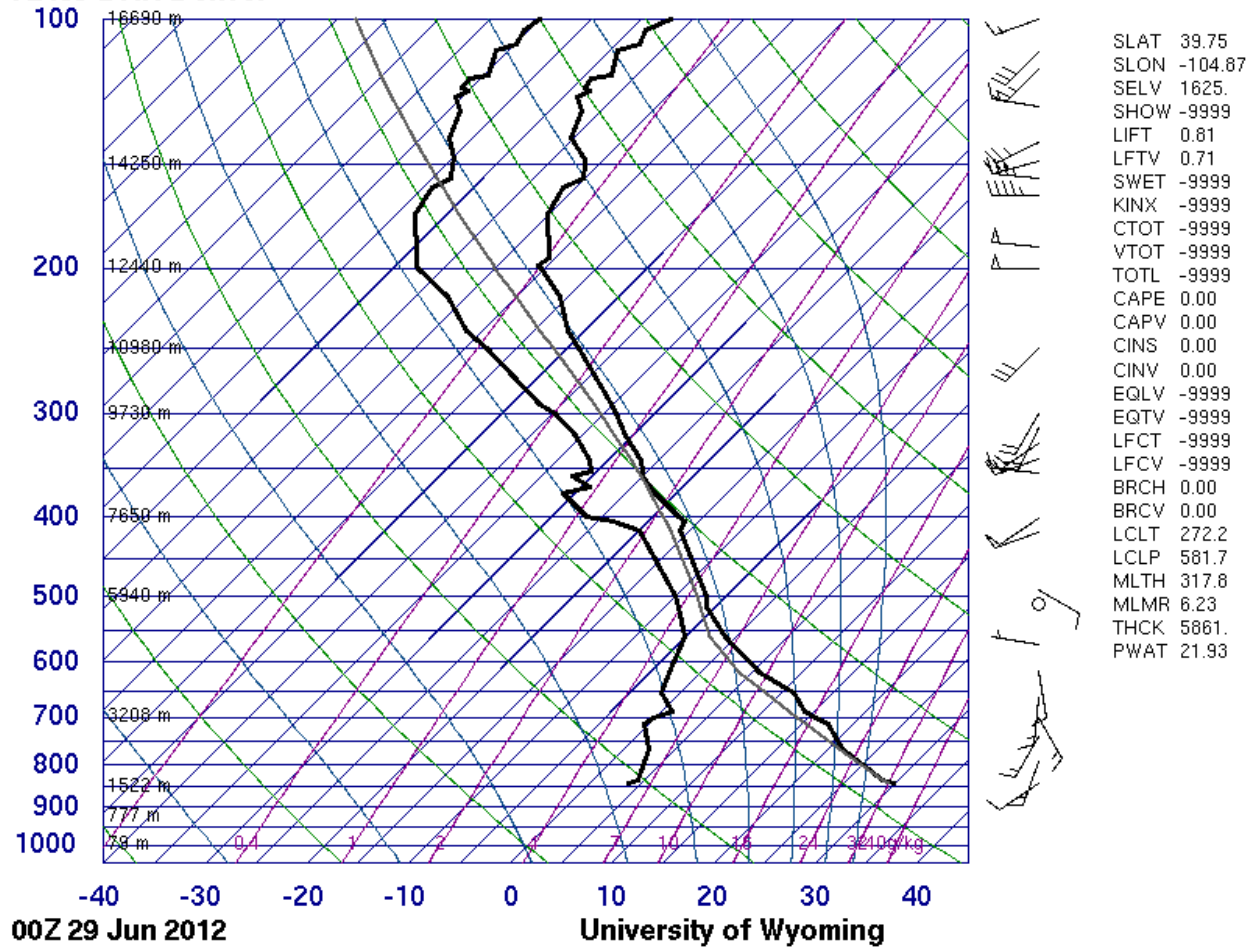
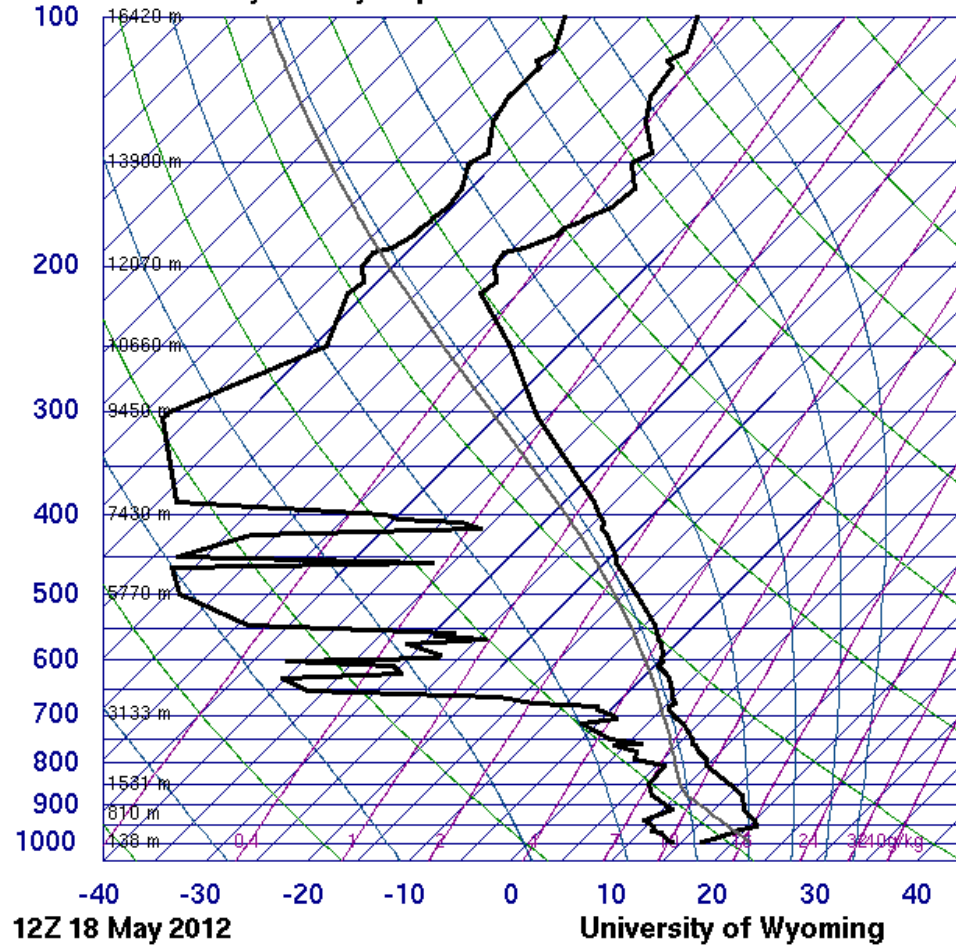


Figure A.3: Same as Fig. A.1 but shown is the 0000 UTC June 29, 2012 KDNR sounding SKEW-T for the June 28, 2012 storm event. Boundary layer height was estimated to be ~550 hPa (~4.8 km).

**72230 BMX Shelby County Airport**



SLAT	33.16
SLON	-86.76
SELV	178.0
SHOW	1.58
LIFT	2.14
LFTV	1.80
SWET	89.38
KINX	28.10
CTOT	19.90
VTOT	27.90
TOTL	47.80
CAPE	0.00
CAPV	0.00
CINS	0.00
CINV	0.00
EQLV	-9999
EQTV	-9999
LFCT	-9999
LFCV	-9999
BRCH	0.00
BRCV	0.00
LCLT	283.0
LCLP	863.8
MLTH	295.1
MLMR	8.96
THCK	5632.
PWAT	22.71

Figure A.4: Same as Fig. A.1 but shown is the 0000 UTC May 18, 2012 KBMX sounding SKEW-T for the May 18, 2012 storm event. The 0000 UTC May 19, 2012 KBMX sounding appeared incomplete for pressure levels above 608 hPa, though the boundary layer height was estimated to be ~700 hPa (~3.0 km) from the data available. Boundary layer height was estimated to be ~780 hPa (~2 km) from this sounding, therefore a boundary layer height of 2.5 km was used for analysis.

**72230 BMX Shelby County Airport**

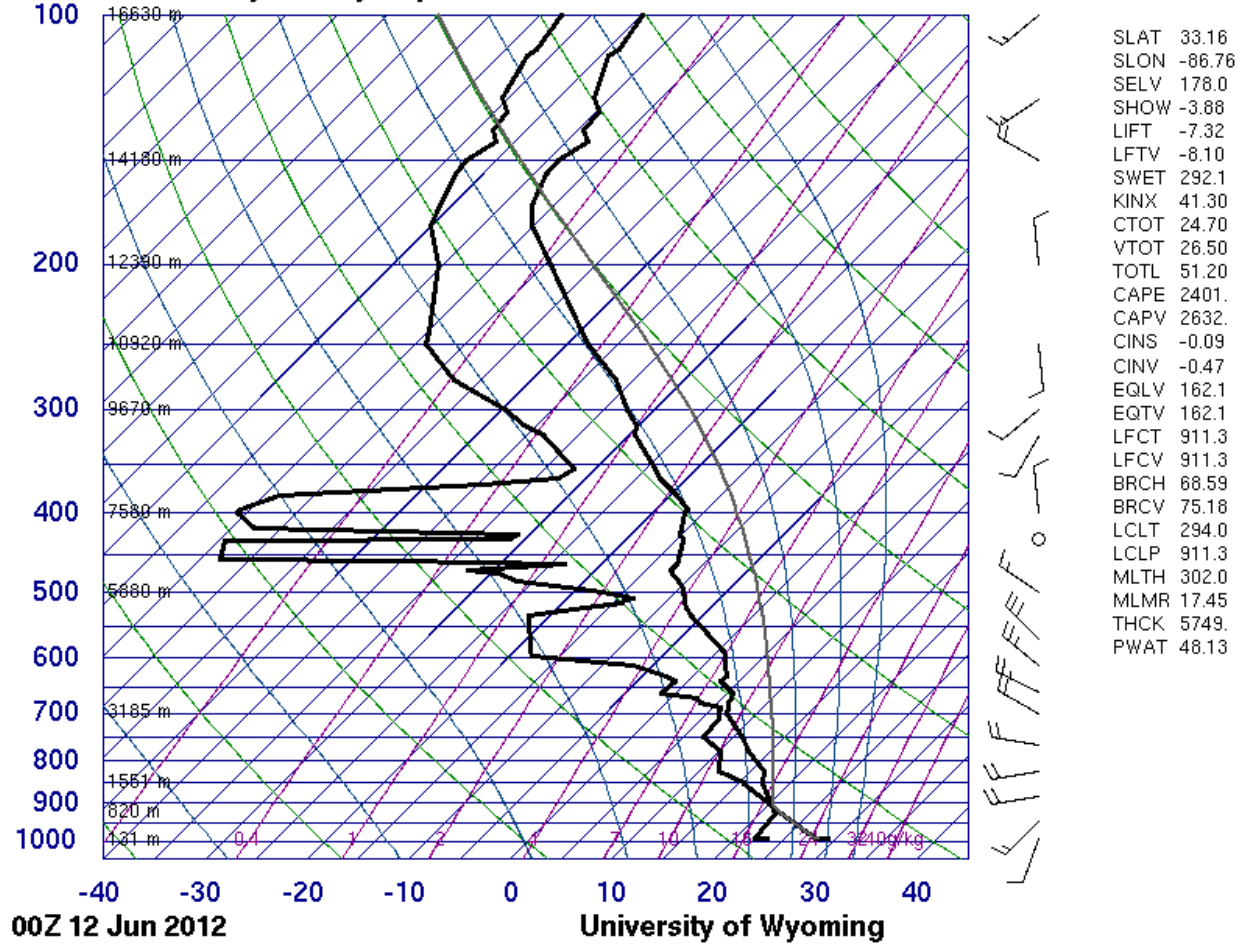


Figure A.5: Same as Fig. A.1 but shown is the 0000 UTC June 12, 2012 KBMX sounding SKEW-T for the June 11, 2012 storm event. Boundary layer height was estimated to be ~925 hPa (~0.8 km).